

Hochschule für angewandte Wissenschaften
München

Invariant based optimization of a CFRP wing box

A thesis
submitted in partial fulfillment of the requirements
for the degree of:

Master of Science (M.Sc.)

Timo Stiels
Matr. Nr.: 10314419
February 15, 2022

Supervisor

Prof. Dr.Ing. Klemens Rother
Munich University of Applied Science

Co-Supervisor

Prof. Aniello Riccio
University of Campania

Supervisors from industry and research institutions

Francesco Di Caprio, Ph.D.
CIRA (Italian Aerospace Research Center)

Josef Neuhäusler, M.Sc.
Munich University of Applied Science

Statutory Declaration

I declare that I have authored this thesis independently, that I have not used other than the declared sources / resources, and that I have explicitly marked all material which has been quoted either literally or by content from the used sources.

(date, signature)

Abstract

This thesis covers the optimization of skins of a vertical stabilizer of an aircraft fighter made from CFRP. A new invariant method is applied to optimize the laminate design considering so-called double double laminates $[\pm\Phi, \pm\Psi]$. This method is implemented in the DD-Design Tool (DiCaprio, Riccio, and Tsai 2020) which has been improved and implemented in Python within the scope of this thesis. The new tool has been proven as computationally efficient for optimizing laminated structures and the obtained results show great weight savings for skins made of double double laminates, compared to legacy quad laminates or aluminum constructions. Due to the partial low loading resulting in thin laminates with a thickness of one building block, two design strategies were defined and investigated for their effects on weight: 1st Symmetry Design Approach, 2nd Homogenization Design Approach, both applied to the digitized optimization results. It is shown that the Symmetry Design Approach yields a significantly lower weight than homogenization for the studied model and all considered failure criteria. In addition, the achieved skin weights for first ply failure are compared with skin weights corresponding to last ply failure, where weight reductions of 28% and 35% are obtained for Tsai-Wu and unit circle, respectively.

Contents

List of Figures	VI
List of Tables	VIII
Nomenclature	X
1 Introduction	1
1.1 Thesis objective	1
1.2 Thesis outline	2
2 Fundamental Background	3
2.1 Fiber and matrix materials	4
2.2 Core materials	9
2.3 Material symmetries and constants	10
2.4 Unidirectional Layer	12
2.5 Transformation of stress and strain	13
2.6 Transformation of stiffness	16
2.7 Classical Laminate Theory	18
2.8 Failure Criteria	21
3 FRP Design Methodologies	34
3.1 A novel invariant method	34
3.1.1 Tsai’s modulus and the master ply concept	34
3.1.2 Normalized stiffness of laminates and homogenization	36
3.1.3 Legacy quad and double-double laminates	38
3.1.4 Trace-based sizing method	39
3.2 Optimization frameworks	41
3.2.1 Lamsearch	41
3.2.2 DD-Design Tool	42
3.2.3 Improved DD-Design Tool	43
4 Invariant Based Optimization Of A CFRP Wing Box	46
4.1 Model description	46
4.2 Influence of partitioning on the double double laminate of the wing skin	48
4.3 Skin optimization with Double-Double laminates	50
4.3.1 Determination of the best design using Tsai-Wu	51
4.3.2 Determination of the best design using unit circle	53
4.3.3 Determination of the best design using Nettles circle	56
4.3.4 Summary DD optimization using the improved DD-Design Tool	58
4.3.5 Further optimization potential of best DD designs determined by RSM and GA	60
4.4 Comparison of Double Double with Legacy Quad and Aluminum designs	62
5 Summary and Conclusion	64
References	66

A	Optimization code	68
A.1	User manual	68
A.1.1	Setup for a simple model with 1 load case	68
A.1.2	Setup for a symmetric model with 2 load cases	70
A.1.3	Setup for a quad laminate model	72
A.1.4	Format of the output file	74
A.2	Python implementation	76
A.3	Python code verification	77
A.3.1	Load case 1, Tsai-Wu failure criterion	78
A.3.2	Load case 1, unit circle failure criterion	79
A.3.3	Load case 1, Nettles circle failure criterion	80
A.3.4	Load case 2, Tsai-Wu failure criterion	81
A.3.5	Load case 2, unit circle failure criterion	82
A.3.6	Load case 2, Nettles circle failure criterion	83

List of Figures

2.1 Unidirectional ply with fiber packing and stacking to multidirectional laminates, adapted from (Schürmann 2007, p. 15). 4

2.2 Change in the chemical structure of PAN under the influence of heat (Jäger and Hauke 2010). 5

2.3 Different core types in sandwich constructions, adapted from (Ueng 2002, p. 409). 9

2.4 Different Honeycomb core geometries, adapted from (Zenkert 1997, p. 25). 9

2.5 Coordinate system aligned with the fiber direction for unidirectional layers, adapted from (Kollar and Springer 2003, p. 19). 12

2.6 Sign convention for ply rotation angle and positive shear, adapted from (Schürmann 2007, p. 208) and (Tsai, José Daniel D. Melo, et al. 2017, p. 1). 13

2.7 Mohr’s circle representation of stress and its principal components, adapted from (Tsai 2008, p. 28). 15

2.8 In-plane, bending, and twisting loads applied to a laminate (Mallick 2008, p. 185). 18

2.9 Components of ABD and their effects on the laminates response (Verein Deutscher Ingenieure 2006, p. 61). 20

2.10 Failure modes of unidirectional layer and their respective designation, adapted from (Schürmann 2007, pp. 347, 351, 364, 365, 366). 22

2.11 Tsai-Wu failure envelopes in strain space for on-axis and various off-axis ply orientations for T300-5208, adapted from (Tsai and José Daniel D. Melo 2015, p. 239). 25

2.12 FPF envelopes in stress and strain space for altered laminate layups, adapted from (Tsai 2008, p. 173). 27

2.13 Superimposed Tsai-Wu failure envelopes and resulting Omni envelope for T300-5208 and IM7 977-3. 28

2.14 Superimposed Tsai-Wu LPF failure envelopes and resulting LPF Omni envelope for T300-5208 and IM7 977-3. 30

2.15 Unit circle failure envelope and anchor points obtained by Omni LPF envelope. 31

2.16 Unit circle FPF envelopes by superimposed Omni FPF and LPF envelopes. 32

2.17 Nettles circle for two materials in strain space, including FPF and LPF Omni failure envelopes, and FPF unit circle envelopes. 33

3.1 Trace normalized stiffness components (%) and required number of repeats r for homogeneity for: a) $[0,45,0,-45,90,45,0,0,-45,0]_{rS}$, b) $[0,45,0,-45,90,45,0,0,-45,0]_r$ and c) $[18,-62,-18,62]_r$ 37

3.2 Increasing homogenization of a $[0/90]$ laminate with different ply thickness and repeats, adapted from (Tsai, José Daniel D. Melo, et al. 2017, p. 45). 38

3.3 Flowchart trace-based sizing method, adapted from (Tsai, Arteiro, and Jose D. D. Melo 2016, p. 591). 40

3.4 Double double laminate strength ratio field determined by the Lamsearch Excel tool. 41

3.5 Schematic determination of the strength ratio field R for n load cases. 42

3.6 Flowchart DD-Design Tool. 43

3.7 Optimization Flowchart of the improved DD-Design Tool. 45

4.1 Wing model geometry with highlighted load introduction points and finite element mesh. 47

4.2 Failure envelopes for ACA unidirectional layer. 48

4.3 Partitioned skins for different number of cells $n_c = n^2$ 49

4.4 Optimal double double angles dependent on the number of cells ($n_c = n^2$) and the respective failure criterion. 49

4.5	Resolution of the strength parameter field $R(\Phi, \Psi)$ based on different angle increments.	50
4.6	Double Double ply orientations for skin optimization.	50
4.7	Skin weights for different angle increments and design approaches, using the Tsai-Wu failure criterion for FPF.	51
4.8	Wing skin thickness profile for the Tsai-Wu FPF criterion.	51
4.9	Double double angles and averaged strength for all iterations for the best design derived by the Tsai-Wu failure criterion and an angle increment of 2.5° .	52
4.10	Differences in weight for FPF and LPF for Tsai-Wu failure criterion optimizations (no convergence was achieved for 1° LPF).	53
4.11	Wing skin thickness profile for the Tsai-Wu LPF criterion.	53
4.12	Skin weights for different angle increments and design approaches, using the unit circle failure criterion for FPF.	54
4.13	Wing skin thickness profile for the unit circle FPF criterion.	54
4.14	Double double angles and averaged strength for all iterations for the best design derived by the unit circle failure criterion and an angle increment of 4.5° .	55
4.15	Differences in weight for FPF and LPF for unit circle failure criterion optimizations.	56
4.16	Wing skin thickness profile for the unit circle LPF criterion.	56
4.17	Skin weights for different angle increments and design approaches, using the Nettles circle failure criterion.	57
4.18	Wing skin thickness profile for the Nettles circle criterion.	57
4.19	Double double angles and averaged strength for all iterations for the best design derived by the Nettles circle failure criterion and an angle increment of 6.0° .	58
A.1	Test case: rectangular plate with 49 partitions and two load cases.	77
A.2	Double Double angles and averaged strength of all iterations for LC 1 and Tsai-Wu failure criterion.	78
A.3	Double Double angles and averaged strength of all iterations for LC 1 and unit circle failure criterion.	79
A.4	Double Double angles and averaged strength of all iterations for LC 1 and Nettles circle failure criterion.	80
A.5	Double Double angles and averaged strength of all iterations for LC 2 and Tsai-Wu failure criterion.	81
A.6	Double Double angles and averaged strength of all iterations for LC 2 and unit circle failure criterion.	82
A.7	Double Double angles and averaged strength of all iterations for LC 2 and Nettles circle failure criterion.	83

List of Tables

2.1	Density, tensile modulus and tensile strength of selected fiber materials (Mallick 2008, pp. 33–34).	6
2.2	Selection of matrix materials for fiber reinforced plastics and their typical fields of application (Mallick 2008, p. 60).	7
2.3	Density, tensile modulus and tensile strength of selected matrix materials (Park 2018, pp. 199, 206).	7
2.4	Transformation variables for stress and strain in Mohr’s circle, adapted from (Tsai 2008, p. 27).	15
2.5	linear combinations of on-axis stiffness moduli, adapted from (Tsai and José Daniel D. Melo 2015, p. 62).	17
3.1	Material parameters and trace normalized plane stress stiffness components of various CFRP, adapted from (Tsai and José Daniel D. Melo 2015, p. 281).	35
3.2	Master ply material parameter.	35
3.3	Load-strain relationship in absolute and normalized form.	36
4.1	Material parameters of aluminum, HRP 4.8 honeycomb and unidirectional ACA layer, taken from (Rother 1985, p. 14).	47
4.2	Degraded material parameters for ACA plies.	48
4.3	Optimal double double angles Φ , Ψ derived by different angle increments using the Tsai-Wu failure criterion.	52
4.4	Optimal double double angles Φ , Ψ derived by different angle increments using the unit circle failure criterion.	55
4.5	Optimal double double angles Φ , Ψ derived by different angle increments using the Nettles circle failure criterion.	58
4.6	Skin weight for different failure criteria and failure modes.	58
4.7	Skin weight for different failure criteria and design approaches.	59
4.8	Optimal double double angles obtained by different failure criteria.	59
4.9	Comparison of optimized designs based on DD-Tool, RSM and GA optimization for homogenized laminate design.	60
4.10	Comparison of optimized designs based on DD-Tool, RSM and GA optimization for symmetric laminate design.	61
4.11	Comparison of skin weights of legacy quad and aluminum design with digitized double double laminates.	62
4.12	Comparison of skin weights of legacy quad and aluminum design with symmetric double double laminates.	63
4.13	Comparison of skin weights of legacy quad and aluminum design with homogenized double double laminates.	63
A.1	Two load cases for plate optimization.	77
A.2	Resulting cell thicknesses for LC 1 and Tsai-Wu failure criterion.	78
A.3	Resulting cell strengths for LC 1 and Tsai-Wu failure criterion.	78
A.4	Resulting digitized cell thicknesses for LC 1 and Tsai-Wu failure criterion.	78
A.5	Resulting cell thicknesses for LC 1 and unit circle failure criterion.	79
A.6	Resulting cell strengths for LC 1 and unit circle failure criterion.	79
A.7	Resulting digitized cell thicknesses for LC 1 and unit circle failure criterion.	79
A.8	Resulting cell thicknesses for LC 1 and Nettles circle failure criterion.	80
A.9	Resulting cell strengths for LC 1 and Nettles circle failure criterion.	80
A.10	Resulting digitized cell thicknesses for LC 1 and Nettles circle failure criterion.	80

A.11 Resulting cell thicknesses for LC 2 and Tsai-Wu failure criterion.	81
A.12 Resulting cell strengths for LC 2 and Tsai-Wu failure criterion.	81
A.13 Resulting digitized cell thicknesses for LC 2 and Tsai-Wu failure criterion.	81
A.14 Resulting cell thicknesses for LC 2 and unit circle failure criterion.	82
A.15 Resulting cell strengths for LC 2 and unit circle failure criterion.	82
A.16 Resulting digitized cell thicknesses for LC 2 and unit circle failure criterion.	82
A.17 Resulting cell thicknesses for LC 2 and Nettles circle failure criterion.	83
A.18 Resulting cell strengths for LC 2 and Nettles circle failure criterion.	83
A.19 Resulting digitized cell thicknesses for LC 2 and Nettles circle failure criterion.	83

Nomenclature

Abbreviations

CFRP	Carbon fiber reinforced plastic
CLT	Classical laminate theory
DD	Double double
FE	Finite element
FPF	First ply failure
FRP	Fiber reinforced plastic
GA	Genetic algorithm
LPF	Last ply failure
NC	Nettles circle
PAN	Polyacrylonitrile
RSM	Response surface method
TW	Tsai-Wu
UC	Unit circle
UD-layer	Unidirectional layer

Latin characters

\mathbf{a}	Extensional compliance matrix
\mathbf{a}^n, a_{ij}^n	Thickness normalized extensional compliance matrix
\mathbf{A}	Extensional stiffness matrix
\mathbf{A}^*	Trace normalized extensional stiffness matrix
\mathbf{A}^n	Thickness normalized extensional stiffness matrix
\mathbf{B}	Bending-extensional coupling stiffness matrix
\mathbf{B}^*	Trace normalized coupling stiffness matrix
\mathbf{B}^n	Thickness normalized coupling stiffness matrix
C_{ij}, C_{pqrs}	Stiffness tensor components
\mathbf{D}	Bending stiffness matrix
\mathbf{D}^*	Trace normalized bending stiffness matrix

\mathbf{D}^n	Thickness normalized bending stiffness matrix
E, E_i	Elastic/shear modulus
\tilde{E}_i	Degenerated elastic modulus
E_i^*	Trace normalized engineering constants
E_m^*	Matrix degeneration factor
F_i, F_{ij}	Strength parameter in stress space
F_{12}^*	Normalized interaction term
G	Shear modulus
G_i, G_{ij}	Strength parameter in strain space
h	Laminate thickness
H_i, H_{ij}	Laminate strength parameter in stress space
k	Failure index
m	$\cos(\alpha)$
m	Mass
\mathbf{M}	Laminate moments
n	$\sin(\alpha)$
n_c	Number of cells
\mathbf{N}	Laminate forces
\mathbf{Q}, Q_{ij}	Plane stress stiffness
\mathbf{Q}^*, Q_{ij}^*	trace normalized plane stress stiffness
R, R_i	Strength ratio
R_{avg}	Averaged strength ratio
S_{ij}, S_{pqrs}	Compliance tensor components
S	Shear strength
t_i	Cell thickness
\mathbf{T}_σ	Stress transformation matrix on-axis to off-axis
\mathbf{T}_ε	Strain transformation matrix on-axis to off-axis
U_i	Material dependent stiffness components
v_i	Volume fraction

x, y, z	Global Coordinates
x_1, x_2, x_3	On-axis Coordinates
X	Tensile Strength in fiber direction
X'	Compressive Strength in fiber direction
Y	Tensile Strength in transversal direction
Y'	Compressive Strength in transversal direction

Greek characters

α	Ply angle
ε_i	Strain tensor component
ε	Strain tensor
ε_{uc}	Failure strain unit circle
ε_{nc}	Failure strain Nettles circle
η_i	Stress partitioning parameter
κ_i	Curvature of the laminates reference plane
ν, ν_{ij}	Poisson's ratio
ρ	Density
σ_i	Stress tensor component
σ	Stress tensor
Φ	Double double angle
Ψ	Double double angle

1 Introduction

Fiber Reinforced Plastics (FRP) are composite materials that consist of fibers and a matrix, where the fibers are carrying the loads and the matrix binds the fibers together. Moreover, the matrix acts as a load-transfer medium between the fibers and protects the fibers from being exposed to the environment (Reddy 2004, p. 1).

FRP materials are used in various industries such as aerospace, automotive, rail industry, marine industry and many more. All industries rely on the lightweight construction properties of the the materials, the freedom of shaping, the possibility of integral construction and the corrosion resistance. In addition to the above-mentioned reasons, the significantly superior fatigue strength compared to aluminum plays a major role in the aerospace industry. Here, FRP materials are used for cladding, secondary structures as well as primary structures (Schürmann 2007, pp. 5–11).

For example, the Airbus A350 XWB structure is made of more than 50% of composite materials. Its wing mostly made of **Carbon Fiber Reinforced Plastics (CFRP)**, including the upper and lower cover. The initially higher production cost are compensated by saving money on future maintenance costs since the material doesn't rust or corrode. The A350 XWB requires 50% fewer structure maintenance tasks and the threshold for airframe checks is at 12 years compared to eight for the A380 (Airbus 2021b). In addition, the use of CFRP results in a 25% reduction in fuel consumption compared to its aluminum competitors (Airbus 2021a).

But the design process of structures made of CFRP materials is difficult. In the early 1960s, when CFRP began to be used in the aerospace industry, companies decided to make laminates from four ply angles: 0° , $\pm 45^\circ$ and 90° , referred to as legacy quad. With legacy quads, a number of rules for laminate design were developed, such as the presence of midplane symmetry, the 10% rule, the need for balanced layup, etc. and these rules have remained until today.

Recently, a group of researchers led by Stephen W. Tsai discovered a novel method for laminate design using an invariant based description of stiffness and strength. They forgo legacy quads and instead use balanced laminates with two arbitrary ply angles that allow efficient optimization and manufacturing. These laminates are called double double laminates.

1.1 Thesis objective

The objective of this work is to use the invariant methods for the design optimization of skins of an aircraft rudder wing box made of CFRP. Three failure criteria, Tsai-Wu, Unit-Circle and Nettles-Circle will be used to optimize the laminate angles and skin thickness profile with respect to minimum weight for double double layups using the DD-Design Tool (DiCaprio, Riccio, and Tsai 2020). Differences in weight will be investigated for first ply failure (FPF) and last ply failure (LPF). Weight savings will be benchmarked to an aluminum and a legacy quad design. In addition, laminate homogenization and the corresponding minimum repeat factors will be explored, as well as the effect on weight if a symmetrical layup is used instead. Finally, a further optimization potential for the optimum DD-design is determined by a genetic optimization and response surface optimization.

1.2 Thesis outline

Chapter 2 covers the fundamentals of this thesis. First, a short introduction to carbon fiber reinforced materials is given, followed by a brief description of honeycomb core materials. The mechanical principles of multidirectional composite laminates are explained, and failure theories for CFRPs are introduced.

In chapter 3, the invariant approach to laminate design is described and a direct sizing method developed by Tsai is presented. In addition, the original DD-Design Tool is explained and an improved design tool for double double laminates is presented. Both tools apply the invariant method by Tsai, and a finite element software is used to solve the boundary problem.

Chapter 4 deals with the optimization of a vertical stabilizer of an aircraft. The improved design tool is applied for optimization and results for double double laminates are compared to those for legacy quad laminates and aluminum.

2 Fundamental Background

This chapter describes the basic principles of fiber reinforced plastics. First, a brief introduction into fiber and resin materials is given, followed by the mechanical relations of FRP materials. Since this work considers multidirectional laminates made from unidirectional layers, other types are only briefly discussed if at all.

It is necessary to first explain some conventions and notation simplifications that will be used in the following chapters:

- The local (fiber-orientated) coordinate system is denoted by x_1, x_2, x_3 and the global one by x, y, z
- Displacements in local coordinate system are denoted as u_1, u_2, u_3 and in the global system as u, v, w

Furthermore, contracted notation is used for stress, strain, stiffness and compliance tensors. In contracted notation, the number of indices is reduced by half, and the relations can be expressed in terms of matrix equations. This is possible because these tensors are symmetric:

$$\begin{bmatrix} \sigma_1 \\ \sigma_2 \\ \sigma_3 \\ \sigma_4 \\ \sigma_5 \\ \sigma_6 \end{bmatrix} = \begin{bmatrix} \sigma_{11} \\ \sigma_{22} \\ \sigma_{33} \\ \sigma_{23} \\ \sigma_{13} \\ \sigma_{12} \end{bmatrix} ; \quad \begin{bmatrix} \sigma_{11} & \sigma_{12} & \sigma_{13} \\ \sigma_{21} & \sigma_{22} & \sigma_{23} \\ \sigma_{31} & \sigma_{32} & \sigma_{33} \end{bmatrix}$$

$$\begin{bmatrix} \varepsilon_1 \\ \varepsilon_2 \\ \varepsilon_3 \\ \varepsilon_4 \\ \varepsilon_5 \\ \varepsilon_6 \end{bmatrix} = \begin{bmatrix} \varepsilon_{11} \\ \varepsilon_{22} \\ \varepsilon_{33} \\ 2\varepsilon_{23} \\ 2\varepsilon_{13} \\ 2\varepsilon_{12} \end{bmatrix} ; \quad \begin{bmatrix} \varepsilon_{11} & \varepsilon_{12} & \varepsilon_{13} \\ \varepsilon_{21} & \varepsilon_{22} & \varepsilon_{23} \\ \varepsilon_{31} & \varepsilon_{32} & \varepsilon_{33} \end{bmatrix}$$

Engineering strain is used throughout this thesis, so the shear components of the tensorial strain are multiplied by the factor two, as shown above. In addition, the contracted notation for stiffness C_{pqrs} and compliance S_{pqrs} yields second rank matrices instead of fourth rank matrices:

$$\begin{matrix} C_{ij} \\ S_{ij} \end{matrix} \quad i, j = 1, 2, \dots, 6$$

They are not shown here, but the derivation of compliance and stiffness in contracted notation can be found in (Tsai 2008, pp. 10–13).

2.1 Fiber and matrix materials

CFRP materials are widely used in all industries wherever lightweight structures are needed and high demands on stiffness and strength have to be met. CFRP offer both, low weight and high strength and stiffness. They consist of two components: fibers and resin, where fibers are placed in the resin matrix as shown in figure 2.1.

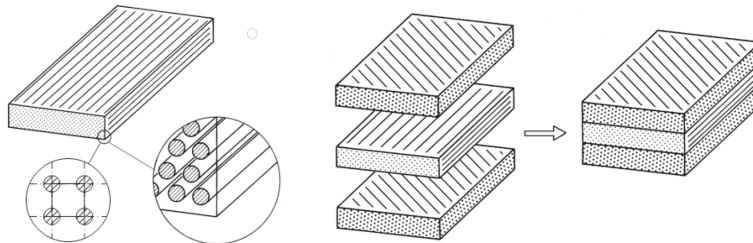


Figure 2.1: Unidirectional ply with fiber packing and stacking to multidirectional laminates, adapted from (Schürmann 2007, p. 15).

Fibers

Fibers are the load-bearing parts of fiber composites and must therefore have high strength and stiffness. Materials such as boron, carbon or silicon, for example, exhibit covalent bonding, which theoretically allows very high strength to be achieved. In practice, the strength and stiffness of materials depends on the occurrence and size of defects in the material structure, especially in brittle materials such as those mentioned above. According to the so-called size effect, defects statistically occur less at lower volumes than at higher volumes and therefore thin fibers are stronger than bulk material. The use of thin fibers divides the stressed volume of the material into many small volumes. An additional advantage is that the small fiber cross sections also reduce the size of the defects, thus reduce their effectiveness (Schürmann 2007, pp. 21–22).

Nowadays, the most commonly used fiber materials are carbon, glass, boron and aramid.

Glass fibers

Glass fibers are the most commonly used fibers for FRPs. They offer high tensile strength, high chemical resistance, excellent insulating properties and are low cost. The high density, low tensile modulus and the relatively low fatigue resistance are the disadvantages. Most commonly used glass fibers are E-type and S-type. While fibers of E-type have the lowest cost of all FRP fibers available, S-type offer the highest tensile strength among all fibers in use (Mallick 2008, p. 41).

Boron fibers

Boron fibers have an extremely high tensile modulus and offer, due to their relatively large diameter, excellent resistance to buckling. The disadvantage of boron fibers is their high cost. They cost more than most available carbon fibers and are therefore only used for few applications in the aerospace sector (Mallick 2008, pp. 56–57).

Aramid fibers

Aramid fibers have the lowest density and the highest strength-to-weight ratio among all commonly used FRP fibers. They are used in many applications where lightweight, high tensile strength, or resistance to impact damage is needed. The disadvantages are their low compressive strength and difficulties during machining due to their outstanding toughness. A well-known aramid fiber available on the market is Kevlar 49, which is often used in soft lightweight body armors (Mallick 2008,

pp. 53–54).

Carbon fibers

The most important properties of carbon fibers are their high axial strength and modulus, low density, good fatigue durability, negative thermal-expansion coefficient and excellent corrosion resistance. The disadvantages are a low strain to failure, low impact resistance, electrical conductivity and their cost (Wang and Gao 2021, p. 19).

Carbon fibers are produced by carbonization and graphitization of organic fibers. Mostly PAN (polyacrylonitrile) precursors are used, but also pitch-based exist. After producing and stabilizing the precursor, the carbon fibers are created by carbonization. During the carbonization, all foreign atoms are removed from the material and a turbostratic structure of C-atoms is obtained. With increasing treatment temperature, also the graphitic ribbon structure increases. The alignment of the ribbons in longitudinal direction of the fibers is the prerequisite for high fiber strength and a high modulus of elasticity. Figure (2.2) shows the change in the chemical structure of the fiber material during carbonization. Depending on the treatment temperature, the performance of carbon fibers alter. They can be divided in high-strength fibers (HT/HS type, 1200°C to 1500°C), intermediate modulus fibers (IM type, 1500°C to 1800°C) and high modulus fibers (HM, UHM types, up to 3000°C) (Lengsfeld, Mainka, and Altstädt 2020, pp. 17–31).

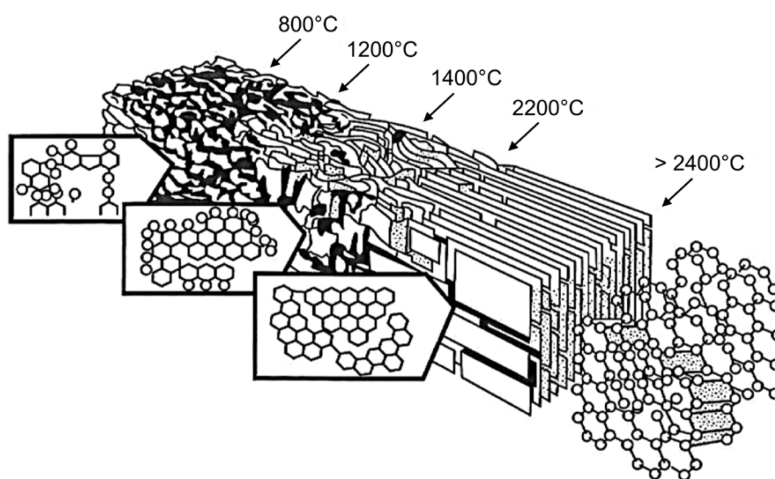


Figure 2.2: Change in the chemical structure of PAN under the influence of heat (Jäger and Hauke 2010).

Carbon fibers with high tensile strength have the lowest modulus among carbon fibers, while carbon fibers with high- and ultrahigh-modulus have the lowest tensile strength and tensile strain-to-failure. High tensile strength carbon fibers are, for example, T-300 and AS-4. T-40 and IM-7 are fibers with an intermediate modulus and GY-70 fibers are an example of ultrahigh modulus (Mallick 2008, pp. 49–50).

Resin matrix

The matrix covers several tasks within the fiber reinforced composite. The matrix keeps the fibers in place, transfers stress between the fibers and protects the fibers from adverse environment. The selection of a suitable matrix is important, because it strongly influences the compressive,

Table 2.1: Density, tensile modulus and tensile strength of selected fiber materials (Mallick 2008, pp. 33–34).

Fiber-Type	Fiber	ρ [g/cm ³]	E_1 [GPa]	X[GPa]
Glass	E-glass	2.54	72.4	3.45
	S-glass	2.49	86.9	4.3
Boron		2.7	393	3.1
Aramid	Kevlar 49	1.45	131	3.62
PAN carbon	T-300	1.76	231	3.65
	AS-4	1.8	248	4.07
	T-40	1.81	290	5.65
	IM-7	1.78	301	5.31
	GY-70	1.96	483	1.52

interlaminar shear and in-plane shear properties. Furthermore, the matrix supports the fibers under compressive stress in the longitudinal direction of the fibers against buckling.

A various number of matrix materials are available for fiber reinforced plastics. They can be divided into thermoplastic and thermosetting resins, with each offering different advantages and disadvantages.

In a thermoplastic resin, for example, the molecules are not chemically bonded to each other, but are held together by weak secondary bonds or intermolecular forces such as van der Waals bonds and hydrogen bonds. Applying heat to the matrix can loosen these bonds, and by the application of pressure, a reforming of the material is possible. Furthermore, thermosetting resins have a relatively large strain-to-failure which provides a good resistance to matrix microcracking in the laminate.

In contrast to thermoplastic resin, the curing process of thermosetting polymers joins molecules chemically by creating cross-links. These cross-links form a rigid, three-dimensional network structure which can't be resolved, once they are created. Thermosetting resin usually come with a low molecular weight. Their low viscosity contributes to a good wet-out between the fibers and the matrix, which is necessary to achieve fiber-matrix interaction within the composite. Thermosetting resin are thermally stable, have a chemical resistance and also exhibit less creep and stress relaxation compared to thermoplastic polymers (Mallick 2008, p. 59–67).

Table (2.2) shows selected matrix materials and their typical fields of application. Due to the variety of available matrix materials, only a limited selection can be presented here. Further information can be found in the relevant literature.

Fiber-matrix materials in aircraft design

The first FRP used in aircraft design were a material combination of boron fibers and epoxy matrices, where nowadays mostly carbon fibers are used. Both fiber material have a high modulus and also high strength, but due to the high density of boron, carbon fibers are preferred nowadays. Also their high corrosion and fatigue resistance is an important point (Park 2018, pp. 259–263).

CFRP material products

For highly stressed laminates, continuous fibers are mainly used. Only a few manufacturing processes are capable to lay yarns or rovings directly as unidirectional layers with the desired fiber

Table 2.2: Selection of matrix materials for fiber reinforced plastics and their typical fields of application (Mallick 2008, p. 60).

Resin-Type	Material	fields of application
Thermoplastic	Nylons	injection-molded articles
	thermoplastic polyesters	injection-molded articles
	polyether ether ketone	moderately high temperature applications
Thermosetting	Epoxies	aerospace and aircraft applications
	Polyimides	high temp. aerospace applications
	polyesters	automotive, marine, chemical
	vinyl esters	automotive, marine, chemical

Table 2.3: Density, tensile modulus and tensile strength of selected matrix materials (Park 2018, pp. 199, 206).

Resin-Type	ρ [g/cm ³]	E_m [GPa]	X[MPa]
Epoxy	1.2–1.4	2.5–5.0	50–110
Polyesters	1.1–1.4	1.6–4.1	35–90
Vinyl esters	1.04–1.1	3.2–3.6	68–80
Nylon	1.1	1.3–3.5	55–90
thermopl. Polyester	1.3–1.4	2.1–2.8	55–60
polyether ether ketone	1.3–1.35	3.5–4.4	100

orientations, for example pultrusion or placement using laying robots. To reduce effort in correct fiber positioning, semi-finished products such as prepregs are used (Schürmann 2007, pp. 57–58). Prepregs or pre-impregnated materials are thin sheets of fibers embedded in semi-cured resin material, where the fibers may be in woven form or aligned in parallel. For example, unidirectional (CFRP) prepreg tapes are used to manufacture wing skins of airplanes such as the Airbus A350, A380 or A400M by automated tape laying (MTorres 2021).

Mechanical description

The behavior of composite materials is quite difficult to describe in terms of mechanical equations. Not only the stressed fibers and matrix have to be included, but also the interaction between the two constitutes. The interaction between individual fibers and their surrounding matrix is described micromechanically, while in the macromechanical approach the fiber-reinforced plastics are assumed to be a homogeneous material in which the fibers and the matrix of a single layer are treated as one component. Micromechanics is rather used in the context of material science and macromechanics is used by FRP designers (Schürmann 2007, pp. 16–17) .

Assuming uniformly distributed fibers, perfect bonding between fibers and matrix, linear material behavior, void free matrix, a stress-free initial state, and forces applied either parallel or normal to fiber direction, the material parameters of the composite material can be determined easily by the

so-called rule of mixtures.

The composite modulus in longitudinal direction E_L is intermediate between the fiber and the matrix modulus and depends on the volume fraction of fibers in the composite (Mallick 2008, pp. 120–125).

$$E_L = E_f v_f + E_m v_m \quad (2.1)$$

The transverse modulus E_T of the composite can be derived by replacing the fibers and the matrix by their respective equivalent volume depicted as two structural components with strong bonding. Assuming the total deformation is the sum of fibers and matrix deformation and stresses are equal in fibers and matrix, the transverse modulus of the composite depends on the volume fractions and modulus of fiber and matrix (Mallick 2008, pp. 138–144).

$$\frac{1}{E_T} = \frac{v_f}{E_f} + \frac{v_m}{E_m} \quad (2.2)$$

In addition to the elastic moduli, other parameters such as the composite density, the coefficient of thermal expansion or the strength can be determined using the rule of mixtures.

2.2 Core materials

Composite sandwich constructions are commonly used to obtain structures that are lightweight but also strong and stiff. They are widely found in aerospace applications, but also in other disciplines. In principle, sandwich structures are analogous to I-beams, where the web carries the shear forces and the flanges provide the bending rigidity. The core of sandwich constructions has the same functions as the web of an I-beam, and the face sheets or skins provide flexural rigidity.

To ensure this, there must be a strong adhesive bond between the core and the faces. In addition, the shear modulus of the core must be high enough to prevent the faces from sliding relative to each other, the Young's modulus perpendicular to the faces must be high enough to maintain the spacing of the faces, and the core must not fail under the applied transverse load (Ueng 2002, p. 408). To ensure low weight, the core should have a low density.

The different types of cores can be grouped into foams, honeycombs and corrugated cores, as shown in figure 2.3 (Zenkert 1997, p. 23). Since honeycomb cores are used in the context of this thesis, only these will be explained below.

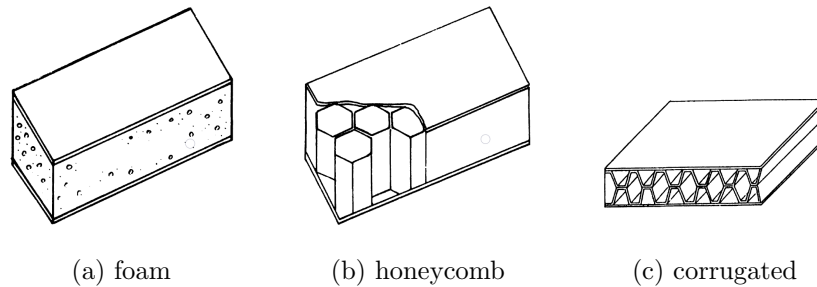


Figure 2.3: Different core types in sandwich constructions, adapted from (Ueng 2002, p. 409).

Honeycomb cores are available in various cell shapes and materials, each with different characteristics. For example, they can be square, rectangular, triangular, corrugated or in hexagonal shape, where the latter is most commonly used. Typical materials are aluminum, impregnated glass or aramid fiber mats, but impregnated paper is also sometimes used (Zenkert 1997, p. 25). In figure 2.4 different shapes of honeycomb cores are shown: a) the traditional hexagon shape, b) square shape, c) an over-expanded hexagonal shape, and d) a flex-core shape.

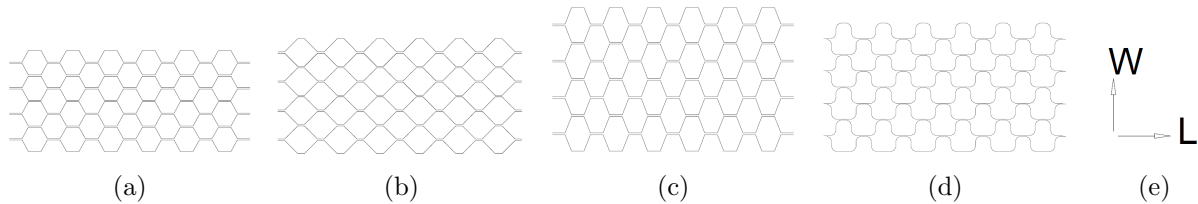


Figure 2.4: Different Honeycomb core geometries, adapted from (Zenkert 1997, p. 25).

However, for simulation, honeycombs are commonly modeled as continuous orthotropic material with respect to the principal directions W (width), L (length), T (transverse), as shown in figure 2.4 e). Typical mechanical properties for different honeycomb cell shapes, materials and densities can be found in (Zenkert 1997, pp. 26–30).

2.3 Material symmetries and constants

The amount of independent parameters to describe a material behavior is dependent on the amount of material symmetries. For linear elastic materials without symmetry planes, the stiffness matrix \mathbf{C} , respectively the compliance matrix \mathbf{S} , of the generalized Hooke's law

$$\begin{aligned}\boldsymbol{\sigma} &= \mathbf{C}\boldsymbol{\varepsilon} \\ \boldsymbol{\varepsilon} &= \mathbf{S}\boldsymbol{\sigma}\end{aligned}\tag{2.3}$$

consist of 21 independent components to describe the stress-strain relationship. The stiffness matrix \mathbf{C} is derived by inverting the compliance matrix \mathbf{S} whose components S_{ij} can be determined by testing. The index notation of the Poisson's ratios and shear coupling coefficients in this work follows the notation in Tsai, Melo et al. (2017), Tsai and Melo (2015) and Tsai (1992). The coupling coefficients of the compliance matrix are normalized column-wise, resulting in an indexing that conforms to the conventions of matrix algebra:

$$\nu_{21} > \nu_{12} \text{ if } E_1 > E_2\tag{2.4}$$

where ν_{21} is the major Poisson's ratio and ν_{12} the minor Poisson's ratio.

$$\begin{aligned}\nu_{21} &= -\frac{S_{21}}{S_{11}} \\ \nu_{12} &= -\frac{S_{12}}{S_{22}} = \nu_{21} \frac{E_2}{E_1}\end{aligned}$$

Note that this convention is often ignored in most common practice (row normalized coupling coefficients): i.e. $\nu_{12} > \nu_{21}$ if $E_1 > E_2$ (Tsai, José Daniel D. Melo, et al. 2017, p. 15).

The shear moduli are designated by the letter E instead of G in accordance with the previously mentioned works. The elastic ($i = 1, 2, 3$) and shear moduli ($i = 4, 5, 6$) of the material are determined by uniaxial tensile/compression and shear tests, respectively.

$$E_i = \frac{\sigma_i}{\varepsilon_i} = \frac{1}{S_{ii}} \quad i = 1, \dots, 6.\tag{2.5}$$

Materials without symmetry planes are called **anisotropic materials** or triclinic materials and are the most general linear elastic materials. The stiffness and compliance matrix consist of 36 components and is symmetric from energy consideration (Tsai 2008, p. 13).

$$S_{ij} = S_{ji} \quad C_{ij} = C_{ji}\tag{2.6}$$

Thus, only 21 of the 36 components are independent.

$$\begin{bmatrix} \varepsilon_1 \\ \varepsilon_2 \\ \varepsilon_3 \\ \varepsilon_4 \\ \varepsilon_5 \\ \varepsilon_6 \end{bmatrix} = \begin{bmatrix} S_{11} & S_{12} & S_{13} & S_{14} & S_{15} & S_{16} \\ S_{21} & S_{22} & S_{23} & S_{24} & S_{25} & S_{26} \\ S_{31} & S_{32} & S_{33} & S_{34} & S_{35} & S_{36} \\ S_{41} & S_{42} & S_{43} & S_{44} & S_{45} & S_{46} \\ S_{51} & S_{52} & S_{53} & S_{54} & S_{55} & S_{56} \\ S_{61} & S_{62} & S_{63} & S_{64} & S_{65} & S_{66} \end{bmatrix} \begin{bmatrix} \sigma_1 \\ \sigma_2 \\ \sigma_3 \\ \sigma_4 \\ \sigma_5 \\ \sigma_6 \end{bmatrix}\tag{2.7}$$

In anisotropic materials, there is a shear-extension coupling, i.e. an applied normal or shear stress produces both extensional and shear deformations.

If one symmetry plane exists, a material is called **monoclinic material**. The coordinate system is chosen so that the axes x_1 and x_2 are in the plane of symmetry and x_3 perpendicular to it. For monoclinic materials, the number of independent components of the stiffness or compliance matrix, is reduced to 13. Furthermore, shear and extension are partially decoupled.

$$\mathbf{S} = \begin{bmatrix} S_{11} & S_{12} & S_{13} & 0 & 0 & S_{16} \\ S_{21} & S_{22} & S_{23} & 0 & 0 & S_{26} \\ S_{31} & S_{32} & S_{33} & 0 & 0 & S_{36} \\ 0 & 0 & 0 & S_{44} & S_{45} & 0 \\ 0 & 0 & 0 & S_{54} & S_{55} & 0 \\ S_{61} & S_{62} & S_{63} & 0 & 0 & S_{66} \end{bmatrix} \quad (2.8)$$

A material is called **orthotropic material**, if three orthogonal symmetry planes exist. Due to symmetry, the number of independent components is reduced to 9. If the coordinate system is chosen so that the axes are perpendicular to the planes of symmetry, the stiffness or compliance matrix will have the zero/nonzero components shown in equation (2.9). In this case, shear and extension are completely decoupled.

$$\mathbf{S} = \begin{bmatrix} S_{11} & S_{12} & S_{13} & 0 & 0 & 0 \\ S_{21} & S_{22} & S_{23} & 0 & 0 & 0 \\ S_{31} & S_{32} & S_{33} & 0 & 0 & 0 \\ 0 & 0 & 0 & S_{44} & 0 & 0 \\ 0 & 0 & 0 & 0 & S_{55} & 0 \\ 0 & 0 & 0 & 0 & 0 & S_{66} \end{bmatrix} \quad (2.9)$$

Transversely isotropic materials are a special case of orthotropic materials in which one plane is isotropic. As for orthotropic material, the coordinate system is chosen to coincide the symmetry planes, but the x_1 -axis is perpendicular to the plane of isotropy as shown in figure 2.5. Due to isotropy, the number of independent components is reduced to 5. An example of transversely isotropic materials are unidirectional FRP layers, which are described in more detail in the following section.

If an orthotropic or transversely isotropic material is rotated about the x_3 -axis, i.e. x_1 and x_2 are no longer normals of the symmetry planes, the stiffness or compliance matrix has the same zero/non-zero components as shown in equation (2.8). In other words, on-axis plies behave orthotropically or transversely isotropically and off-axis plies behave monoclinically.

2.4 Unidirectional Layer

In an unidirectional layer (UD-layer), all fibers are orientated in the same direction, i.e. the longitudinal direction. The coordinate system is chosen as described in the previous chapter for transversely isotropic materials, so that the x_1 -axis is aligned with the fiber direction and the x_2 -axis and x_3 -axis are in the plane of isotropy as shown on figure 2.5.

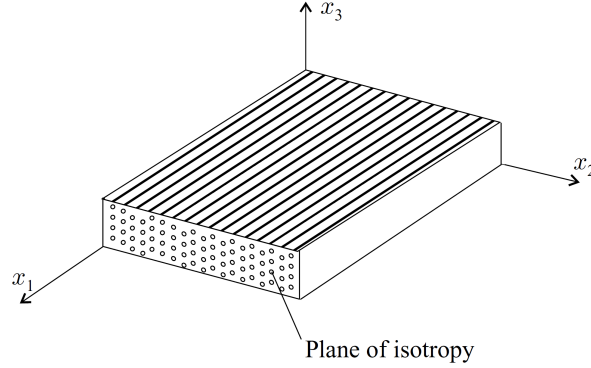


Figure 2.5: Coordinate system aligned with the fiber direction for unidirectional layers, adapted from (Kollar and Springer 2003, p. 19).

Being a special case of orthotropic materials, the compliance and stiffness matrices of unidirectional layers have the same zero/nonzero components as shown in equation (2.9). The engineering constants of UD-layer are derived taking into account the isotropy plane, which reduces the number of independent constants from nine to five. Engineering constants of transversely isotropic materials are related as follows:

$$\begin{aligned} E_3 &= E_2 \\ E_5 &= E_6 \\ \nu_{31} &= \nu_{21} \end{aligned}$$

The shear modulus E_4 in the x_2 - x_3 -plane is derived similar to the shear modulus for isotropic materials:

$$E_4 = \frac{E_2}{2(1 - \nu_{32})} \quad (2.10)$$

Finally, the on-axis compliance matrix in terms of engineering constants results in:

$$\mathbf{S} = \begin{bmatrix} \frac{1}{E_1} & -\frac{\nu_{12}}{E_2} & -\frac{\nu_{12}}{E_2} & 0 & 0 & 0 \\ -\frac{\nu_{21}}{E_1} & \frac{1}{E_2} & -\frac{\nu_{23}}{E_2} & 0 & 0 & 0 \\ -\frac{\nu_{21}}{E_1} & -\frac{\nu_{32}}{E_2} & \frac{1}{E_2} & 0 & 0 & 0 \\ 0 & 0 & 0 & \frac{2(1+\nu_{32})}{E_2} & 0 & 0 \\ 0 & 0 & 0 & 0 & \frac{1}{E_6} & 0 \\ 0 & 0 & 0 & 0 & 0 & \frac{1}{E_6} \end{bmatrix} \quad (2.11)$$

And the stiffness matrix is derived by inverting equation (2.11) $\mathbf{C} = \mathbf{S}^{-1}$.

Usually, lightweight structures made of composite materials are large in area but thin-walled, so that plane stress state can be considered. For plane stress, the following stress components are zero:

$$\sigma_3 = \sigma_4 = \sigma_5 = 0$$

And the stress-strain relation is reduced to:

$$\begin{aligned} \varepsilon_i &= S_{ij}\sigma_j \\ \sigma_i &= Q_{ij}\varepsilon_j \end{aligned} \quad i, j = 1, 2, 6 \quad (2.12)$$

where Q_{ij} are the components of the reduced in-plane stiffness matrix under plane stress condition. \mathbf{Q} is derived by modifying the 3-dimensional Hooke's law, which is shown in many books, including (Tsai 2008, pp. 19–22), (Tsai and José Daniel D. Melo 2015, pp. 31–36), and (Kollar and Springer 2003, pp. 38–42). The on-axis components for the reduced stiffness matrix Q_{ij} can be calculated as shown in equation (2.13):

$$\mathbf{Q} = \begin{bmatrix} \frac{E_1}{1 - \nu_{21}\nu_{12}} & \frac{\nu_{12}E_1}{1 - \nu_{21}\nu_{12}} & 0 \\ \frac{\nu_{21}E_2}{1 - \nu_{21}\nu_{12}} & \frac{E_2}{1 - \nu_{21}\nu_{12}} & 0 \\ 0 & 0 & E_6 \end{bmatrix} \quad (2.13)$$

2.5 Transformation of stress and strain

This section covers the transformation of stress and strain between two coordinate systems. The transformation relations are described in terms of engineering constants and are shown for a transformation about the z or x_3 , from on-axis to off-axis coordinate systems and vice versa. Note that on-axis stress and strains are designated by σ_{12} and ε_{12} , and off-axis by σ_{xy} and ε_{xy} .

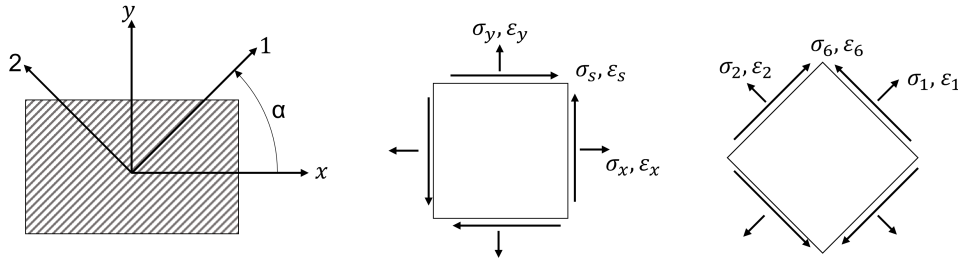


Figure 2.6: Sign convention for ply rotation angle and positive shear, adapted from (Schürmann 2007, p. 208) and (Tsai, José Daniel D. Melo, et al. 2017, p. 1).

The rotation angle α is defined positive for a counterclockwise rotation, i.e. a mathematical positive rotation, from off-axis (global) to on-axis (local) coordinate system. Besides the definition of a positive rotation angle, the definition for positive shear is shown in figure (2.6). Considering an equilibrium of forces and moments, the stress transformation can be easily derived. The strain

transformation can be derived by geometric relations before and after the element is deformed by normal and shear strain.

Both, the stress and the strain transformation relation are second-rank tensors. Considering engineering shear strain, transformation relations for stress and strain are different, because tensorial shear is defined half in value as engineering shear (Tsai 2008, pp. 25–29).

$$\varepsilon_{12} = \frac{\varepsilon_6}{2} \quad \varepsilon_{xy} = \frac{\varepsilon_s}{2} \quad (2.14)$$

The transformation of stress and strain from on-axis to off-axis and vice versa is shown in equations (2.15), (2.16), (2.17), and (2.18), where the following abbreviations are made:

$$\begin{aligned} m &= \cos(\alpha) \\ n &= \sin(\alpha) \end{aligned}$$

Stress Transformation

The stress transformation from on-axis to off-axis coordinate system:

$$\begin{aligned} \sigma_{xy} &= \mathbf{T}_\sigma \sigma_{12} \\ \begin{bmatrix} \sigma_x \\ \sigma_y \\ \sigma_s \end{bmatrix} &= \begin{bmatrix} m^2 & n^2 & -2mn \\ n^2 & m^2 & 2mn \\ mn & -mn & m^2 - n^2 \end{bmatrix} \begin{bmatrix} \sigma_1 \\ \sigma_2 \\ \sigma_6 \end{bmatrix} \end{aligned} \quad (2.15)$$

The stress transformation from off-axis to on-axis coordinate system is performed by inverting the transformation tensor \mathbf{T}_σ according to:

$$\begin{aligned} \sigma_{12} &= \mathbf{T}_\sigma^{-1} \sigma_{xy} \\ \begin{bmatrix} \sigma_1 \\ \sigma_2 \\ \sigma_s \end{bmatrix} &= \begin{bmatrix} m^2 & n^2 & 2mn \\ n^2 & m^2 & -2mn \\ -mn & mn & m^2 - n^2 \end{bmatrix} \begin{bmatrix} \sigma_x \\ \sigma_y \\ \sigma_s \end{bmatrix} \end{aligned} \quad (2.16)$$

Strain Transformation

The strain transformation tensor is denoted \mathbf{T}_ε and differs from the stress transformation tensor \mathbf{T}_σ because engineering shear strain is used.

$$\begin{aligned} \varepsilon_{xy} &= \mathbf{T}_\varepsilon \varepsilon_{12} \\ \begin{bmatrix} \varepsilon_x \\ \varepsilon_y \\ \varepsilon_s \end{bmatrix} &= \begin{bmatrix} m^2 & n^2 & -mn \\ n^2 & m^2 & mn \\ 2mn & -2mn & m^2 - n^2 \end{bmatrix} \begin{bmatrix} \varepsilon_1 \\ \varepsilon_2 \\ \varepsilon_6 \end{bmatrix} \end{aligned} \quad (2.17)$$

And the transformation from off-axis to on-axis

$$\begin{aligned} \varepsilon_{12} &= \mathbf{T}_\varepsilon^{-1} \varepsilon_{xy} \\ \begin{bmatrix} \varepsilon_1 \\ \varepsilon_2 \\ \varepsilon_6 \end{bmatrix} &= \begin{bmatrix} m^2 & n^2 & mn \\ n^2 & m^2 & -mn \\ -2mn & 2mn & m^2 - n^2 \end{bmatrix} \begin{bmatrix} \varepsilon_x \\ \varepsilon_y \\ \varepsilon_s \end{bmatrix} \end{aligned} \quad (2.18)$$

The transformation tensors for stress and strain are related:

$$\begin{aligned} \mathbf{T}_\sigma &= \mathbf{T}_\varepsilon^{-T} \\ \mathbf{T}_\sigma^{-1} &= \mathbf{T}_\varepsilon^T \end{aligned}$$

Using Mohr’s circle to transform stresses and strains shows that there are invariants within the aforementioned transformations. Invariants are combinations of stress or strain components that remain constant under coordinate transformation. Table 2.4 shows the respective transformation variables for stress and strain for the application of Mohr’s circle. One invariant is the center p of Mohr’s circle which represents the average stress or strain, and a second invariant is the radius R . The principal stresses/strains are invariant as per definition because they are the sum of p and $\pm R$. Figure 2.7 shows Mohr’s circle where all invariants can be seen. In strain space $\varepsilon_s/2$ is used because of engineering shear.

Table 2.4: Transformation variables for stress and strain in Mohr’s circle, adapted from (Tsai 2008, p. 27).

	p	q	r	$\tan(2\alpha_0)$	R^2	Principal
Stress	$\frac{\sigma_x + \sigma_y}{2}$	$\frac{\sigma_x - \sigma_y}{2}$	σ_s	$\frac{2\sigma_s}{\sigma_x - \sigma_y}$	$q^2 + r^2$	$p \pm R$
Strain	$\frac{\varepsilon_x + \varepsilon_y}{2}$	$\frac{\varepsilon_x - \varepsilon_y}{2}$	$\frac{\varepsilon_s}{2}$	$\frac{\varepsilon_s}{\varepsilon_x - \varepsilon_y}$	$q^2 + r^2$	$p \pm R$

Mohr’s circle is an important tool for the creation of failure envelopes that will be shown in chapter 2.8. A ply rotation in the laminate corresponds to a rotation by a doubled angle in the Mohr’s space and failure envelopes of various ply angles can be created by simple rigid body rotations (Tsai 2008, p. 28).

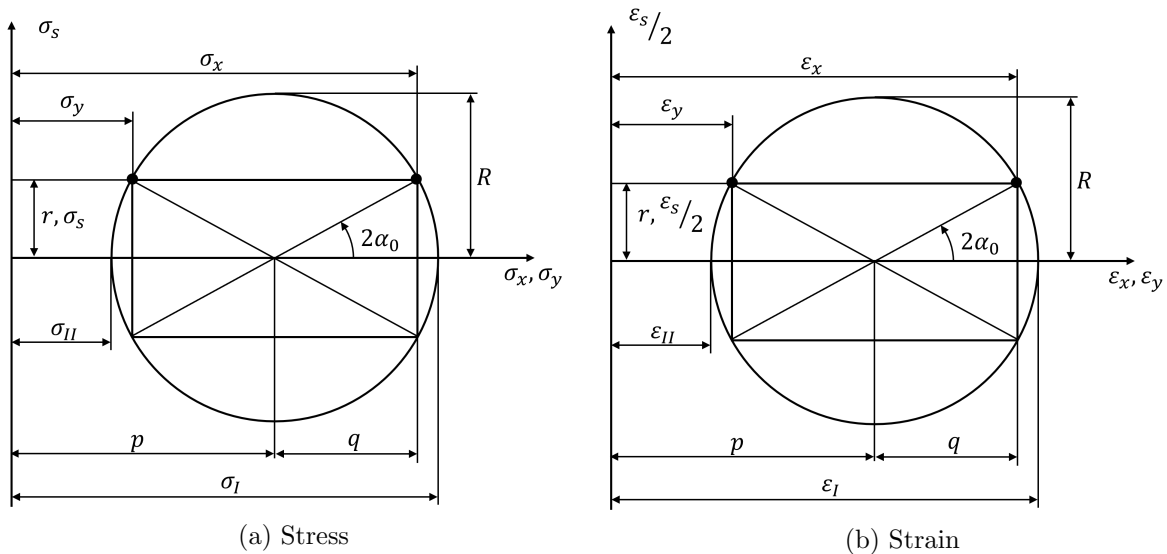


Figure 2.7: Mohr’s circle representation of stress and its principal components, adapted from (Tsai 2008, p. 28).

2.6 Transformation of stiffness

In addition to stress and strain, the stiffness and compliance of a material can also be transformed between different coordinate systems. The transformation relations depend directly on the transformations of stress and strain as shown in the following.

The stress terms σ_{xy} and σ_{12} in transformation equation (2.15)

$$\sigma_{xy} = \mathbf{T}_\sigma \sigma_{12}$$

are substituted, according to Hooke's law for on-axis and off-axis, by:

$$\begin{aligned}\sigma_{12} &= \mathbf{Q}_{12} \varepsilon_{12} \\ \sigma_{xy} &= \mathbf{Q}_{xy} \varepsilon_{xy}\end{aligned}$$

The substitution yields

$$\mathbf{Q}_{xy} \varepsilon_{xy} = \mathbf{T}_\sigma \mathbf{Q}_{12} \varepsilon_{12}$$

where ε_{12} is further substituted with equation (2.18):

$$\mathbf{Q}_{xy} \varepsilon_{xy} = \mathbf{T}_\sigma \mathbf{Q}_{12} \mathbf{T}_\varepsilon^{-1} \varepsilon_{xy}$$

Finally, the relation between on-axis and off-axis stiffness results in

$$\mathbf{Q}_{xy} = \mathbf{T}_\sigma \mathbf{Q}_{12} \mathbf{T}_\varepsilon^{-1} \quad (2.19)$$

and

$$\mathbf{Q}_{12} = \mathbf{T}_\sigma^{-1} \mathbf{Q}_{xy} \mathbf{T}_\varepsilon \quad (2.20)$$

The transformation of compliance is performed similar, using the respective stress and strain transformations.

The transformation relations for stiffness under plane stress are fourth rank tensors. Considering contracted notation, a transformation matrix for stiffness can be derived, using the same abbreviations as for stiffness and strain transformation ($m = \cos(\alpha)$, $n = \sin(\alpha)$).

$$\begin{bmatrix} Q_{xx} \\ Q_{yy} \\ Q_{xy} \\ Q_{ss} \\ Q_{xs} \\ Q_{ys} \end{bmatrix} = \begin{bmatrix} m^4 & n^4 & 2m^2n^2 & 4m^2n^2 \\ n^4 & m^4 & 2m^2n^2 & 4m^2n^2 \\ m^2n^2 & m^2n^2 & m^4 + n^4 & -4m^2n^2 \\ m^2n^2 & m^2n^2 & -2m^2n^2 & (m^2 - n^2)^2 \\ m^3n & -mn^3 & mn^3 - m^3n & 2(mn^3 - m^3n) \\ mn^3 & -m^3n & m^3n - mn^3 & 2(m^3n - mn^3) \end{bmatrix} \begin{bmatrix} Q_{11} \\ Q_{22} \\ Q_{12} \\ Q_{66} \end{bmatrix} \quad (2.21)$$

The powered trigonometric terms can be rewritten in the form of multiple angles, which are easier to manipulate mathematically.

$$\begin{aligned}
 m^4 &= \frac{3 + 4 \cos(2\alpha) + \cos(4\alpha)}{8} \\
 n^4 &= \frac{3 - 4 \cos(2\alpha) + \cos(4\alpha)}{8} \\
 m^3 n &= \frac{2 \sin(2\alpha) + \sin(4\alpha)}{8} \\
 mn^3 &= \frac{2 \sin(2\alpha) - \sin(4\alpha)}{8} \\
 m^2 n^2 &= \frac{1 - \cos(4\alpha)}{8}
 \end{aligned} \tag{2.22}$$

By substitution of equation (2.22) into equation (2.21), the relation between on-axis and off-axis stiffness can be rewritten as:

$$\begin{bmatrix} Q_{xx} \\ Q_{yy} \\ Q_{xy} \\ Q_{ss} \\ Q_{xs} \\ Q_{ys} \end{bmatrix} = \begin{bmatrix} U_1 & U_2 & U_3 & 0 & 0 \\ U_1 & -U_2 & U_3 & 0 & 0 \\ U_4 & 0 & -U_3 & 0 & 0 \\ U_5 & 0 & -U_3 & 0 & 0 \\ 0 & 0 & 0 & \frac{U_2}{2} & U_3 \\ 0 & 0 & 0 & \frac{U_2}{2} & -U_3 \end{bmatrix} \begin{bmatrix} 1 \\ \cos(2\alpha) \\ \cos(4\alpha) \\ \sin(2\alpha) \\ \sin(4\alpha) \end{bmatrix} \tag{2.23}$$

The new formulation of the stiffness transformation (2.23) is separated into two sets, material dependencies in U and geometry in trigonometric functions of double and quadruple angles. U_i are linear combinations of the on-axis stiffness \mathbf{Q}_{12} , where U_1 , U_4 and U_5 are invariant, U_2 and U_3 are not. U_1 can be considered as the total stiffness potential of an anisotropic material. U_2 and U_3 are responsible for the anisotropy of the ply material and are zero for isotropic materials. The contribution of the respective stiffness components to U_i is shown in table 2.5.

Table 2.5: linear combinations of on-axis stiffness moduli, adapted from (Tsai and José Daniel D. Melo 2015, p. 62).

	Q_{11}	Q_{22}	Q_{12}	Q_{66}	invariant?
$U_1 = U_4 + 2U_5$	3/8	3/8	1/4	1/2	yes
U_2	1/2	-1/2	0	0	no
U_3	1/8	1/8	-1/4	-1/2	no
$U_4 = U_1 - 2U_5$	1/8	1/8	3/4	-1/2	yes
$U_5 = (U_1 - U_4)/2$	1/8	1/8	-1/4	1/2	yes

Linear combinations of invariant U_i are also invariant. For example the trace, i.e. Tsai's modulus, of the stiffness matrix $\text{tr}(\mathbf{Q})$ can be derived by such linear combinations. The respective shear component must be multiplied by factor 2, as engineering shear is used.

$$\text{tr}(\mathbf{Q}) = Q_{11} + Q_{22} + 2Q_{66} = Q_{xx} + Q_{yy} + 2Q_{ss} = 2(U_1 + U_5) \tag{2.24}$$

Since invariants remain constant at whatever angle, they are crucial for the design of multidirectional laminates.

2.7 Classical Laminate Theory

The structural response of a multidirectional composite laminate can be derived using the classical laminate theory (CLT). It can be used to calculate both, the global deformations and those of the individual plies, and to determine the ply stresses from ply strains.

The classical laminate theory is an extension of the Kirchhoff-Love plate theory (classical plate theory) to composite laminates, which itself is an extension of the Euler-Bernoulli-beam theory to thin plates. The following assumptions apply to the classical plate theory (Reddy 2004, p. 113):

- Straight lines perpendicular to the midsurface (i.e. transverse normals) before deformation remain straight after deformation
- The transverse normals do not experience elongation
- The transverse normals rotate such that they remain perpendicular to the mid-surface after deformation

Furthermore, the extension to composite laminates assumes (Mallick 2008, p. 183):

- The laminate is thin and wide (width \gg thickness)
- A perfect interlaminar bond exists between various laminas
- Strain distribution in the thickness direction is linear
- All laminas are macroscopically homogeneous and behave in a linearly elastic manner

The force and moment resultants are applied to the mid surface of a laminate as shown in figure 2.8. For bending and twisting moments, the sign convention differs from other engineering fields, e.g. M_x and M_y bend the plate, while M_{xy} twists the plate.

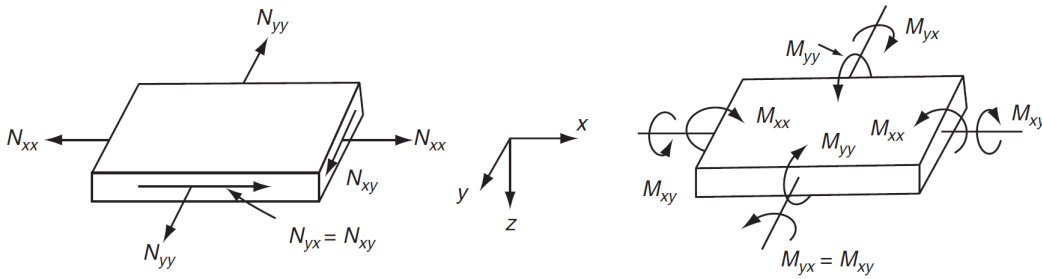


Figure 2.8: In-plane, bending, and twisting loads applied to a laminate (Mallick 2008, p. 185).

Considering a laminated plate, where x and y are in-plane and z out-of-plane, and the respective displacements u^o , v^o , and w^o . The strains ε_i^o and curvatures κ_i of the reference plane are:

$$\begin{aligned} \varepsilon_x^o &= \frac{\partial u^o}{\partial x} & \varepsilon_y^o &= \frac{\partial v^o}{\partial y} & \varepsilon_s^o &= \frac{\partial u^o}{\partial y} + \frac{\partial v^o}{\partial x} \\ \kappa_x &= -\frac{\partial^2 w^o}{\partial x^2} & \kappa_y &= -\frac{\partial^2 w^o}{\partial y^2} & \kappa_s &= -\frac{2\partial^2 w^o}{\partial x \partial y} \end{aligned} \quad (2.25)$$

According to the above made assumptions, the laminate strains are linearly related to the distance z from the mid plane:

$$\boldsymbol{\varepsilon} = \begin{bmatrix} \varepsilon_x^o \\ \varepsilon_y^o \\ \varepsilon_s^o \end{bmatrix} + z \begin{bmatrix} \kappa_x \\ \kappa_y \\ \kappa_s \end{bmatrix} \quad (2.26)$$

The resulting forces and moments (N_i, M_i) are derived by integrating the stress across the laminate thickness, and since the stresses are not continuous through the thickness, a lamina-wise integration is required. The stresses $\boldsymbol{\sigma}_k$ of each layer k depend on the respective stiffness matrix $\mathbf{Q}_{xy,k}$ and strains $\boldsymbol{\varepsilon}_k$.

$$\mathbf{N} = \int_{h_b}^{h_t} \boldsymbol{\sigma} dz = \sum_{k=1}^K \int_{z_{k-1}}^{z_k} \boldsymbol{\sigma}_k dz = \sum_{k=1}^K \int_{z_{k-1}}^{z_k} \mathbf{Q}_{xy,k} \boldsymbol{\varepsilon}_k dz \quad (2.27)$$

$$\mathbf{M} = \int_{h_b}^{h_t} \boldsymbol{\sigma} z dz = \sum_{k=1}^K \int_{z_{k-1}}^{z_k} \boldsymbol{\sigma}_k z dz = \sum_{k=1}^K \int_{z_{k-1}}^{z_k} \mathbf{Q}_{xy,k} \boldsymbol{\varepsilon}_k z dz \quad (2.28)$$

By substituting equation (2.26) into the equations (2.27) and (2.28), the load-strain relation can be represented as

$$\begin{bmatrix} \mathbf{N} \\ \mathbf{M} \end{bmatrix} = \begin{bmatrix} \mathbf{A} & \mathbf{B} \\ \mathbf{B} & \mathbf{D} \end{bmatrix} \begin{bmatrix} \boldsymbol{\varepsilon}^o \\ \boldsymbol{\kappa} \end{bmatrix} \quad (2.29)$$

where \mathbf{A} is the extensional stiffness matrix, \mathbf{D} is the bending stiffness matrix, and \mathbf{B} is the bending-extensional coupling stiffness matrix. The respective matrix components are

$$\begin{aligned} A_{ij} &= \sum_{k=1}^K Q_{xy,k,ij} (z_k - z_{k-1}) \\ B_{ij} &= \frac{1}{2} \sum_{k=1}^K Q_{xy,k,ij} (z_k^2 - z_{k-1}^2) \\ D_{ij} &= \frac{1}{3} \sum_{k=1}^K Q_{xy,k,ij} (z_k^3 - z_{k-1}^3) \end{aligned} \quad (2.30)$$

where $Q_{xy,k,ij}$ is the stiffness component ij ($i, j = 1, 2, 6$) belonging to layer k in the laminate coordinate system.

$$\begin{bmatrix} \mathbf{A} & \mathbf{B} \\ \mathbf{B} & \mathbf{D} \end{bmatrix} = \begin{bmatrix} A_{11} & A_{12} & A_{16} & B_{11} & B_{12} & B_{16} \\ A_{21} & A_{22} & A_{26} & B_{21} & B_{22} & B_{26} \\ A_{61} & A_{62} & A_{66} & B_{61} & B_{62} & B_{66} \\ B_{11} & B_{12} & B_{16} & D_{11} & D_{12} & D_{16} \\ B_{21} & B_{22} & B_{26} & D_{21} & D_{22} & D_{26} \\ B_{61} & B_{62} & B_{66} & D_{61} & D_{62} & D_{66} \end{bmatrix} \quad (2.31)$$

Multiplying equation (2.29) by the inverse of \mathbf{ABD} yields the laminate strain $\boldsymbol{\varepsilon}$ for an external load \mathbf{N}, \mathbf{M} . Since the stiffness matrix and the transformation relations for stress, strain and stiffness are known (Eqs. 2.16, 2.18 and 2.21), the on-axis ply stresses and strains can be calculated. The on-axis stresses and strains can then be used for strength analysis of the laminate.

The in-plane stiffness components A_{ij} depend on the ply orientations in the laminate, while D_{ij} additionally depend on the stacking order of plies. Furthermore, the ABD-matrices describe the response of a laminate to in-plane forces and moments (Kollar and Springer 2003, pp. 72–73):

- extension-shear coupling, $A_{16} \neq 0, A_{26} \neq 0$
- bending-twist coupling, $D_{16} \neq 0, D_{26} \neq 0$
- extension-twist and bending-shear coupling, $B_{16} \neq 0, B_{26} \neq 0$
- in-plane-out-of-plane coupling, $B_{ij} \neq 0$
- extension-extension coupling, $A_{12} \neq 0$
- bending-bending coupling, $D_{12} \neq 0$

If a laminate is build symmetric with respect to the mid-plane, i.e. material properties, locations, and lamination scheme are symmetric about the mid-plane, the coupling stiffness are zero ($B_{ij} = 0$). If the material properties and locations are symmetric about the mid-plane, but the sign of the ply angles is opposite, a laminate is called antisymmetric. For antisymmetric laminates the following components are zero: $A_{16} = A_{26} = D_{16} = D_{26} = 0$. In a balanced laminate, for each $+\alpha$ ply there is a corresponding $-\alpha$ ply, independent of the particular z -location, and the following components are zero: $A_{16} = A_{26} = 0$. A laminate exhibits in-plane isotropy if it consists of three or more plies oriented at the same relative angle α to adjacent plies, i.e. $\alpha = \pi/I$, where I is the total number of fiber orientations ($I \geq 3$). Due to their in-plane isotropy, such laminates are also called black aluminum. The stiffness components are related as follows: $A_{11} = A_{22}$, $A_{66} = (A_{11} - A_{12})/2$, and $A_{16} = A_{26} = 0$ (Reddy 2004, pp. 148–156).

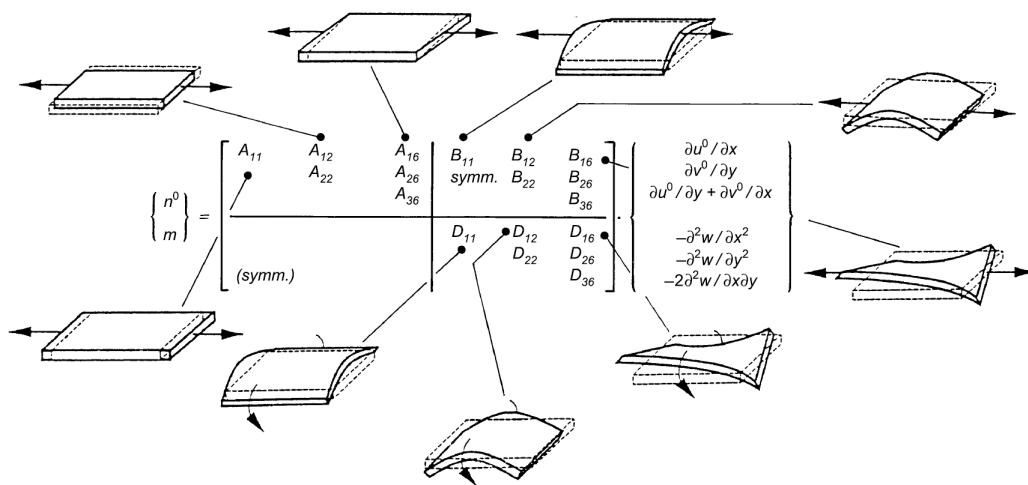


Figure 2.9: Components of ABD and their effects on the laminates response (Verein Deutscher Ingenieure 2006, p. 61).

2.8 Failure Criteria

Lightweight components are generally designed to utilize almost the entire material capacity. A strength analysis based on failure criteria is performed to verify that a stress or strain state is within the allowable range, to determine safety factors and to compare different laminate designs. Besides, the strength analysis is useful for optimization to determine best ply orientations, stacking sequences and laminate thicknesses. For example, a fail-safe design can be achieved by designing the laminate so that failure does not occur immediately, but rather evolutionarily, with sufficient reserves in the plies adjacent to the failing ply. The first occurrence of failure within a laminate is referred as first ply failure FPF and the total failure as last ply failure LPF.

During a strength analysis, failure criteria are commonly used to compare stress states with material strength parameter. Referring to isotropic materials, the equivalent von-Mises stress is such a criterion and is commonly compared with the materials tensile strength. For composites, the strength analysis is much more complicated because there are different failure modes depending on the loading direction. Furthermore, plies within the laminate are loaded differently, with failure starting in the highest stressed layer and continuing ply-by-ply. In addition, Cracks reduce the ply stiffness, resulting in a redistribution of stress to adjacent plies. The larger the crack, the more stress is redistributed. Since failure is not a single event but an evolutionary process, a degradation analysis is also performed to account for degraded ply stiffnesses (Schürmann 2007, pp. 393–397). FRP materials have different strength characteristics for tension and compression in longitudinal and transverse direction and for longitudinal shear. For a unidirectional layer, tensile failure in fiber direction is designated by X, compressive failure by X'. Transverse to the fiber direction, tensile failure is designated by Y, compressive failure Y'. Longitudinal shear failure is designated by S. The five different failure modes of an unidirectional layer and their respective designations are also shown in figure 2.10.

Over the years, many failure theories have been developed by various authors to represent the different failure modes. 19 of leading failure theories are tested and compared against each other and experimental data in the World Wide Failure Exercise (M. Hinton, P. D. Soden, and A.-S. Kaddour 2004). The theories included in the aforementioned book are divided into interactive failure criteria, physically based failure criteria, and damage mechanics. The former are theories evolved from those for yielding of metals, physically based failure criteria take into account the different failure modes of FRP and can provide predictions of the mode of failure, and last, damage mechanics describes the whole process of failure from damage initiation, evolution and final fracture and also considers delamination (M. Hinton, P. D. Soden, and A.-S. Kaddour 2004, pp. 11–12). While the latter two families of criteria are usually complicated, interactive failure criteria are rather simple and can be easily implemented in a design algorithm.

Four theories for predicting failure that make laminate optimization computationally favorable are described in the following. Starting with the Tsai-Wu failure criteria, an interactive failure theory included in the aforementioned work and the basis for the theories that follow. In Addition, a simplified approach for considering material behavior after FPF for multidirectional laminates is given.

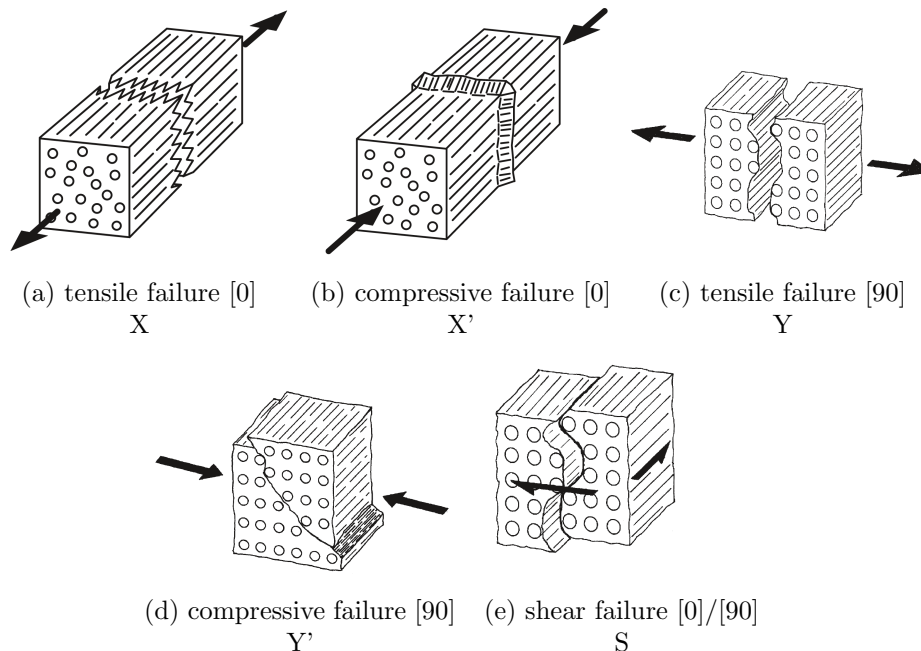


Figure 2.10: Failure modes of unidirectional layer and their respective designation, adapted from (Schürmann 2007, pp. 347, 351, 364, 365, 366).

Strength ratio

Before explaining the different failure criteria, the strength ratio R or the failure index k is described here. The strength ratio is the relationship between the maximum, ultimate or allowable stress and the applied stress (Tsai and José Daniel D. Melo 2015, p. 72).

Assuming that the composite is linear elastic and for each combined stress state there is a corresponding combined strain state, the strength ratio for stress and strain is the same:

$$\begin{aligned}\sigma_{max} &= R\sigma_{applied} \\ \varepsilon_{max} &= R\varepsilon_{applied}\end{aligned}\tag{2.32}$$

Where σ_{max} , consequently ε_{max} is defined by the chosen failure criterion. The strength ratio R can be used for laminate design since it is a simple scaling parameter:

- $R = 1$ failure occurs
- $R > 1$ the applied load can be increased or the laminate thickness can be reduced
- $R < 1$ the applied load has to be reduced or the laminates thickness has to be increased

For example, $R = 2$ means that the load can be doubled or the thickness can be halved before failure occurs. On the other hand, $R = 0.5$ means that the load has to be reduced by half or the laminate has to be doubled. Note that the strength ratio has a physical meaning only for $R \geq 1$. Besides the strength ratio R , the failure index k and the FEA index K are often used within finite element software where k is simply the reciprocal of R :

$$k = \frac{1}{R}\tag{2.33}$$

And can be used to scale the thickness of the laminate. In contrast, the FEA index K is disadvantageous because it cannot be used for scaling when tensile and compressive strengths are unequal.

Tsai-Wu failure criterion in stress space

The Tsai-Wu criterion (Tsai and Wu 1971) is a common quadratic failure criterion for composite materials. It is based on scalar products of stress or strain and is classified as interactive failure criterion. It does not provide information on failure modes, i.e. fiber and matrix failure for tension and compression are captured in one criterion which might be seen as a disadvantage. However, it is simply applicable and can be used for any loading direction.

The Tsai-Wu criteria assumes that a closed failure surface with an ellipsoidal shape exists in stress or strain space. Stress or strain conditions that are inside the body do not damage the material, while failure occurs for conditions outside.

The failure surface $f(\sigma_k)$ in stress space is defined as

$$f(\sigma_k) = F_{ij}\sigma_i\sigma_j + F_i\sigma_i = 1 \quad i, j, k = 1, 2, \dots, 6 \quad (2.34)$$

where F_i and F_{ij} are the materials strength tensors of the second and fourth rank, respectively. Performing uniaxial tension and compression tests, as well as pure shear tests, the parameters F_i and F_{ii} can be obtained. The off-diagonal interaction terms $F_{ij}, i \neq j$ are restricted by

$$F_{ii}F_{jj} - F_{ij}^2 \geq 0 \quad (2.35)$$

in order to ensure the failure surface intersects each stress axis and that it is closed, i.e. that the surface is ellipsoidal. The interaction terms F_{ij} may be written in form of a normalized interaction terms F_{ij}^* , where

$$F_{ij} = F_{ij}^* \sqrt{F_{ii}F_{jj}} \quad (2.36)$$

and F_{ij}^* is restricted in accordance to equation (2.35) by

$$-1 \leq F_{ij}^* \leq 1 \quad (2.37)$$

Assuming plane stress, equation (2.34) simplifies to

$$F_{11}\sigma_1^2 + 2F_{12}\sigma_1\sigma_2 + F_{22}\sigma_2^2 + F_{66}\sigma_6^2 + F_1\sigma_1 + F_2\sigma_2 = 1 \quad (2.38)$$

when expanded in the symmetry axes, which describes an envelope.

The strength parameters F_{ii} and F_i are obtained by substitution of the measured strength parameter X, X', Y, Y', S into equation (2.38) and solving the respective equations as shown in (Tsai 2008, p. 149).

$$\begin{aligned} F_{11} &= \frac{1}{XX'} & F_1 &= \frac{1}{X} - \frac{1}{X'} \\ F_{22} &= \frac{1}{YY'} & F_2 &= \frac{1}{Y} - \frac{1}{Y'} \\ F_{66} &= \frac{1}{S^2} \end{aligned} \quad (2.39)$$

By substitution of equation (2.39) into (2.38), the Tsai-Wu criterion can be written in its well-know formulation:

$$\frac{\sigma_1^2}{XX'} + \frac{2F_{12}^*\sigma_1\sigma_2}{\sqrt{XX'YY'}} + \frac{\sigma_2^2}{YY'} + \frac{\sigma_6^2}{S^2} + \left(\frac{1}{X} - \frac{1}{X'}\right)\sigma_1 + \left(\frac{1}{Y} - \frac{1}{Y'}\right)\sigma_2 = 1 \quad (2.40)$$

Taking into account failure mode interactions, i.e. changes in strength under multiaxial loading, the permissible range of the interaction term F_{12}^* can be narrowed down to

$$-1 \leq F_{12}^* \leq 0 \quad (2.41)$$

To achieve this, the admissible inclination of tangents to the failure envelopes at the four anchor points X, X', Y, Y' is investigated (Tsai 2008, pp. 153–159). It is shown that the new admissible range for the normalized interaction term F_{12}^* is valid for all FRP materials.

Usually, the interaction criterion is chosen as $F_{12}^* = -0.5$, because the well-known von-Mises criterion can be reconstructed by assuming isotropic material behavior and equal values for tensile and compressive strength (Tsai 2008, S. 151).

However, F_{12}^* can be adjusted to provide a better fit to test data for compression-compression loads (Millen and Aravand 2021, p. 5).

Note that stress space failure envelopes are dependent on the laminate layup, i.e. envelopes vary with the presence and absence of plies at a certain angle as the laminates compliance matrix changes. The derivation of FPF envelopes for multidirectional laminates is shown after the Tsai-Wu criterion in strain space, since this requires a transformation to strain space.

Tsai-Wu in strain space

The representation of failure envelopes in strain space is advantageous compared to stress space, since (Tsai and José Daniel D. Melo 2015, S. 238):

- Strain is usually specified in the CLT
- Failure envelopes in strain space are fixed and independent of plies with different orientations within the same laminate and therefore they can be seen as material properties
- Strains are dimensionless and therefore equal for SI and English units

The Tsai-Wu criterion in strain space is derived by substituting equation (2.12) $\sigma_i = Q_{ij}\varepsilon_j$ into the quadratic stress terms of equation (2.34):

$$F_{ij}\sigma_i\sigma_j = F_{ij}(Q_{ik}\varepsilon_k)(Q_{jl}\varepsilon_l) = (F_{ij}Q_{ik}Q_{jl})\varepsilon_k\varepsilon_l = G_{kl}\varepsilon_k\varepsilon_l \quad (2.42)$$

where $G_{kl} = Q_{ki}Q_{lj}F_{ij}$. Using the same approach for the linear stress terms yields:

$$F_i\sigma_i = F_i(Q_{ij}\varepsilon_j) = (F_iQ_{ij})\varepsilon_j = G_j\varepsilon_j \quad (2.43)$$

and $G_j = Q_{ji}F_i$.

G_j and G_{kl} are the second and fourth rank strength tensors in strain space, respectively.

Finally, the Tsai-Wu failure criteria in strain space for plane stress is obtained as

$$G_{ij}\varepsilon_i\varepsilon_j + G_i\varepsilon_i = 1 \quad i, j = 1, 2, 6 \quad (2.44)$$

and in its expanded on-axis formulation

$$G_{11}\varepsilon_1^2 + 2G_{12}\varepsilon_1\varepsilon_2 + G_{22}\varepsilon_2^2 + G_{66}\varepsilon_6^2 + G_1\varepsilon_1 + G_2\varepsilon_2 = 1 \quad (2.45)$$

Figure 2.11 a) shows a failure envelope for an interaction parameter $F_{12}^* = 0.5$ in strain space. Due to Poisson's ratio, the strength parameter X,X',Y,Y' in strain space do not lie on the coordinate axes. Furthermore, the major Poisson's ratio of the ply material is the negative slope of the connecting line between the strengths X' and X.

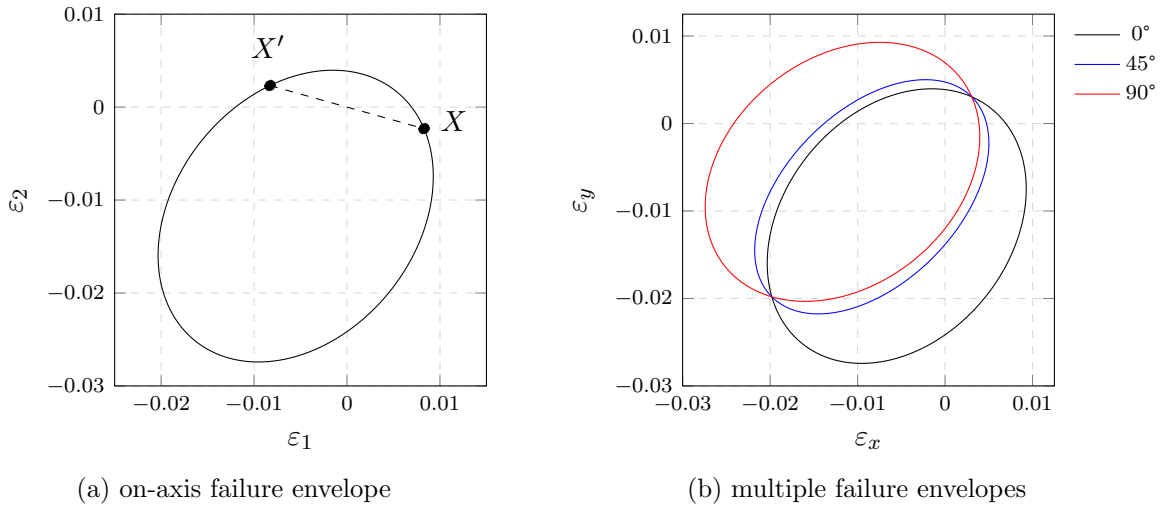


Figure 2.11: Tsai-Wu failure envelopes in strain space for on-axis and various off-axis ply orientations for T300-5208, adapted from (Tsai and José Daniel D. Melo 2015, p. 239).

The on-axis failure envelopes derived by equation (2.45) can be transformed to off-axis orientation, corresponding to the respective ply angle α . Such transformed failure envelopes are shown in figure 2.11 b) for different α . For the fourth and second rank strength tensors in strain space G_{ij}, G_i , the transformation relations are the same as for elastic stiffness and stress, respectively:

$$\begin{aligned}
 \begin{bmatrix} G_{xx} \\ G_{yy} \\ G_{xy} \\ G_{ss} \\ G_{xs} \\ G_{ys} \end{bmatrix} &= \begin{bmatrix} m^4 & n^4 & 2m^2n^2 & 4m^2n^2 \\ n^4 & m^4 & 2m^2n^2 & 4m^2n^2 \\ m^2n^2 & m^2n^2 & m^4 + n^4 & -4m^2n^2 \\ m^2n^2 & m^2n^2 & -2m^2n^2 & (m^2 - n^2)^2 \\ m^3n & -mn^3 & mn^3 - m^3n & 2(mn^3 - m^3n) \\ mn^3 & -m^3n & m^3n - mn^3 & 2(m^3n - mn^3) \end{bmatrix} \begin{bmatrix} G_{11} \\ G_{22} \\ G_{12} \\ G_{66} \end{bmatrix} \\
 \begin{bmatrix} G_x \\ G_y \\ G_s \end{bmatrix} &= \begin{bmatrix} m^2 & n^2 \\ n^2 & m^2 \\ mn & -mn \end{bmatrix} \begin{bmatrix} G_1 \\ G_2 \end{bmatrix}
 \end{aligned} \tag{2.46}$$

The criterion in the off-axis coordinate system, i.e. laminate coordinate system, results in :

$$G_{xx}\varepsilon_x^2 + G_{yy}\varepsilon_y^2 + G_{ss}\varepsilon_s^2 + 2G_{xy}\varepsilon_x\varepsilon_y + 2G_{xs}\varepsilon_x\varepsilon_s + 2G_{ys}\varepsilon_y\varepsilon_s + G_x\varepsilon_x + G_y\varepsilon_y + G_s\varepsilon_s = 1 \tag{2.47}$$

The transformation of strength in stress space is performed analogously using the transformation relations for elastic compliance and strain, which can be found in (Tsai 2008, p. 162).

This is a major advantage of the Tsai-Wu or quadratic failure criteria in general, since the failure analysis can be performed in any coordinate system.

First ply failure envelopes

First ply failure (FPF) envelopes are characterized by stress or strain states of a multidirectional laminate at which the first ply reaches a strength ratio $R = 1$, i.e. the first ply fails. In strain space, the respective failure envelopes of each ply-orientation can simply be superimposed and the resulting inner envelope is the FPF envelope. Superposition in stress space is not as simple as for strain space. With the presence or absence of plies in the laminate, the stiffness and compliance matrix alters and so do the stress failure envelopes. FPF envelopes in stress space require a transformation to strain space as shown above, followed by a transformation back to stress space, by the means of the laminates thickness normalized extensional compliance matrix $\mathbf{a}^n = \mathbf{a}/h$ (Tsai 2008, p. 173). Inserting the laminates in-plane stress-strain relation

$$\varepsilon_i^\circ = a_{ij}^n \sigma_j^\circ = \frac{1}{h} a_{ij} \sigma_j^\circ \quad (2.48)$$

into equation (2.44) yields

$$H_{ij} \sigma_i^\circ \sigma_j^\circ + H_i \sigma_i^\circ = 1 \quad (2.49)$$

where the strength parameter H_{ij} and H_i are calculated by

$$\begin{aligned} H_{ij} &= G_{kl} a_{ki}^n a_{lj}^n \\ H_i &= G_j a_{ji}^n \end{aligned} \quad (2.50)$$

Failure envelopes in stress space controlled by H_{ij} and H_i can be superimposed and as in strain space, the resulting inner envelope is the FPF envelope. Figure 2.12 a) and b) show two FPF envelopes in the stress space for the same material but with different number of $[0]$ plies. Figure 2.12 c) shows the failure envelopes in strain space that apply to both laminates a) and b). As mentioned before, failure envelopes in strain space are independent of the laminate, they are material properties.

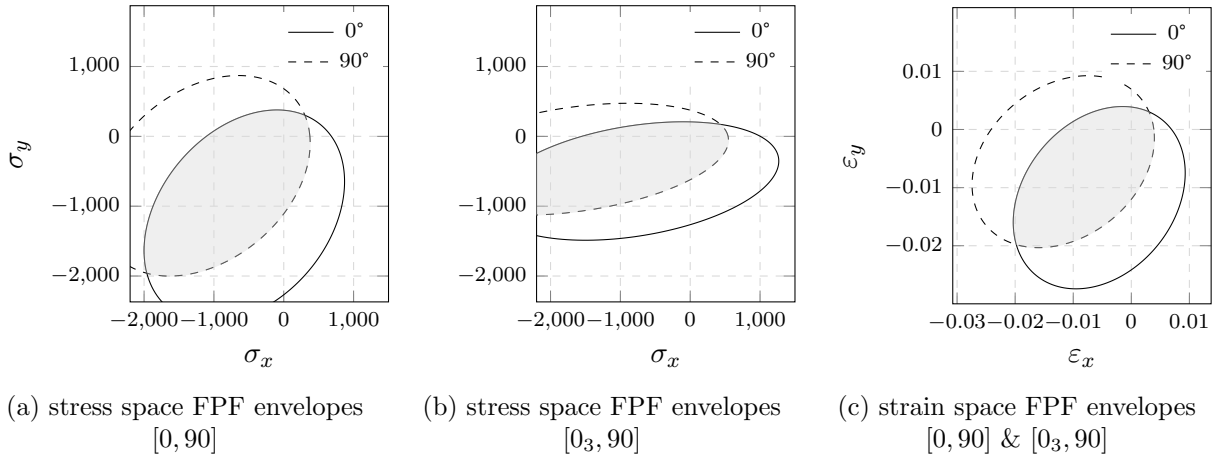


Figure 2.12: FPF envelopes in stress and strain space for altered laminate layups, adapted from (Tsai 2008, p. 173).

Omni Failure Criterion

The Omni failure criteria is based on strain space failure envelopes determined using tensor-based failure criteria such as the Tsai-Wu criterion. It is constructed similarly to FPF envelopes by superimposing failure envelopes, but taking into account all possible ply orientations, i.e. ply angles from 0 to 2π . The resulting inner envelope is called Omni failure envelope.

The Omni failure envelope is invariant because all possible ply orientations are covered. Furthermore, it is applied on laminate level, making a ply-by-ply strength analysis needless. Dependent on the selected material, different ply orientations contribute to the inner envelope. These plies are called controlling plies and can be determined by applying unit load vectors from 0 to 2π and identifying the particular ply that fails first. Since all possible ply orientations are covered, the Omni failure criterion represents a safe design independent of the laminates layup composition (Tsai and Jose Daniel D. Melo 2014, p. 242).

In figure 2.13, the construction of Omni envelopes is shown for two materials, T300-5208 and IM7 977-3. For both materials, the interaction term is chosen as $F_{12}^* = -0.5$ and the ply angle increments as $\Delta\alpha = 15^\circ$ to approximate the Omni envelope.

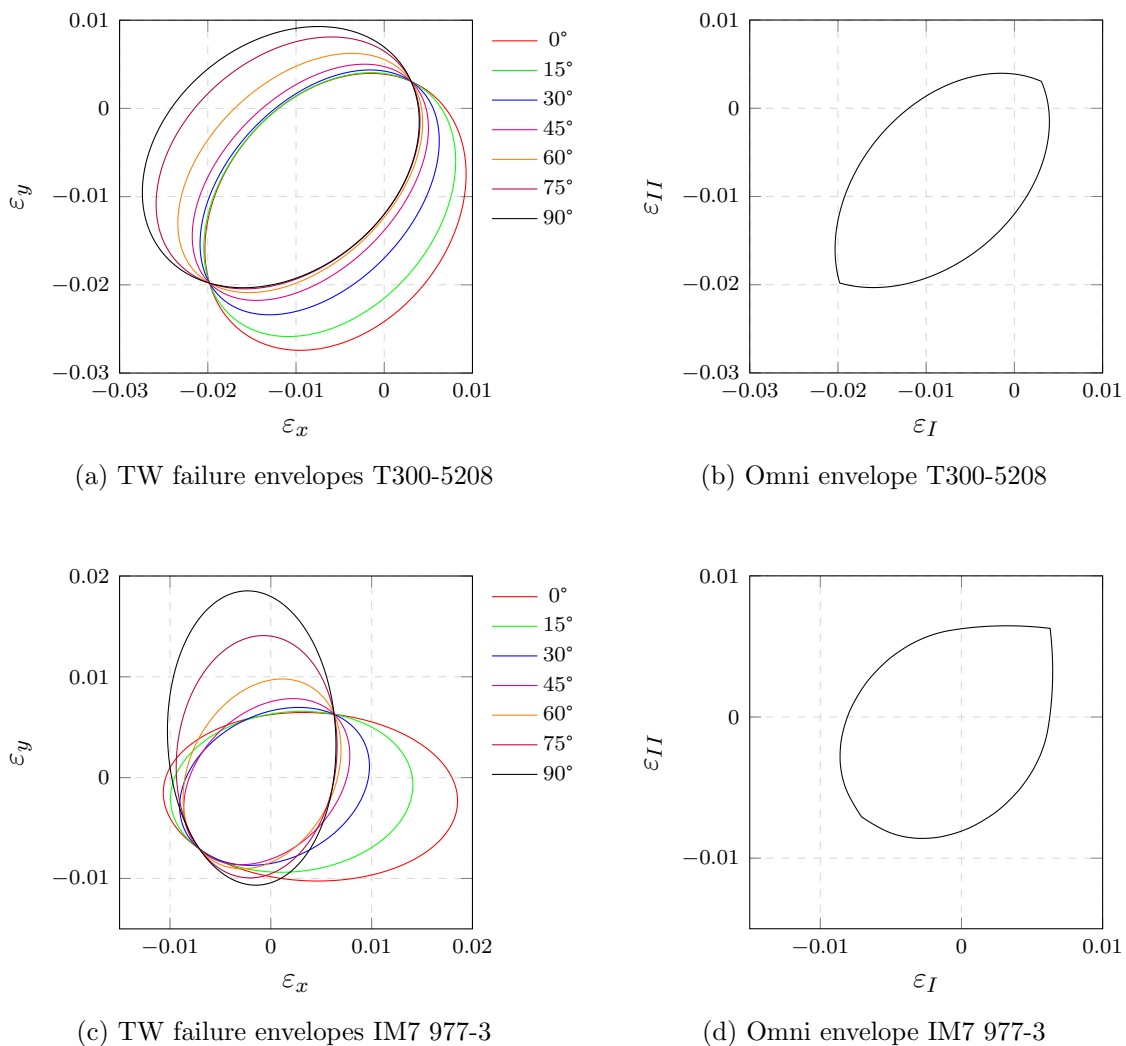


Figure 2.13: Superimposed Tsai-Wu failure envelopes and resulting Omni envelope for T300-5208 and IM7 977-3.

Material degradation after FPF

After a laminate encounters first ply failure, cracks occur within the matrix and the fibers resulting in degraded material properties. The degradation can occur in one or more plies simultaneous and degraded ply properties are derived by the means of micromechanics. Thus, the derivation of last ply failure (LPF) as well as the derivation of the laminate strength after FPF usually requires a progressive failure analysis of plies.

Depending on the transverse ply strain ε_2 , the ply can degrade twice for $\varepsilon_2 > 0$ and only once for $\varepsilon_2 \leq 0$. Assuming an initial strain $\varepsilon_2 > 0$, the matrix degrades by micro cracks and subsequently fiber failure leads to the second degradation. For $\varepsilon_2 \leq 0$, the initial degradation is directly caused by fiber failure (Tsai, José Daniel D. Melo, et al. 2017, p. 82).

A progressive failure analysis is an iterative process and therefore time consuming. In (Tsai and José Daniel D. Melo 2015, pp. 274–276) a simultaneous degradation approach is presented and shown to be a sufficient simplification of the failure analysis process for a homogeneous stress state. For simultaneous degradation, only matrix degradation is considered and instead of plies being degraded progressively, all plies are degraded at once as one ply reaches first-ply-failure. In addition, the ply with the lowest strength ratio yields the ultimate stress.

Among the various micromechanical formulations present for degraded ply properties, the following formulations for matrix degradation are suggested in (Tsai, José Daniel D. Melo, et al. 2017, pp. 83–84):

$$\begin{aligned}\tilde{E}_2 &= \frac{1 + \eta_2 \frac{1-\nu_f}{\nu_f}}{\frac{1}{E_2} + \frac{\eta_2 \frac{1-\nu_f}{\nu_f} (E_m^* E_m + E_2(1 - E_m^*))}{E_2 E_m^* E_m}} \\ \tilde{E}_6 &= \frac{1 + \eta_6 \frac{1-\nu_f}{\nu_f}}{\frac{1}{E_6} + \frac{\eta_6 \frac{1-\nu_f}{\nu_f} (E_m^* G_m + E_6(1 - E_m^*))}{E_6 E_m^* G_m}} \\ \tilde{\nu}_{21} &= E_m^* \nu_{21} \\ \tilde{F}_{xy}^* &= E_m^* F_{xy}^*\end{aligned}\tag{2.51}$$

Where η_2 and η_6 are stress partitioning parameters for transverse and shear, ν_f is the fiber volume fraction of the ply, G_m is the matrix shear modulus, and E_m^* is the matrix degradation factor. E_2 and E_6 are the ply materials transverse modulus and shear modulus. For most unidirectional composites, it was found the following parameters work best (Tsai, José Daniel D. Melo, et al. 2017, p. 84):

$$\begin{aligned}\eta_2 &= 0.516 \\ \eta_6 &= 0.316 \\ E_m^* &= 0.15\end{aligned}$$

Tsai-Wu and Omni failure envelopes for LPF

Failure envelopes for the same materials as in figure 2.13 are plotted in figure 2.14 but with degraded material properties. The envelopes in a) and c) are determined by the Tsai-Wu failure criterion and in b) and d), the respective inner, i.e. LPF, envelopes are shown.

For both materials, the controlling plies for LPF, i.e. the inner envelope, are the $[0^\circ]$ and $[90^\circ]$ plies. Furthermore, this accounts for all CFRP, as no CFRP has been found where the shear strength of other plies are significantly smaller to become the controlling plies (Tsai and Jose Daniel D. Melo 2016, p. 73).

For laminates containing these plies, LPF will always be controlled by them, and if they are not present in the laminate, the LPF Omni envelope will be conservative.

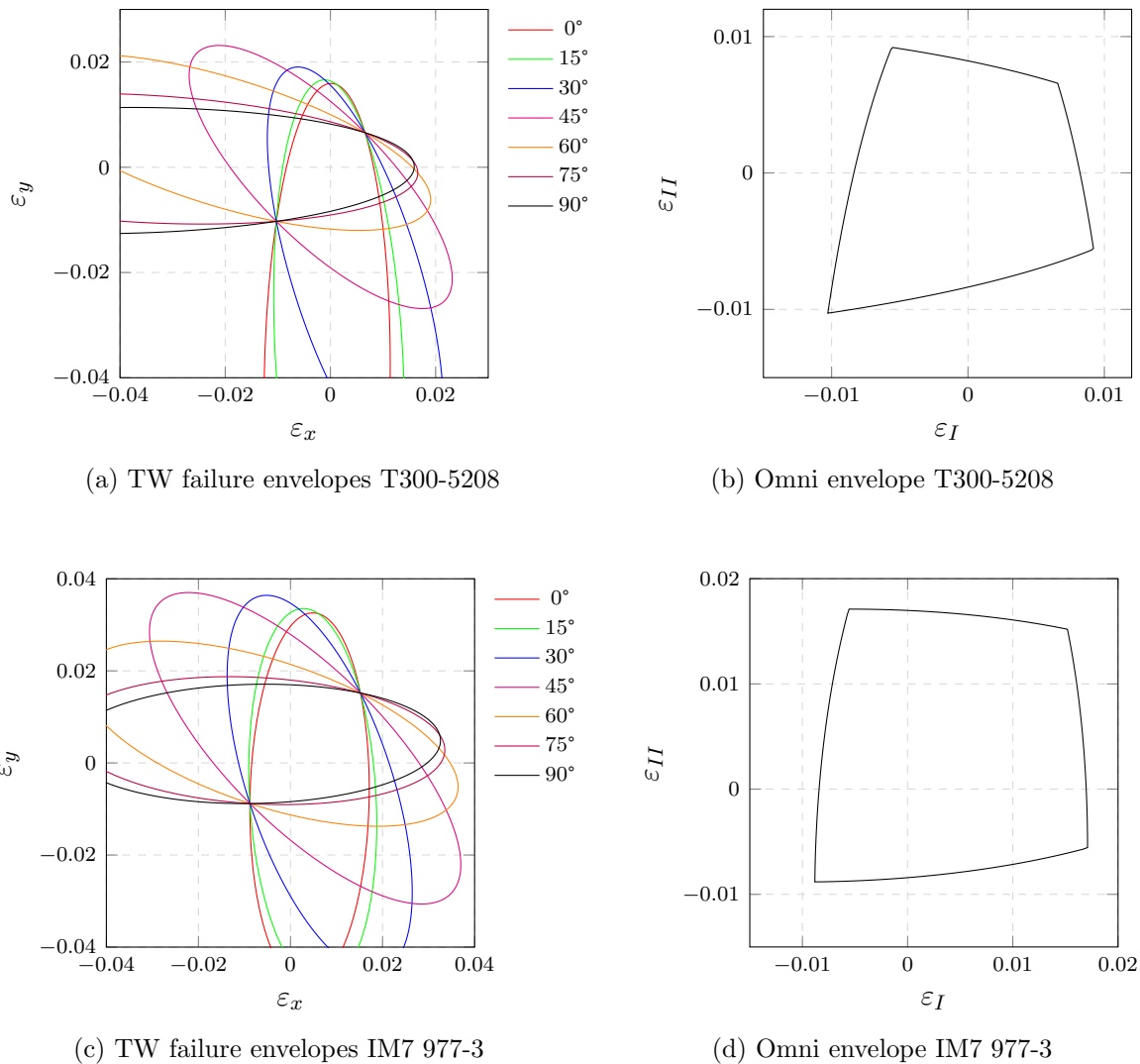


Figure 2.14: Superimposed Tsai-Wu LPF failure envelopes and resulting LPF Omni envelope for T300-5208 and IM7 977-3.

Unit Circle Failure Criterion

The unit circle failure criterion (Tsai and Jose Daniel D. Melo 2016) is derived by simplifications of the Omni failure envelope for LPF which are controlled by the failure envelopes of $[0^\circ]$ and $[90^\circ]$ ply for degraded material properties. Unit circle failure envelopes can be derived for any CFRP if the anchor points of a unit circle are multiplied with the respective failure strains ε_X and $\varepsilon_{X'}$ as shown in figure 2.15 a) and equation (2.52). Figure 2.15 b) shows the unit circle LPF failure envelope for IM7 977-3.

The unit circle failure envelope can be plotted according to the following equation:

$$\varepsilon_{uc} = \begin{bmatrix} \varepsilon_I \\ \varepsilon_{II} \end{bmatrix} = \begin{bmatrix} \cos(\phi)\varepsilon_{f1} \\ \sin(\phi)\varepsilon_{f2} \end{bmatrix} \quad \varepsilon_{f1} \begin{cases} \varepsilon_X, & \text{for } \frac{-\pi}{2} \leq \phi \leq \frac{\pi}{2} \\ \varepsilon_{X'}, & \text{for } \frac{\pi}{2} \leq \phi \leq \frac{3\pi}{2} \end{cases} \quad \varepsilon_X = \frac{X}{E_1} \quad (2.52)$$

$$\varepsilon_{f2} \begin{cases} \varepsilon_X, & \text{for } 0 \leq \phi \leq \pi \\ \varepsilon_{X'}, & \text{for } \pi \leq \phi \leq 2\pi \end{cases} \quad \varepsilon_{X'} = \frac{X'}{E_1}$$

There is a problem with obtaining the strains to failure directly from experiments since $[0]$ test coupons have a Poisson's ratio higher than zero. By considering degraded material properties the Poisson's ratio is approximately zero and the failure strains determined by uniaxial tests are essentially the same as the anchor points shown in figure 2.15 b) (Tsai and Jose Daniel D. Melo 2016, p. 73).

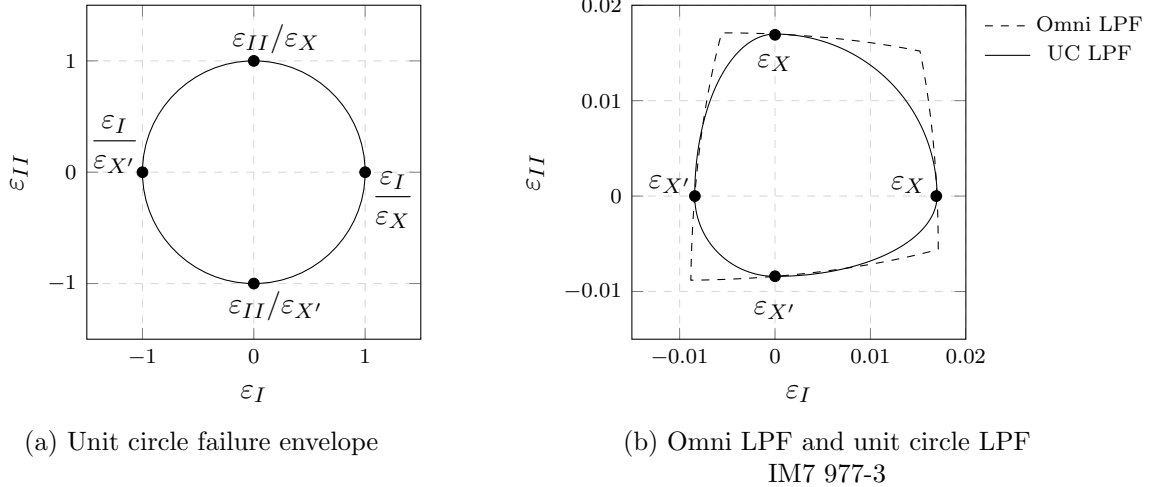


Figure 2.15: Unit circle failure envelope and anchor points obtained by Omni LPF envelope.

In (Tsai and Jose Daniel D. Melo 2016, pp. 75–77), the unit circle failure criterion is evaluated in terms reliability using experimentally obtained failure data from (P. Soden 1998) and (P. D. Soden, M. J. Hinton, and A. S. Kaddour 2002). It was found that a good correlation between prediction by unit circle and experimental data exist for tension-tension loads. Somewhat lower, but still good, is the correlation for tension-compression loads. For compression-compression loads, however, the correlation between theoretical and experimental data is low, which is attributed to buckling and the resulting reduction in strength.

In order to apply the advantages of the unit circle, i.e. the reduced amount of necessary test, to FPF envelopes, the Omni envelopes for FPF and LPF can be superimposed. The anchor points in compression are taken from the LPF envelope and for tension from the FPF envelope as shown in figure 2.16.

The anchor points for the FPF unit circle are derived by:

$$\begin{aligned} \varepsilon_Y &= \frac{Y}{E_2} \\ \varepsilon_{X'Y'} &= \min\left(\frac{X'}{E_1}, \frac{Y'}{E_2}\right) \end{aligned} \tag{2.53}$$

The anchor points in compression are defined either by the longitudinal compression failure strain or by the transverse compression failure strain of the material, dependent on which is the controlling one. In figure 2.16 a) the compressive failure strains in longitudinal direction X'/E_1 are applied and in b) the compressive failure strains in transverse direction Y'/E_2 .

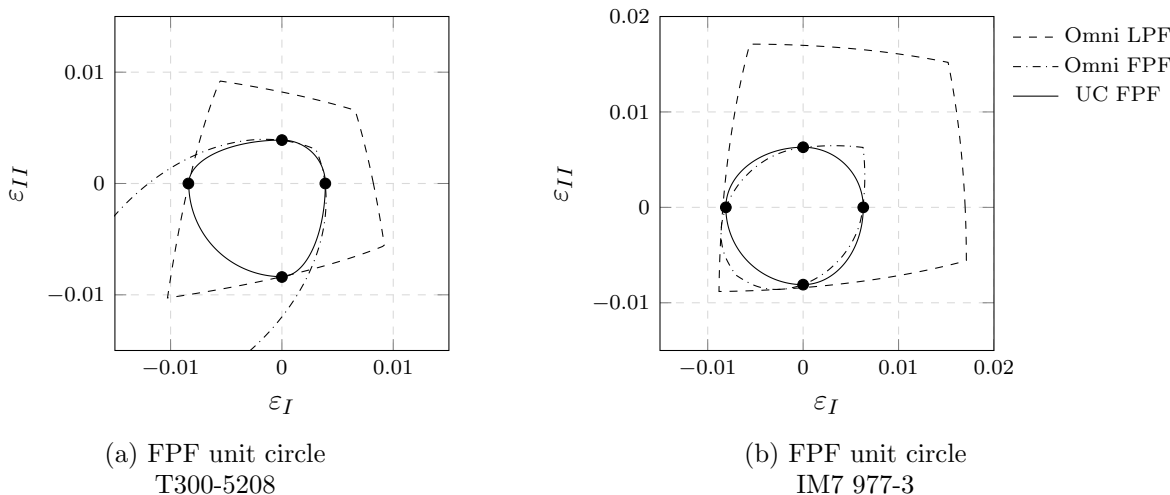


Figure 2.16: Unit circle FPF envelopes by superimposed Omni FPF and LPF envelopes.

Improvements in the accuracy of failure prediction are not the advantages of the unit circle criterion, but the mathematical simplicity, the reduced effort in producing strength parameters and the fact that it applies to all CFRP laminates regardless of ply orientations, are. In addition, due to its simplicity it can be easily implemented in design optimization algorithms (Tsai and Jose Daniel D. Melo 2016, p. 77).

Nettles circle

The Nettles circle is a simple and conservative failure criterion for FRP, where the strain is cut off at a fixed value. Either an experimentally determined value for FPF tensile strain or $\varepsilon_f = 0.004$ can be used. The latter is suggested by Allen Nettles and is the most conservative since no structure has been fabricated with a lower limit. Furthermore, the laminates damage tolerance against impacts is sufficiently guaranteed (Tsai 2021, p. 7). The radius can be chosen even smaller, making the Nettles circle more conservative. Figure 2.17 shows the Nettles circle for T300-5208 and IM7 977-3, additionally Omni LPF and FPF envelopes as well as FPF unit circles are included.

The Nettles circle envelope can be calculated by

$$\varepsilon_{nc} = \varepsilon_f \begin{bmatrix} \cos(\phi) \\ \sin(\phi) \end{bmatrix} \tag{2.54}$$

where ε_f represents the strain cutoff, i.e. the circle's radius. Since Nettles circle requires the least amount of data of all criteria presented, it can be applied directly for optimizing the preliminary laminate design. As mentioned above, $\varepsilon_f = 0.004$ can be used before determining the strength parameters of the material. This is especially useful when initial results need to be delivered quickly.

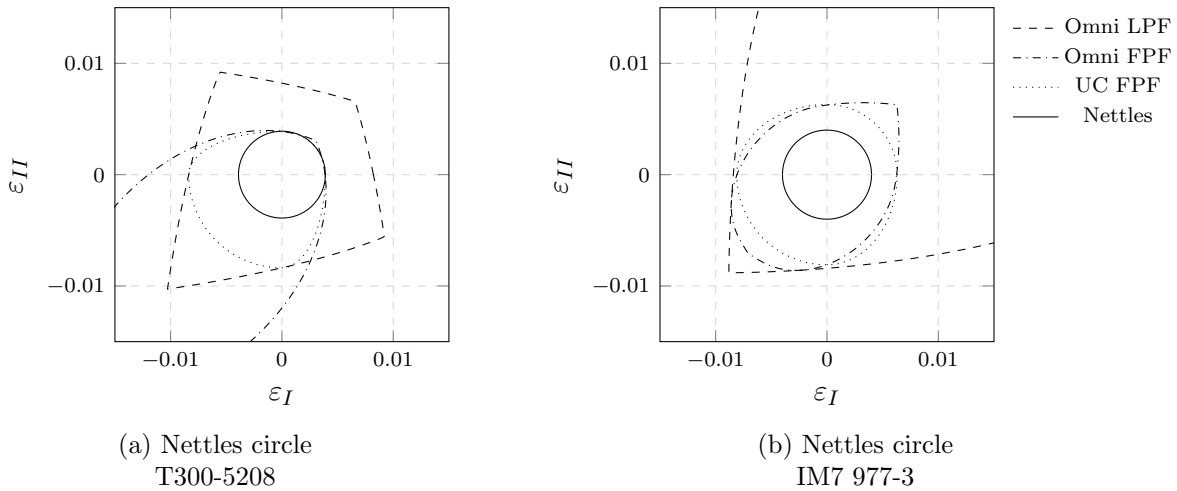


Figure 2.17: Nettles circle for two materials in strain space, including FPF and LPF Omni failure envelopes, and FPF unit circle envelopes.

3 FRP Design Methodologies

In this chapter a new approach to composite design is presented that facilitates the optimization of laminates. In this approach, laminates are described by their stiffness trace and ply orientations are not longer fixed. Quad laminates are replaced by so-called double double laminates with two ply angles $[\pm\Phi, \pm\Psi]$, and homogenization of the laminate eliminates the need for mid-plane symmetry. Thus, ply drop for thickness tapering can be done individually. These principles are applied in optimization procedures described in the second part of this chapter.

3.1 A novel invariant method

In this section, the theoretical aspects of the invariant approach to composite design are presented. It aims to describe the properties of carbon fiber composites with a reduced number of parameter. Applying the failure theories in strain space as described in the previous chapter also simplifies the prediction of failure. In addition, the use of double double laminates facilitates optimization of the laminate design since ply angles are not limited to discrete values.

First, Tsai's modulus is introduced and described in combination with the concept of master ply. Next, normalized stiffness and homogenization of laminates is explained, followed by a comparison of legacy quad and double double laminates. Finally, a method for designing laminates based on these principles is presented.

3.1.1 Tsai's modulus and the master ply concept

Stiffness and compliance of unidirectional layers of CFRP depend on several parameters including matrix and fiber moduli. In chapter 2 a small selection of commonly used materials is given and in table 3.1 it can be seen that for each combination of fiber and matrix material, unique stiffness properties are obtained. To describe the stiffness or compliance of unidirectional plies, at least four parameters (E_1, E_2, ν_{21}, E_6) are required, which must be determined by tests.

The stiffness and compliance matrices of UD layers are tensors and therefore there are invariants associated with them. For example, the trace of the stiffness tensor is a material dependent value that remains the same in any orientation and can therefore be treated as a material constant that is unique to each CFRP material. Using engineering constants and assuming a plane stress state, the trace of stiffness matrices is calculated by:

$$tr(\mathbf{Q}) = Q_{11} + Q_{22} + 2Q_{66} \quad (3.1)$$

In (Tsai and José Daniel D. Melo 2015, pp. 281–282) it is shown that CFRP materials share common stiffness properties if they are normalized by their respective trace $tr(\mathbf{Q})$. Especially in the fiber direction, the trace normalized stiffness parameters of various materials are very close to each other. Table 3.1 shows the material parameters and trace normalized stiffness components (plane stress) of 15 CFRP materials. Comparing the moduli E_1 and the trace normalized moduli E_1^* among all materials, the high standard deviation and variation almost vanished for the normalized values.

The last row of table 3.1 shows the so-called master ply values of the respective material parameter, which are obtained by the arithmetic mean of the trace normalized stiffness parameters. E_2^* and E_6^* are derived analogously by their means and are shown in table 3.2, where all master ply material parameters are given. These master ply values apply to all CFRP materials, as explained below.

Table 3.1: Material parameters and trace normalized plane stress stiffness components of various CFRP, adapted from (Tsai and José Daniel D. Melo 2015, p. 281).

Material	E_1 [GPa]	E_2 [GPa]	ν_{21}	E_6 [GPa]	Q_{11}^*	Q_{22}^*	Q_{12}^*	Q_{66}^*	$tr(\mathbf{Q})$ [GPa]	E_1^*
IM6/epoxy	203	11.2	0.32	8.40	0.8791	0.0485	0.0155	0.0362	232	0.874
IM7/977-3	191	9.94	0.35	7.79	0.8825	0.0459	0.0161	0.0358	218	0.877
T300/5208	181	10.30	0.28	7.17	0.8805	0.0501	0.0140	0.0347	206	0.877
IM7/MTM45	175	8.20	0.33	5.50	0.9014	0.0422	0.0139	0.0282	195	0.897
T800/Cytec	162	9.00	0.40	5.00	0.8955	0.0497	0.0199	0.0274	183	0.888
IM7/8552	159	8.96	0.32	5.50	0.8888	0.0501	0.0160	0.0306	180	0.884
T800S/3900	151	8.20	0.33	4.00	0.9034	0.0491	0.0162	0.0238	168	0.898
T300/F934	148	9.65	0.30	4.55	0.8878	0.0579	0.0174	0.0271	168	0.883
T700 C-Ply 64	141	9.30	0.30	5.80	0.8713	0.0575	0.0172	0.0356	163	0.866
AS4/H3501	138	8.96	0.30	7.10	0.8567	0.0556	0.0167	0.0438	162	0.852
T650/epoxy	139	9.40	0.32	5.50	0.8724	0.0590	0.0189	0.0343	160	0.866
T4708/MR60H	142	7.72	0.34	3.80	0.9029	0.0491	0.0167	0.0240	158	0.897
T700/2510	126	8.40	0.31	4.20	0.8827	0.0588	0.0182	0.0292	144	0.877
AS4/MTM45	127	7.93	0.30	3.60	0.8938	0.0558	0.0167	0.0252	143	0.889
T700 C-Ply 55	121	8.00	0.30	4.70	0.8746	0.0578	0.0173	0.0338	139	0.869
Std dev	24.6	1.0	0.029	1.5	0.0132	0.0053	0.0016	0.0056		0.013
Coeff var %	16.0	10.9	9.0	27.2	1.5	10.1	9.6	17.9		1.5
Master ply			0.32		0.8849	0.0525	0.0167	0.0313	1	0.880

Table 3.2: Master ply material parameter.

E_1^*	E_2^*	E_6^*	ν_{21}	Q_{11}^*	Q_{22}^*	Q_{12}^*	Q_{66}^*	$tr(\mathbf{Q}^*)$
0.880	0.052	0.031	0.32	0.8849	0.0525	0.0167	0.0313	1

As already mentioned, normalized stiffness components in fiber direction are very close to each other whereas matrix-dominated stiffnesses show larger dispersion. A close estimation for trace for all CFRP materials can be obtained by:

$$tr(\mathbf{Q}) \approx \frac{E_1}{0.88} \quad (3.2)$$

which can be verified using table 3.1. Considering that Q_{11}^* accounts for about 88.5% of the trace, the larger scatter of matrix-dominated stiffnesses is not problematic since they are only responsible for the remaining 11.5%. Furthermore, testing for E_2 and E_6 is no longer required, since they can be derived by trace and the respective master ply parameter E_2^* or E_6^* . The errors generated by this assumption were evaluated in (Tsai, José Daniel D. Melo, et al. 2017, pp. 8–9), where it is shown that the average relative error for trace is 1.76% and the errors by assuming master ply values for E_2 and E_6 are below 1%. In honor of Prof. Tsai for these findings, the trace of CFRP materials is named Tsai’s modulus (Arteiro et al. 2020, p. 3).

The use of master ply in combination with the classical laminate theory enables the generation

of trace-normalized laminate factors for stiffness components of multidirectional laminates. The trace normalized in-plane laminate stiffness \mathbf{A}^* can be derived by summation of the respective transformed trace normalized ply stiffnesses $\mathbf{Q}_{xy,i}^*$, normalized by the number of plies n .

$$\mathbf{A}^* = \frac{1}{n} \sum_{i=1}^n \mathbf{Q}_{xy,i}^* \quad (3.3)$$

Laminate factors E_x^*, E_y^*, E_s^* , i.e. trace normalized engineering constants, are derived by:

$$E_i^* = \frac{E_i}{tr(\mathbf{A}^*)} \quad i = x, y, s \quad (3.4)$$

Since $tr(\mathbf{A}^*) = tr(\mathbf{Q}^*)$, the value of trace can be determined by testing a laminate in its longitudinal direction for its Young's modulus and dividing it by the corresponding trace normalized laminate factor (Arteiro et al. 2020, p. 6):

$$tr(\mathbf{Q}^*) = tr(\mathbf{A}^*) = \frac{E_x}{E_x^*} \quad (3.5)$$

A major advantage of this method is that process-related defects in the material are already taken into account when determining the stiffness parameters, and these thus correspond to those of the finished laminate (Tsai and José Daniel D. Melo 2015, p. 285).

3.1.2 Normalized stiffness of laminates and homogenization

The components of the ABD matrix are calculated according to the classical laminate theory and using non-normalized material parameters have different units for \mathbf{A} , \mathbf{B} , and \mathbf{D} . Therefore, the sub matrices can not be compared directly. By choosing suitable normalization factors, i.e. thickness normalization, their units can be adjusted to each other as shown in table 3.3. Note that thickness normalized stiffnesses are designated by $()^n$ and trace normalized values by $()^*$.

Table 3.3: Load-strain relationship in absolute and normalized form.

absolute	thickness normalized
$\begin{bmatrix} \mathbf{N} \\ \mathbf{M} \end{bmatrix} = \begin{bmatrix} \mathbf{A} & \mathbf{B} \\ \mathbf{B} & \mathbf{D} \end{bmatrix} \begin{bmatrix} \boldsymbol{\varepsilon}^o \\ \boldsymbol{\kappa} \end{bmatrix}$	$\begin{bmatrix} \boldsymbol{\sigma}^o \\ \boldsymbol{\sigma}^f \end{bmatrix} = \begin{bmatrix} \mathbf{A}^n & \mathbf{B}^n \\ 3\mathbf{B}^n & \mathbf{D}^n \end{bmatrix} \begin{bmatrix} \boldsymbol{\varepsilon}^o \\ \boldsymbol{\varepsilon}^f \end{bmatrix}$
$A_{ij} [N/m]$	$A_{ij}^n [N/m^2]$
$B_{ij} [N]$	$B_{ij}^n [N/m^2]$
$D_{ij} [Nm]$	$D_{ij}^n [N/m^2]$

Thickness normalized stiffnesses are calculated as shown in equation (3.6), where the in-plane stiffness \mathbf{A} is simply divided by the laminate thickness h and the flexural stiffness \mathbf{D} is corrected by a normalized moment of inertia of a rectangular section. The components of the coupling matrix \mathbf{B} are normalized by a more arbitrary factor (Tsai and José Daniel D. Melo 2015, pp. 164–165).

$$\begin{aligned} \mathbf{A}^n &= \frac{1}{h} \mathbf{A} \\ \mathbf{B}^n &= \frac{2}{h^2} \mathbf{B} \\ \mathbf{D}^n &= \frac{12}{h^3} \mathbf{D} \end{aligned} \quad (3.6)$$

Using these factors for normalization, all sub matrices of \mathbf{ABD}^n have the same units, and in addition, the traces of the normalized in-plane and flexural stiffnesses are equal. They are also equal to the trace of the ply stiffness \mathbf{Q} :

$$\text{tr}(\mathbf{A}^n) = \text{tr}(\mathbf{D}^n) = \text{tr}(\mathbf{Q}) \quad (3.7)$$

The components of \mathbf{A}^n are independent of the stacking sequence, but those of \mathbf{D}^n are not, so their values are not necessarily equal. But as the number of stacked sub-laminates increases, their components converge to the same values. Moreover, the order of magnitude of \mathbf{B}^n decreases sharply compared to those of \mathbf{A}^n and \mathbf{D}^n . This characteristic is called homogenization and is an effective way to achieve out-of-plane homogeneity.

$$A_{ij}^n \approx D_{ij}^n \gg B_{ij}^n \quad (3.8)$$

With homogenization, there is no longer a need to design laminates with mid-plane symmetry in order to avoid in-plane-out-of-plane coupling because homogenized laminates are intrinsically symmetric. The absence of mid-plane symmetry allows continuous ply stacking, which is faster and less prone to error when it comes to manufacturing. In addition, with homogenized laminates, ply drops can be done individually, providing more flexibility for design optimization, e.g. thickness tapering (Tsai, José Daniel D. Melo, et al. 2017, p. 46).

The homogeneity of a laminate can be evaluated using the master ply values of \mathbf{ABD}^* , i.e. trace normalized values of equation (3.6), where laminates can be considered homogenized if the following conditions are met (Tsai 2021, pp. 2–4):

$$\left. \begin{array}{l} D_{11}^* - A_{11}^* \\ D_{66}^* - A_{66}^* \\ |D_{16}^*| \\ |D_{26}^*| \\ |B_{ij}^*| \end{array} \right\} \leq 0.02 = 2\% \quad (3.9)$$

The required number of repeats for laminate homogeneity can be determined by evaluating equation (3.9) while increasing the number of repeats. Note that some researcher prefer to normalize B by $1/h^2$ or $4/h^2$, which may yield different number of repeats.

Figure 3.1 shows the required number of repeats for a hard laminate with symmetry a), the same hard laminate without symmetry b) and a double double laminate c). Two repeats corresponding to 40 plies are required if symmetry is considered, three repeats corresponding to 30 plies without symmetry, and 4 repeats equal to 16 plies for double double.

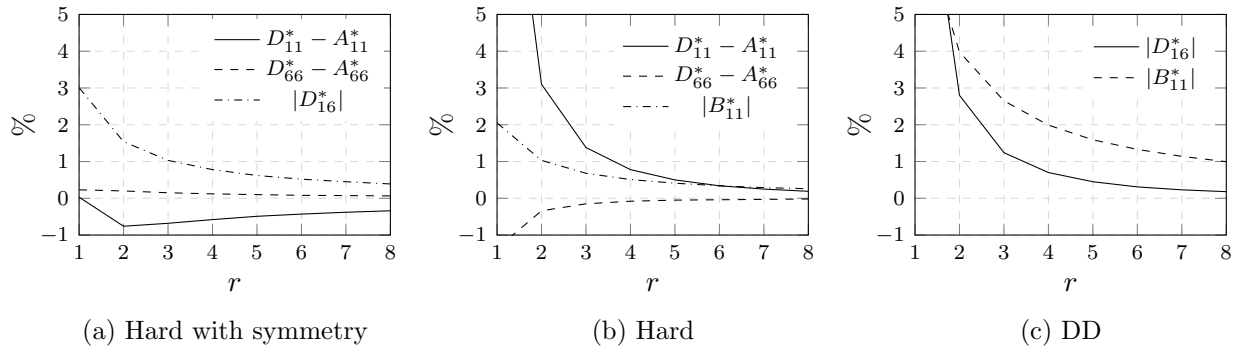


Figure 3.1: Trace normalized stiffness components (%) and required number of repeats r for homogeneity for: a) $[0,45,0,-45,90,45,0,0,-45,0]_{r,S}$, b) $[0,45,0,-45,90,45,0,0,-45,0]_r$ and c) $[18,-62,-18,62]_r$.

In (Tsai 2021, pp. 2–4) it is shown that among all four double double stacking sequences

- staggered 1: $[\Phi, -\Psi, -\Phi, \Psi]$
- staggered 2: $[\Phi, \Psi, -\Phi, -\Psi]$
- staggered 3: $[\Phi, -\Psi, \Psi, -\Phi]$
- staggered 4: $[\Phi, -\Phi, \Psi, -\Psi]$

staggered 1 reaches homogeneity first. Usually, three or four repeats of sub-laminates are required, resulting in a laminate with 12 to 16 plies and a thickness of 0.75mm to 1mm if thin plies of $t = 0.0625\text{mm}$ are used.

Using thin plies, laminates not only homogenize faster, i.e. with lower laminate thickness, but also result in a finer micro structure as shown in figure 3.2. Thus, the toughness and strength of the laminate are higher and interlaminar stresses at free edges are lower, making the laminate less susceptible to delamination (Tsai, José Daniel D. Melo, et al. 2017, p. 46).

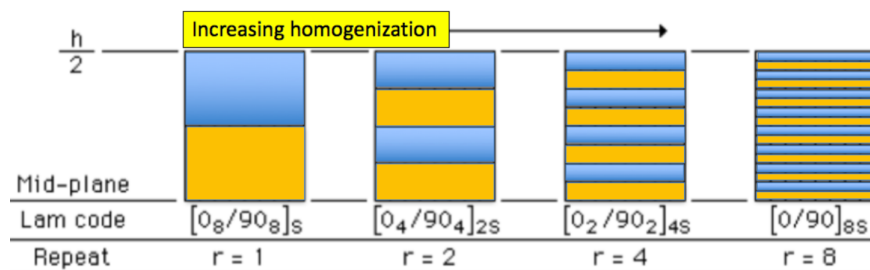


Figure 3.2: Increasing homogenization of a $[0/90]$ laminate with different ply thickness and repeats, adapted from (Tsai, José Daniel D. Melo, et al. 2017, p. 45).

3.1.3 Legacy quad and double-double laminates

In 1960, when the use of fiber reinforced materials started in the aerospace industry, it was common to choose the laminate as $[0_p, \pm 45_q, 90_r]$ which is referred as legacy quad. Depending on the required behavior of the laminate, i.e. directionality or orthotropy, p, q, r is raised until the maximum number of 10 plies in the sub-laminate is reached. The idea was to design not only for primary loads but also for secondary loads which may not be as well understood or defined as the primary. Sub-laminates with more than 10 plies become too difficult to design and manufacture, instead the sub-laminate is stacked until the required thickness is reached.

For quad laminate design, the following rules must be taken into account (Tsai, José Daniel D. Melo, et al. 2017, pp. 115–116):

- Laminates must have mid-plane symmetry
- Each of the four ply orientations has to be at least 10% of the total laminates thickness
- No more than 3 plies of the same orientation should be grouped together, in order to minimize delamination
- Ply drops for thickness tapering must maintain mid-plane symmetry
- Laminates must have a balanced layup, i.e. $n_{-45} = n_{+45}$, to avoid shear-coupling

The application of these rules and the consideration of a discrete ply thickness makes the design of conventional laminates difficult because it is formulated as a discrete optimization problem. Sub-laminates limited to a thickness of 4 to 10 plies reduce the optimization problem, but is still computationally expensive. The permutations of the stacking sequence for different sub-laminate thicknesses are (Tsai, José Daniel D. Melo, et al. 2017, p. 121):

- 4-ply sub-laminate: 24
- 6-ply sub-laminate: 120
- 8-ply sub-laminate: 2520
- 10-ply sub-laminate: 25250

For in-plane laminate design problems, the stacking sequence can often be neglected, only the number of layers in each direction needs to be evaluated (Gürdal, Haftka, and Hajela 1999, p. 187). Among other, genetic algorithm are capable of such integer optimization but usually it is still computationally expensive.

Contrary to the legacy quad, double double laminates, i.e. balanced sub-laminates with four plies and two arbitrary ply angles $[\pm\Phi, \pm\Psi]$, offer much more flexibility. Indeed, they can be perfectly adapted to the loading conditions. In addition, replacing legacy quad laminates with double double laminates is possible with a very good approximation and if the cross-ply ratio equals unity, double double can replace the quad exact, e.g. $[(0, 90)_3, \pm 45]$ can be matched exactly by $[\pm 15, \pm 75]$. Their thickness normalized in-plane stiffnesses A_{11}, A_{22}, A_{66} are identical and both experience the same laminate strain under applied load. If the omni strain failure envelope is applied to these two laminates, their strength and safety factor, i.e. strength ratio, will also be the same (Tsai, José Daniel D. Melo, et al. 2017, p. 113).

Considering homogenization, double double laminates are an enabler for efficient laminate optimization. As mentioned in the previous section, DD laminates homogenize with three to four stacking repeats corresponding to 0.75mm and 1mm respectively. With homogenized laminates, mid-plane symmetry is no longer required and thickness tapering can be performed one-by-one. In addition, the laminates become tougher, their strength will be higher and inter laminar stresses are reduced compared to traditional laminate designs (Tsai, José Daniel D. Melo, et al. 2017, p. 46).

3.1.4 Trace-based sizing method

In (Tsai, José Daniel D. Melo, et al. 2017, pp. 259–268) and (Tsai, Arteiro, and Jose D. D. Melo 2016, pp. 590–593), a trace-based laminate sizing method is proposed that is suitable for any laminate. The method can be used for legacy quad laminates as well as for double double laminates to determine the best thickness and material.

Starting from a predefined design and any baseline material, universal laminate factors are determined by Tsai’s modulus for the selected material. Since the material can be changed later, the baseline material does not have to be the final one. Solving the laminates boundary-value problem for one or multiple loads yields the strain field ε_i ($i = x, y, s$) which is transformed to principle strain space ε_j ($j = I, II$). The unit circle is applied to determine the strength parameter/ratio $R = 1/k$ for each load case and the global strength distribution is calculated by $\min(R)$ in every point (x, y) of the laminate. In the following step, the thickness is obtained with respect to the strength ratios. Crucially, the unit circle is defined as a one-parameter criterion where the tensile

and compressive failure strains are assumed to be equal ($\varepsilon_X = \varepsilon_{X'} = \min(\varepsilon_X, \varepsilon_{X'})$), so the solution can be easily scaled to any CFRP material based on trace. For example, a material with a failure strain 20% higher than the baseline material will have a strength ratio 20% higher for the same loading scenario. A two-parameter unit circle with actual failure strains in tension and compression, as well as other higher-order failure criteria in strain space, can be used in the final step to further improve the optimal solution. In the works mentioned above, it is suggested to re-run critical load cases with the new material and tapered configuration when stiffness requirements need to be considered, since the elastic response cannot be well predicted by simple scaling between different materials.

Later, it will be shown that an iterative determination of the optimum laminate as implemented in the DD-Design Tool is also required due to the stress redistribution caused by updated ply angles.

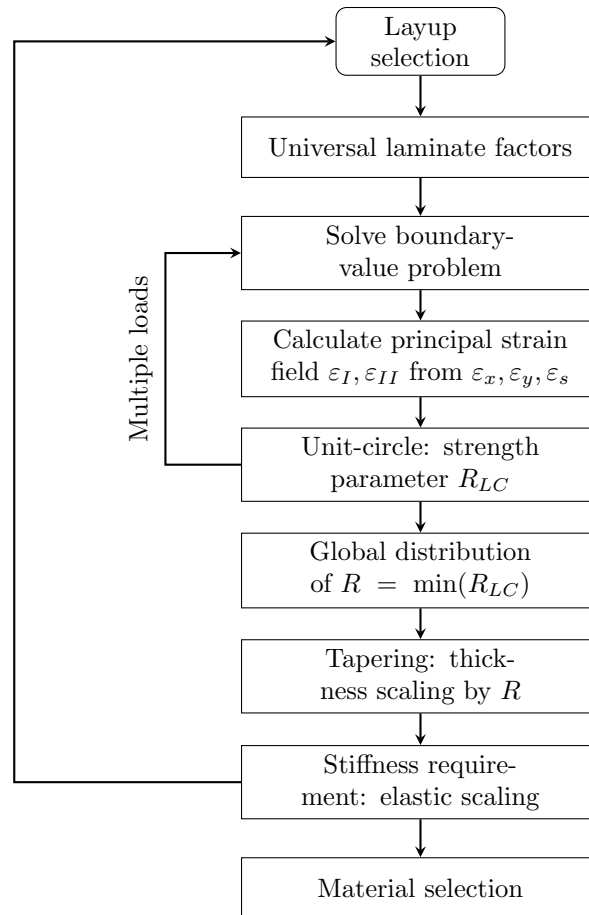


Figure 3.3: Flowchart trace-based sizing method, adapted from (Tsai, Artero, and Jose D. D. Melo 2016, p. 591).

3.2 Optimization frameworks

In this section, the optimization frameworks used are presented. First, the optimization algorithm implemented in the Lamsearch Excel is briefly explained, followed by a description of the DD-Design Tool, since both form the basis for the method used in this work. Finally, the improved DD-Design Tool is explained.

3.2.1 Lamsearch

Lamsearch is an Excel-based optimization tool that applies the invariant methods described earlier to find the best double double laminates and laminate thicknesses. The tool is developed by Stephen W. Tsai, Thierry Massard and Pranav D. Shah and can be obtained by contacting Professor Tsai at Stanford (stsai@stanford.edu).

Four failure criteria are implemented within Lamsearch to find the best laminate with respect to first ply failure:

- Tsai-Wu
- Unit circle
- Nettles circle
- Maximum strain

Lamsearch is able to consider up to 49 loads to find the best laminate among double double or quad families. In the following, the application is described for double double laminates, since the DD-Design Tool and the improved tool are based on the procedure implemented in the Excel file.

Based on the selected failure criterion, strength ratio fields $R(\Phi, \Psi)$ are calculated for each load case as a function of Φ and Ψ by transforming the input stress to strain and evaluating the failure criterion. The strength ratio fields are represented by 2 dimensional matrices with discrete values for Φ and Ψ between 0° and 90° as shown in figure 3.4.

[$\pm\Phi$]	0.0	7.5	15.0	22.5	30.0	37.5	45.0	52.5	60.0	67.5	75.0	82.5	90.0
0.0	56	62	81	107	139	174	199	200	176	137	97	70	62
7.5	62	69	87	111	142	177	203	207	186	147	108	81	70
15.0	81	87	102	119	147	191	223	230	210	174	136	108	97
22.5	107	111	119	130	152	198	242	252	239	209	174	148	137
30.0	139	142	147	152	167	198	222	243	247	231	205	181	174
37.5	174	177	191	198	198	186	189	210	226	226	213	196	191
45.0	199	203	223	242	222	189	170	171	185	195	194	185	181
52.5	200	207	230	252	243	210	171	151	150	156	159	156	154
60.0	176	186	210	239	247	226	185	150	133	129	128	125	123
67.5	137	147	174	209	231	226	195	156	129	115	105	98	96
75.0	97	108	136	174	205	213	194	159	128	105	90	80	76
82.5	70	81	108	148	181	196	185	156	125	98	80	66	60
90.0	62	70	97	137	174	188	176	148	119	96	76	60	54

Figure 3.4: Double double laminate strength ratio field determined by the Lamsearch Excel tool.

The combination of Φ and Ψ yielding the highest value for strength ratio R defines the best double double laminate for the respective load case.

To evaluate the best laminate considering all load cases, a new strength ratio field is determined by the minimum strength of all load cases for each combination of Φ and Ψ . This procedure is shown schematically in figure 3.5. The best double double angles Φ, Ψ are then determined by the highest strength ratio of this matrix.

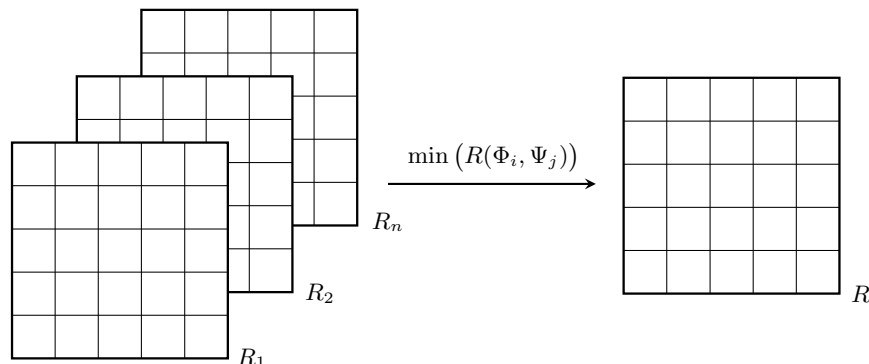


Figure 3.5: Schematic determination of the strength ratio field R for n load cases.

Finally, the laminates thickness is scaled by

$$t_{new} = \frac{t_{old}}{R}$$

with respect to the strength ratio $R(\Phi, \Psi)$ found in the previous step and an initial thickness t_{old} .

3.2.2 DD-Design Tool

The DD-Design Tool (DiCaprio, Riccio, and Tsai 2020) is a fully automated optimization framework to find the best double double laminate and thickness distribution for structural components with respect to strength. Ansys is used to determine the structural response to external loading and the Lamsearch Excel to optimize the laminate design.

The model can be partitioned into up to 49 cells to account for thickness tapering, with each cell subjected to an individual loading condition depending on the applied external forces. Based on an iterative scheme, the tool finds the best laminate design for the structure (Φ, Ψ, t_i) , taking into account the change in cell loading conditions due to variation of fiber directions and laminate thicknesses.

In figure 3.6 the workflow of the DD-Design Tool is shown. Starting from an initial Ansys model with predefined cells and laminate design, a finite element simulation is performed to obtain the loading conditions for each cell. Thickness normalized force resultants are calculated for each cell by averaging the output of all elements belonging to the respective cell. The cell loads and thicknesses are then transferred to the Lamsearch Excel, where the optimal double double angles Φ and Ψ and each cell thickness are determined with respect to the selected failure criterion as described in the previous section. Finally, the convergence criteria are checked. If no convergence is found, the Ansys model is updated and a new iteration is started, or in case of convergence, a digitized model is created where the laminate thicknesses are discretized taking into account the material ply thickness.

The DD-Design Tool assumes the optimization to be converged if the following criteria are fulfilled:

- The change in fiber orientation is zero between two iterations $\Delta\Phi = \Delta\Psi = 0$
- The averaged strength ratio of all cells equals $|R_{avg} - 1| \leq 0.1$ (default value)
- The averaged strength ratio of each cell i has a minimum value of $R_i \geq 0.9$

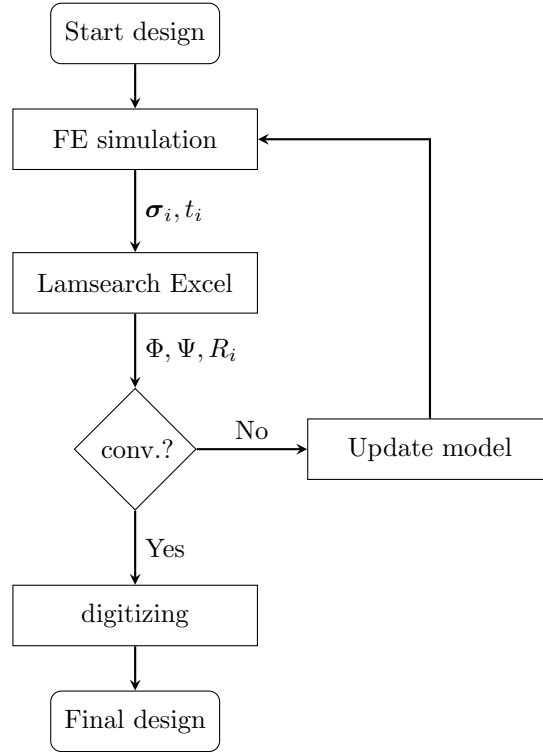


Figure 3.6: Flowchart DD-Design Tool.

3.2.3 Improved DD-Design Tool

The original DD-Design Tool (DiCaprio, Riccio, and Tsai 2020) as described in the previous section was further improved within this thesis. Instead of using Ansys macros and the Lamsearch Excel, the procedure is now completely implemented in Python and any finite element software can be used to determine the structural response. The original version is limited because a maximum of 49 cells and only one loading condition per cell can be considered for optimization. However, usually several load cases have to be taken into account during the design process of components. A further restriction associated with the Lamsearch Excel is that the angle increment for double double angles is fixed at 7.5° (see figure 3.4), which limits the design space of Φ and Ψ .

The improved version is more flexible because any number of cells and load cases can be considered and the angle increment can be selected at any number. The only restriction to the angle increment is that 90 has to be a multiple. In addition, a symmetry option is included that allows the optimization of symmetrical structures such as sandwich constructions, where the layup and thickness must be identical in different areas of the structure. This is important for the model studied in chapter 4, which is a vertical stabilizer of an aircraft designed as a symmetric sandwich construction. Here, the load cases can occur in both directions and would have to be simulated separately. When using the symmetry condition, however, only one direction has to be considered,

since internally the skins are treated as one component that is subjected to the loads from both skins.

The Failure criteria can be selected with respect to first ply failure (TW, UC, NC) or last ply failure (TW, UC), and the convergence criteria have been modified to improve the optimization behavior for structures with low loaded cells.

In general, the optimization procedure of the improved tool is based on the original DD-Design Tool and the Lamsearch Excel, evaluating strength ratios in each cell of the structure to determine Φ, Ψ and the thicknesses t_i . The optimization flowchart is shown in figure 3.7.

Starting from an initial FE model with predefined cells, laminate design and load cases, a finite element simulation is performed to obtain the membrane stress distribution of the laminate for all load cases. The results of the FE software are then averaged load case wise over all elements belonging to a cell to obtain loading conditions that apply to the entire cell for a specific load case. If the symmetry option is enabled, the loads of each symmetry cell are assigned to the respective *main* cell, because they are treated in the optimization procedure as a single cell subjected to the load cases of both. In the next step, Φ and Ψ are determined based on the strength ratios resulting for each cell from the selected failure criterion and the cell loading for each load case. The thicknesses of the cells t_i are then scaled according to the strength ratio resulting from the previously determined angles Φ and Ψ . Subsequently, if no convergence is found, the FE model is updated and the next iteration is started. If the convergence criteria are fulfilled, a digitized model is created, i.e. the laminate thicknesses are discretized taking into account the material ply thickness.

As mentioned, the convergence criteria are modified to improve the optimization behavior for structures where low loaded cells are present. The convergence criterion $|R_{avg} - 1| \leq 0.1$ leads to a high number of iterations or non-convergence for these structures. Low loaded areas yield a high strength ratio, which leads to very low thicknesses in the next iteration according to:

$$t_{new} = \frac{t_{old}}{R}$$

However, in the digitizing step the thicknesses of these cells are discretized to the thickness of a building block and therefore iterations to satisfy the strength criteria in these area are unnecessary. The convergence criteria is modified in a way, that these low loaded cells are not considered for the calculation of R_{avg} .

In appendix A.2, the Python implementation of the improved DD-Design Tool is shown. The improved DD-Design Tool developed in this work is evaluated and verified by comparing optimization results of both tools, the original and the improved one. An example is shown in appendix A.3, where a plate of 49 cells is tested for 2 different load cases and the failure criteria Tsai-Wu, unit circle and Nettles circle. The results shown differ only slightly from each other, if at all.

In addition to the procedure described above, a method for optimizing traditional quad laminates $[0, \pm 45, 90]$ is implemented in the improved tool, where all three failure criteria can be applied. Since the laminate angles are fixed, only the thickness distribution is determined and in the final step, a digitized model is created.

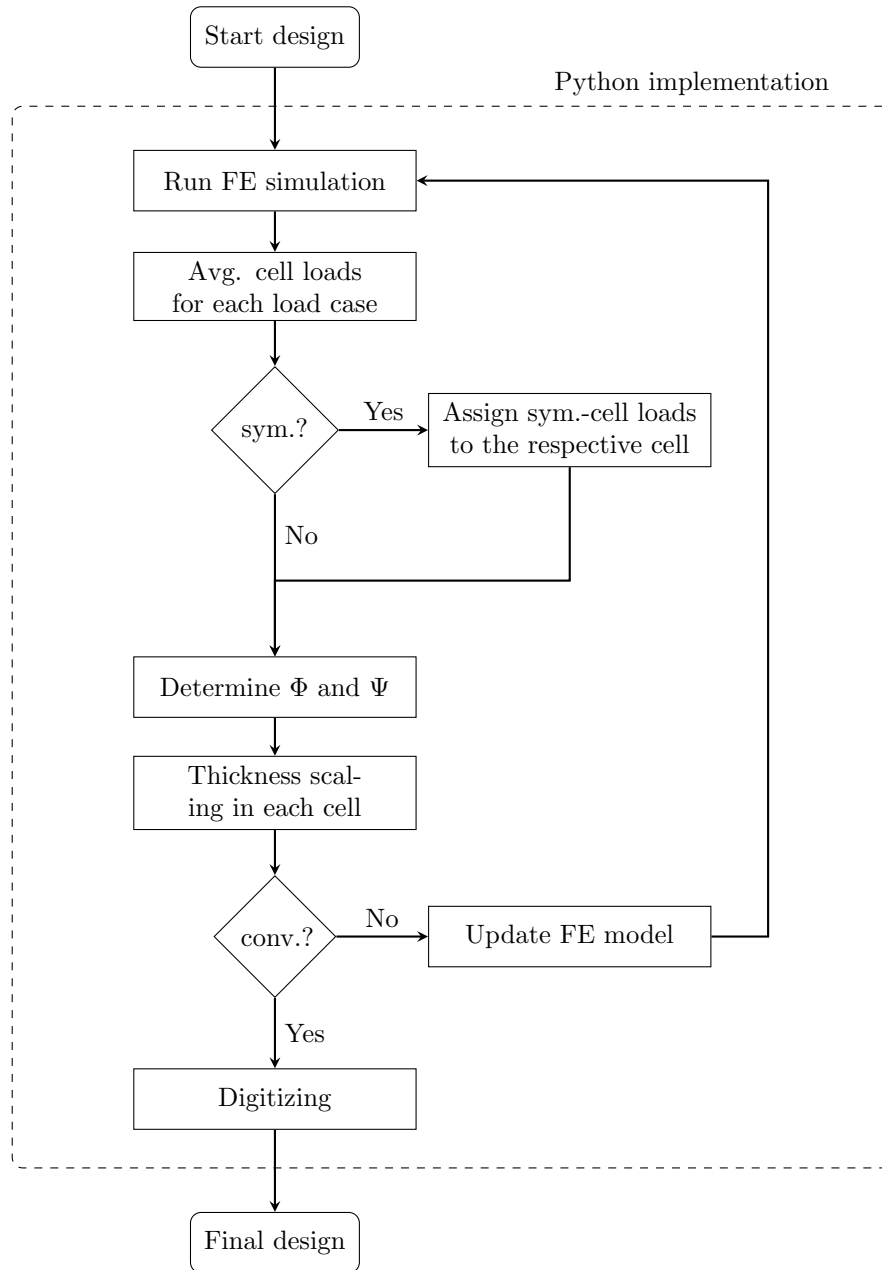


Figure 3.7: Optimization Flowchart of the improved DD-Design Tool.

4 Invariant Based Optimization Of A CFRP Wing Box

In this chapter, the invariant based optimization of a CFRP wing box is covered. The investigated model is a vertical stabilizer of a fighter aircraft and is derived from (Rother 1985). In the work, two design approaches with respect to minimum weight were studied: Quad laminate skins on a honeycomb sandwich core and quad laminate skins on a stringer-only construction. Two load cases, subsonic with skid/slip and supersonic with rudder movement and skid/slip, were considered and it was found that a honeycomb sandwich construction resulted in a significantly lower total mass. In (Neuhäusler 2019, pp. 77–90), the model was investigated again with respect to mass, but the skins were designed as double double laminates. The same material was used as in the original work and the study was carried out considering the design approach of honeycomb sandwich construction, subjecting the structure to the same loads. Optimal double double angles Φ and Ψ were found and a thickness distribution was determined leading to a reduction of skin weight of about 14 % compared to the original work. The results were achieved taking into account not only the strength requirements but also stiffness requirements related to buckling. The outcome of this work was also published in (Neuhäusler and Rother 2021).

In the present work, the model is investigated again with skins made of double double laminates. The optimizations are mainly conducted using the improved DD-Design Tool to determine the best double double angles Φ and Ψ and the resulting thickness distribution. A homogenized design approach as well as a symmetric design approach using double double laminates are studied and compared with respect to weight. In addition, a quad laminate design and an aluminum design are developed to investigate differences in skin weight compared to skins made of double double laminates.

4.1 Model description

The simulation model of the wing structure used in this work was adapted from the CAD model of (Neuhäusler 2019), who reconstructed the original model from a technical drawing in (Rother 1985). Similar to (Neuhäusler 2019), the finite element model of the wing structure is modeled using Abaqus/CAE and solved using Abaqus/Standard. In figure 4.1 the model is shown.

The structure consists of two spars, an upper skin and a lower skin with a honeycomb core in between, a tip shell with honeycomb core and a rudder shell with honeycomb core and is symmetric about the xy -plane. The spars, the upper and the lower skin are connected to the honeycomb core by tie constraints which allows no relative displacement between the parts. Likewise, the shell and the core of the tip, as well as the shell and the core of the rudder are connected to each other by means of tie-constraint. The rudder and the main structure are connected by a coupling constraint of the type continuum distributing, to transfer the load between both parts while allowing relative displacement. The connection of tip and main structure again is modeled using tie constraints.

Boundary conditions are applied at $x = 0$ at the main core, where all translational degrees of freedom are constrained. The edges of the spars and the upper and lower skin are also constrained in $x = 0$, but in addition to the translational dofs, the rotational dofs are also set to 0. Furthermore, the movement of the rudder in the y direction is partially constrained.

The model is meshed as shown in figure 4.1 b) applying a global seed size of 40mm and local refinement in few areas. Full integrated linear hexahedron elements (C3D8) are used for all solid parts and full integrated linear quadrilateral shell elements (S4) for all surface parts.

The loads are the same as in (Neuhäusler 2019) where they are applied as concentrated forces in discrete points, since the original finite element model from 1985 was much coarser due to lower computational capabilities. The load introduction points are shown on figure 4.1 a) as black points.

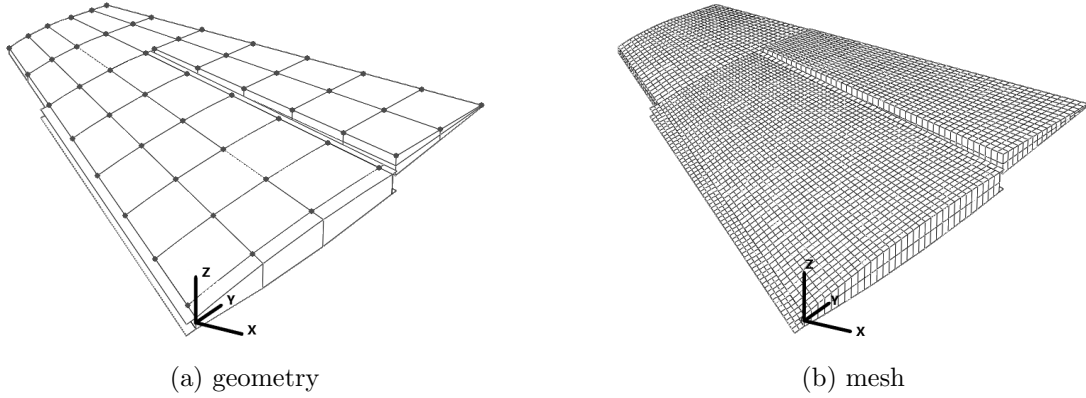


Figure 4.1: Wing model geometry with highlighted load introduction points and finite element mesh.

The materials used in the model are aluminum (tip and rudder shells, spars, *skins*), ACA CFRP (skins) and a HRP honeycomb core. The respective material parameters are given in table 4.1. As in (Neuhäusler 2019) and (Rother 1985), the lower shear modulus is used in L and W direction for the HRP honeycomb material. The Poisson's ratio of HRP material is an arbitrary value, as it is not given in (Rother 1985). However, since for sandwich constructions the global ratio of the panel is mainly dependent on the laminate Poisson's ratios, this assumption is valid (Zenkert 1997, p. 31).

Table 4.1: Material parameters of aluminum, HRP 4.8 honeycomb and unidirectional ACA layer, taken from (Rother 1985, p. 14).

Material	Elastic moduli [MPa]	Strength [MPa]	Density [kg/mm ³]	Poisson's ratio
Aluminum	$E = 68900$ $E_s = 26500$	$X = 206$ $S = 118.9$	$\rho = 2.7 \cdot 10^{-6}$	$\nu_{21} = 0.3$
HRP	$E_3 = 311.5$ $E_s = 34.5$	$Z = 2.98$ $S = 0.76$	$\rho = 6.4 \cdot 10^{-8}$	$\nu_{21} = 0.49$
ACA	$E_1 = 140000$ $E_2 = 6000$ $E_6 = 1300$	$X = 1300$ $X' = 1000$ $Y = 25$ $Y' = 100$ $S = 40$	$\rho = 1.55 \cdot 10^{-6}$	$\nu_{21} = 0.3$

Degraded properties of the ACA ply material (carbon fibers in epoxy resin) are calculated by equation (2.51). Due to missing data, the matrix modulus is calculated using the rule of mixtures in equations (2.1) and (2.2). A fiber volume fraction of the unidirectional layer of $v_f = 0.6$ is assumed, which is a common value (Schürmann 2007, p. 160), and the epoxy Poisson's ratio is assumed to be $\nu_m = 0.37$ (Schürmann 2007, p. 132). Using the ACA material properties from table 4.1 and the aforementioned v_f and ν_m , yields a matrix modulus $E_m \approx 2500$ [MPa] which is also a common value for epoxy resin according to table 2.3. The matrix shear modulus is obtained as $G_m = 1984$ [MPa]. The degraded material properties in table 4.2 are calculated using these parameters.

Table 4.2: Degraded material parameters for ACA plies.

E_1 [MPa]	\tilde{E}_2 [MPa]	\tilde{E}_6 [MPa]	$\tilde{\nu}_{21}$	\tilde{F}_{xy}^*
140000	1339	790	0.045	-0.075

Eventually, using the material parameters from table 4.1 and 4.2, the failure envelopes are calculated using the respective equations from chapter 2. In figure 4.2 the failure envelopes for the ACA material are shown. Note that the Nettles circle for ACA is defined by a strain cut-off of 4000 microstrain.

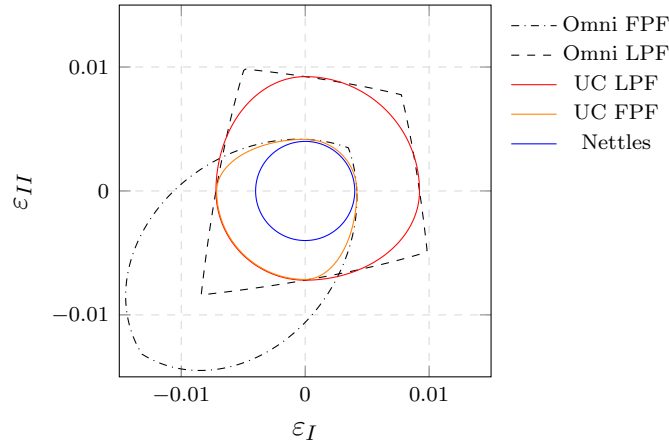


Figure 4.2: Failure envelopes for ACA unidirectional layer.

4.2 Influence of partitioning on the double double laminate of the wing skin

Before optimizing the wing, the influence of partitioning, i.e. discretization of the structure into cells, on the double double laminate of the wing skins is investigated. Note that the mesh density can be much higher and cells are rather element sets of certain areas that are assigned specific thicknesses.

As described in chapter 3, the best double double angles Φ and Ψ are found by evaluating the strength ratios of all cells, which depend on the loading. Since the membrane stress of all elements belonging to a cell is averaged, the resulting strength ratios may be affected as local highly stressed areas within a cell may become invisible. In other words, the optimum double double laminate may depend on the number and size of cells.

A convergence study is carried out to determine the effects of the number of cells on the wing structure. Both load cases are considered in this study and the optimization are run with an angle increment set to 7.5° . The failure criteria used are Tsai-Wu, unit circle and Nettles circle. The number of cells n_c is raised square $n_c = n^2$ in the range $n = [2, 10]$, examples are shown in figure 4.3.

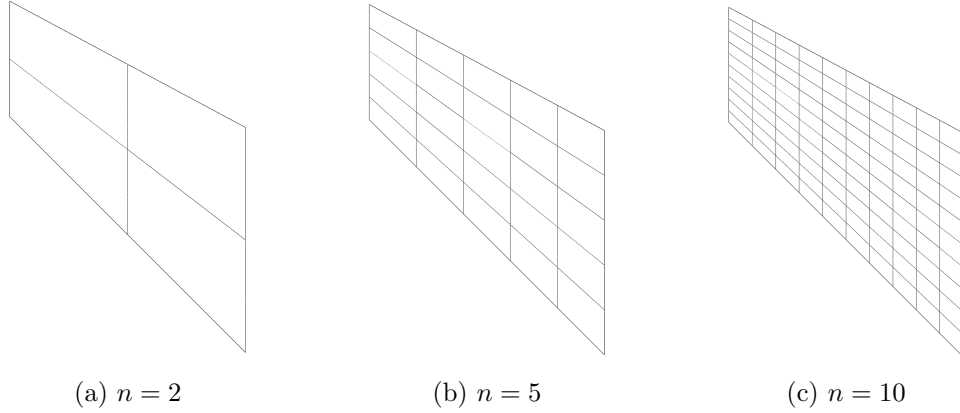


Figure 4.3: Partitioned skins for different number of cells $n_c = n^2$.

The study shows that the optimal double double angles Φ and Ψ for the wing skins are independent of the number of cells n_c , if unit circle or Nettles circle is chosen as failure criterion. For both criteria, the optimal angles result in $\Phi = 22.5^\circ$ and $\Psi = 52.5^\circ$.

For Tsai-Wu, the optimal angles converge to $\Phi = 37.5^\circ$ and $\Psi = 45.0^\circ$. In addition, figure 4.4 a) shows that for $n_c = 3^2$ and $n_c = 4^2$ a different solution is obtained which could be caused by the stress averaging in each cell.

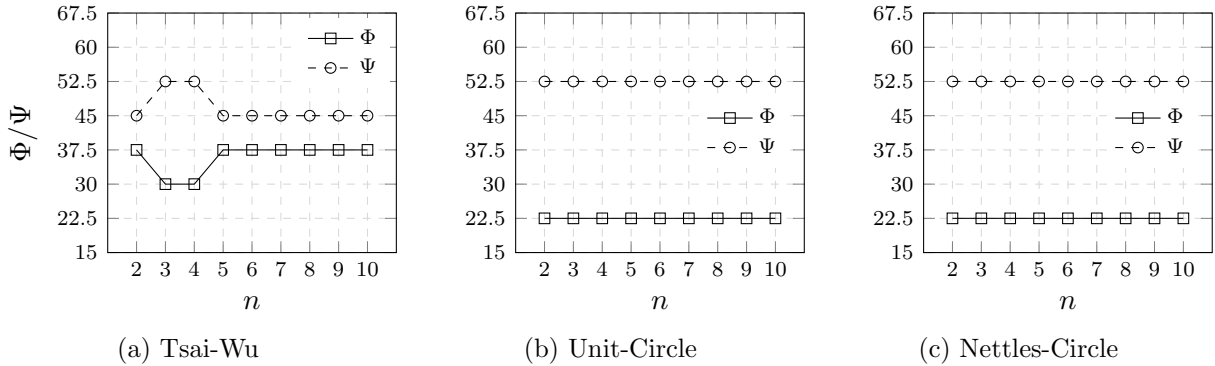


Figure 4.4: Optimal double double angles dependent on the number of cells ($n_c = n^2$) and the respective failure criterion.

In the following sections, all optimization are performed using skin partitioning of $n_c = 100$ to reduce the effect of stress averaging, where highly stressed areas become invisible. This aims in a optimization result that is more similar to the final design, where a ply-by-ply strength analysis must be performed for each element as part of the validation process.

4.3 Skin optimization with Double-Double laminates

This chapter covers the optimization of the wing skins made of double double laminates and the ACA material, using the improved DD-Design Tool as described in chapter 3. The optimization are performed using Tsai-Wu, unit circle and Nettles circle as failure criteria in terms of first and last ply failure. Different angle increments are taken into account for optimization to modify the resolution of the strength ratio field. In figure 4.5 this is shown schematically for angle increments of 7.5° and 2.5° .

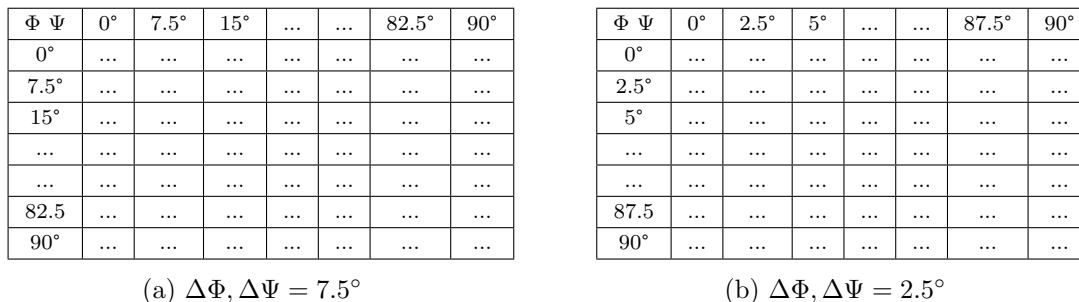


Figure 4.5: Resolution of the strength parameter field $R(\Phi, \Psi)$ based on different angle increments.

The angle increments used for optimization are [1, 1.5, 2, 2.5, 3, 4.5, 5, 6, 7.5, 9, 10] in order to determine the best double double angles Φ and Ψ with respect to the lowest skin weight. Due to the applied load cases, the optimization yields skin thicknesses in certain areas of only one sub-laminate (4 plies). Since homogenization usually requires three to four repeats of sub-laminates, a symmetric design approach using double double laminates and symmetric stacking in each skin is defined and the weight difference with the homogenized design is investigated.

Skin weights are calculated compared for the digitized solution as obtained by the improved DD-Design Tool, the symmetric design approach and the homogenized design approach. In addition, the digitized solutions for first ply failure are compared with results for last ply failure.

Last, the best designs for symmetric and homogenized design approaches for all three failure criteria are used to investigate further weight reduction potential. These designs are used as baseline models for optimization using the response surface method and a genetic algorithm.

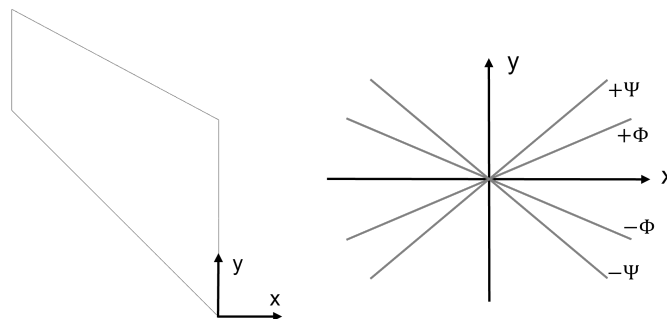


Figure 4.6: Double Double ply orientations for skin optimization.

4.3.1 Determination of the best design using Tsai-Wu

In figure 4.7, the achieved skin weights for the digitized design, the symmetric design and the homogenized design are shown for all considered angle increments. In all cases, the digitized solution offers the lowest weight because design rules are not applied: simply the optimization results are up rounded to the next discrete thickness value. For symmetric designs, the respective digitized design is evaluated and the symmetry design rule is applied. For cells with an odd number of building blocks, the number is rounded up to an even number and mid-plane symmetry is applied. The homogenized design is achieved by evaluating the required number of building block repeats for the specific laminate (Φ, Ψ) . For cells with less building blocks as required for homogeneity, the number is raised.

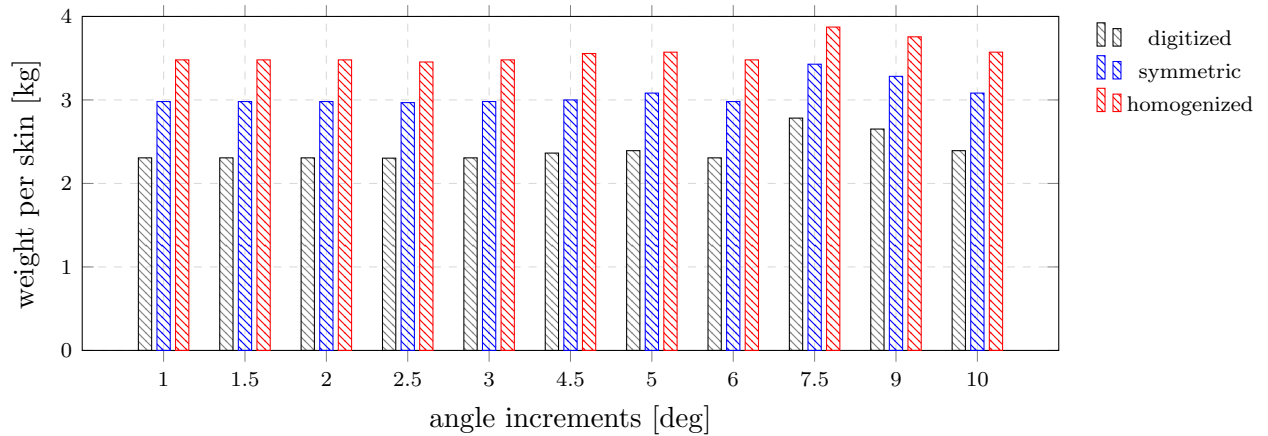


Figure 4.7: Skin weights for different angle increments and design approaches, using the Tsai-Wu failure criterion for FPF.

Figure 4.7 shows that the homogenized design approach yields a higher weight than the symmetric design approach. Digitized thicknesses of only one building block due to only slightly loaded cells are the reason for this observation.

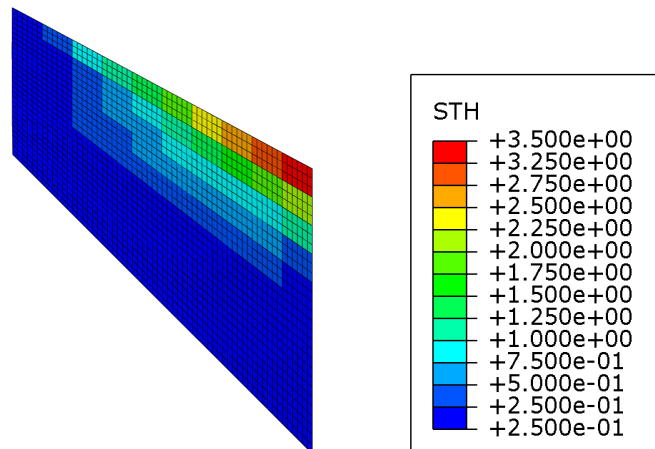


Figure 4.8: Wing skin thickness profile for the Tsai-Wu FPF criterion.

In figure 4.8, the thickness distribution is shown for the digitized design, and the thin cells are

shown in dark blue. For homogeneity, 3 to 4 repeats of building blocks are required, while the symmetry condition can be satisfied with 2 repetitions and thus a lower weight is achieved. The best laminate design, i.e. best double double angles Φ and Ψ , by applying the Tsai-Wu failure criterion is achieved using an angle increment of 2.5° . A skin weight of $m = 2.3029\text{kg}$ with $\Phi = 47.5^\circ$ and $\Psi = 47.5^\circ$ is obtained for the digitized design. The skin weight for the symmetric design is $m_{sym} = 2.9677\text{kg}$ and for the homogenized design $m_{hom} = 3.4544\text{kg}$. Homogeneity of the laminate is achieved with 3 repeats. Figure 4.9 shows the history plot of a) DD-angles and b) the average strength. Within 3 iterations, the optimization procedure yields the best DD-angles $\Phi = \Psi = 47.5^\circ$ and it takes three more iterations until the strength requirement is satisfied.

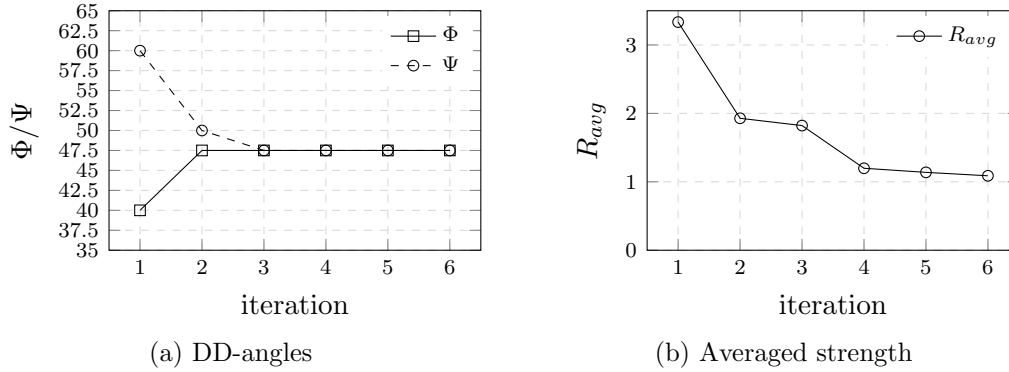


Figure 4.9: Double double angles and averaged strength for all iterations for the best design derived by the Tsai-Wu failure criterion and an angle increment of 2.5° .

The optimal double double angles Φ and Ψ for all angle increments are shown in table 4.3. Except for angle increments of 7.5° and 9.0° , the optimum converged to a single double layup, i.e. $\Phi = \Psi$. Furthermore, angle increments of 1.0° , 1.5° , 2.0° , 3.0° and 6.0° converged to the same layup of $\Phi = \Psi = 48.0$ and therefore their obtained weights are equal. The digitized mass is $m = 2.3064\text{kg}$, the mass for the symmetric design approach is $m_{sym} = 2.9805\text{kg}$ and for homogeneity $m_{hom} = 3.4798\text{kg}$. An angle increment of 4.5° obtained $\Phi = \Psi = 49.5$ and a digitized mass of $m = 2.3635$, resulting in $m_{sym} = 3.0001\text{kg}$ and $m_{hom} = 3.5560\text{kg}$. Angle increments of 5° and 10° converged to $\Phi = \Psi = 50.0^\circ$ with masses of $m = 2.3924\text{kg}$, $m_{sym} = 3.0821\text{kg}$ and $m_{hom} = 3.5722\text{kg}$. An angle increment of 7.5° converged to $\Phi = 37.5^\circ$ and $\Psi = 67.5^\circ$, resulting in a skin weight of $m = 2.7824$ and $m_{sym} = 3.4281\text{kg}$, $m_{hom} = 3.8727\text{kg}$ respectively. A slightly higher mass was obtained by an angle increment of 9.0° which led to $\Phi = 36.0^\circ$ and $\Psi = 63.0^\circ$. A digitized mass of $m = 2.6514\text{kg}$ is achieved which yields, $m_{sym} = 3.2827\text{kg}$ and $m_{hom} = 3.7561\text{kg}$.

All achieved laminates (Φ, Ψ) require 3 repeats until homogeneity, i.e. the condition in equation (3.9), is reached. Furthermore, the optimization converged within 6 or 7 iterations for all angle increments.

Table 4.3: Optimal double double angles Φ , Ψ derived by different angle increments using the Tsai-Wu failure criterion.

angle incr.	1.0°	1.5°	2.0°	2.5°	3.0°	4.5°	5.0°	6.0°	7.5°	9.0°	10.0°
Φ [deg]	48.0	48.0	48.0	47.5	48.0	49.5	50.0	48.0	37.5	36.0	50.0
Ψ [deg]	48.0	48.0	48.0	47.5	48.0	49.5	50.0	48.0	67.5	63.0	50.0

Figure 4.10 shows the digitized skin weight for all angle increments, for first ply failure and last ply failure. Note that for an angle increment of 1°, no convergence was reached for LPF and therefore only FPF is shown.

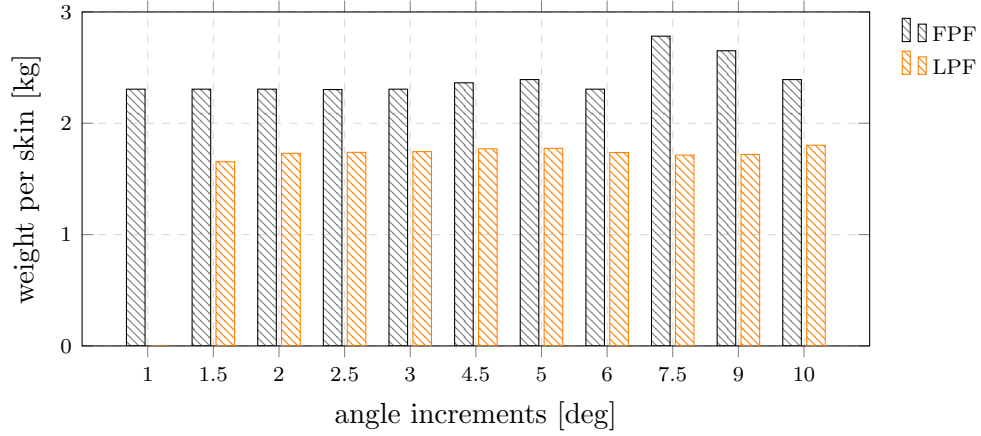


Figure 4.10: Differences in weight for FPF and LPF for Tsai-Wu failure criterion optimizations (no convergence was achieved for 1° LPF).

For last ply failure, the lowest weight is achieved using an angle increment of 1.5°, yielding double angles $\Phi = \Psi = 57.0^\circ$ and a mass of $m = 1.6547\text{kg}$. Figure 4.11 shows the corresponding thickness distribution.

The weight difference between the best design for first ply failure and the best design for last ply failure is $\Delta m = 0,6482\text{kg}$, which is 28% less. Note that the laminate is different for both designs, so the weight difference cannot be considered a safety factor between FPF and LPF.

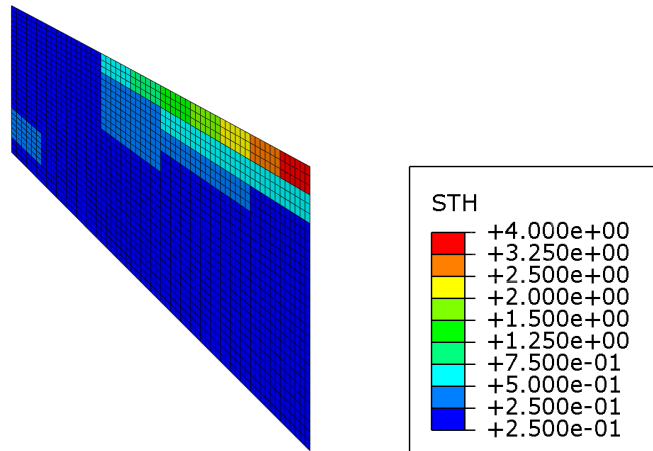


Figure 4.11: Wing skin thickness profile for the Tsai-Wu LPF criterion.

4.3.2 Determination of the best design using unit circle

In figure 4.12, the achieved skin weights for the digitized design, the symmetric design and the homogenized design are shown for all considered angle increments. As for the Tsai-Wu failure

criterion, the digitized solution offers the lowest weight in all cases because design rules are not applied: simply the optimization results are up rounded to the next discrete thickness value. For symmetric designs, the respective digitized design is evaluated and the symmetry design rule is applied. For cells with an odd number of building blocks, the number is rounded up to an even number and mid-plane symmetry is applied. The homogenized design is achieved by evaluating the required number of building block repeats for the specific laminate (Φ, Ψ) . For cells with less building blocks as required, the number is raised.

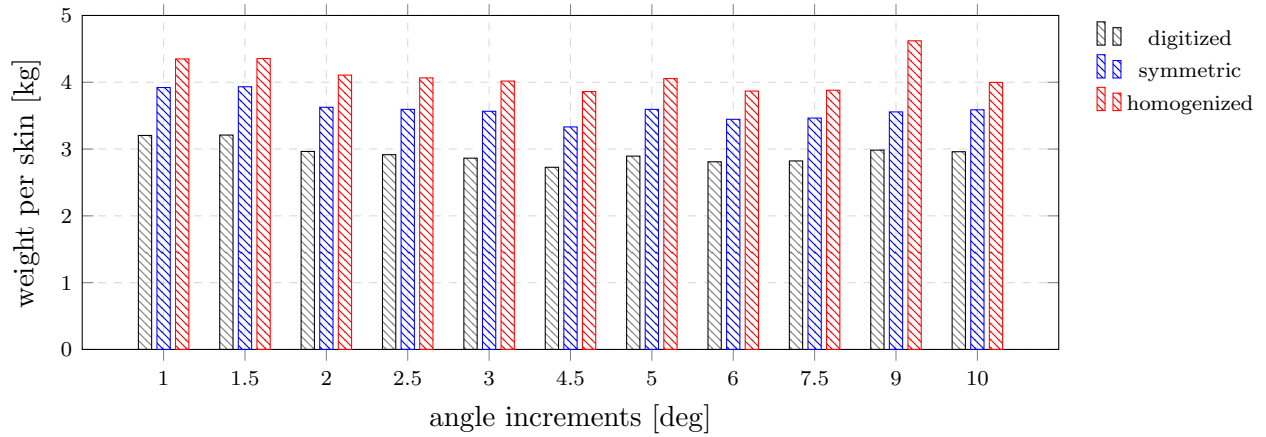


Figure 4.12: Skin weights for different angle increments and design approaches, using the unit circle failure criterion for FPF.

As shown in figure 4.12, the homogenized design approach yields a higher weight than the symmetric design approach for all angle increments. The reason is that most of the optimized structure is subjected to small loads only, which results in digitized thicknesses equal to only one building block. Figure 4.13 shows the thickness distribution of the wing skin for the digitized design. While homogeneity requires 3 to 4 repeats of building blocks, the symmetry condition can be satisfied with 2 repeats, and therefore a lower weight is achieved.

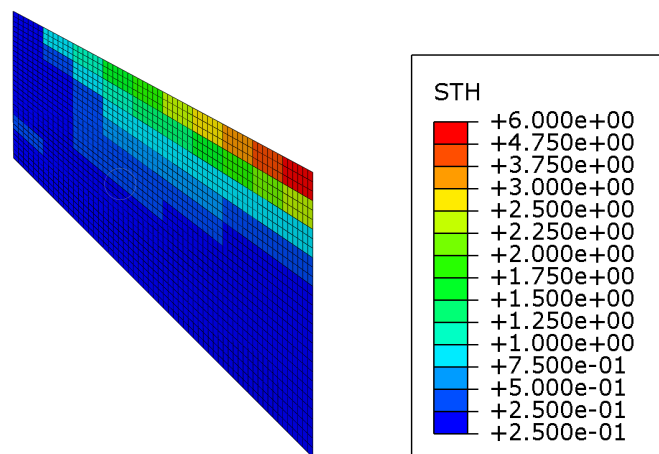


Figure 4.13: Wing skin thickness profile for the unit circle FPF criterion.

By applying the unit circle failure criterion, an angle increment of 4.5° obtained the best laminate. The digitized thickness yields a skin weight of $m = 2.7270\text{kg}$ with $\Phi = 40.5^\circ$ and $\Psi = 63.0^\circ$. The skin weight for the symmetric design is $m_{sym} = 3.3313\text{kg}$ and for the homogenized design $m_{hom} = 3.8611\text{kg}$. Homogeneity of this laminate is achieved with 3 repeats. Figure 4.14 shows the history plot of a) DD-angles and b) the average strength R_{avg} . Within 2 iterations, the optimization procedure yields the best DD-angles $\Phi = 40.5^\circ$ and $\Psi = 63.0^\circ$ and it takes a total of 7 iterations until the strength requirement is satisfied.

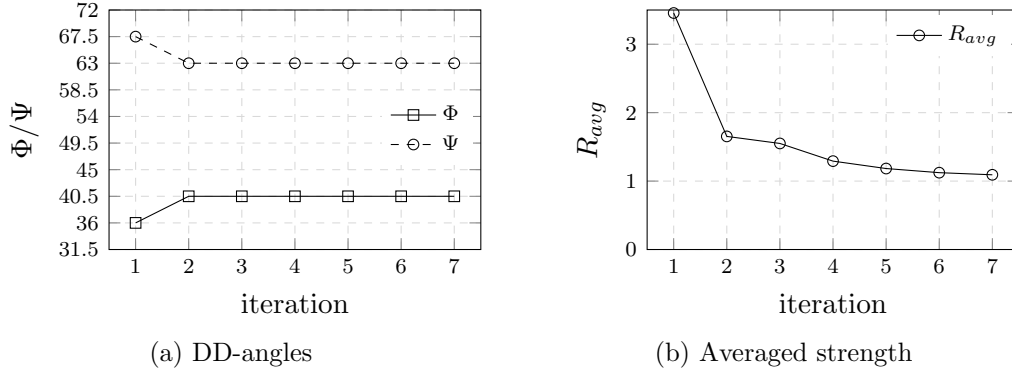


Figure 4.14: Double double angles and averaged strength for all iterations for the best design derived by the unit circle failure criterion and an angle increment of 4.5° .

The optimal double double angles Φ and Ψ for all angle increments are shown in table 4.4. Unlike for Tsai-Wu failure criterion, the optimization for all applied angle increments converged to double double laminates with $\Phi \neq \Psi$.

Angle increments of 1.0° and 1.5° give the highest skin weights for the digitized solution, with a mass of $m = 3.2038\text{kg}$ and $m = 3.2096\text{kg}$, respectively. Their laminate angles are almost identical with $\Phi = 49.0^\circ$ and $\Psi = 64.0^\circ$ for the 1.0° increment and $\Phi = 49.5^\circ$ and $\Psi = 63.0^\circ$ for 1.5° . The symmetric design approach results in weights of $m_{sym} = 3.9211\text{kg}$ and $m_{sym} = 3.9326\text{kg}$ and for the homogenized approach in $m_{hom} = 4.3494\text{kg}$ and $m_{hom} = 4.3552\text{kg}$.

With $m_{hom} = 4.6205\text{kg}$, the highest weight for the homogenized design approach is obtained by an angle increment of 9.0° . The optimization yields double double angles of $\Phi = 36^\circ$ and $\Psi = 72^\circ$, for which a stack repeat of 4 building blocks is required to achieve homogeneity. Even though the mass for the digitized design is not the highest compared to those of the other increment sizes, it can be seen here that the stack repeats can have a large impact on the weight achieved.

For all other angle increments, the resulting weights are between those of 4.5° and 1.5° .

Table 4.4: Optimal double double angles Φ , Ψ derived by different angle increments using the unit circle failure criterion.

angle incr.	1.0°	1.5°	2.0°	2.5°	3.0°	4.5°	5.0°	6.0°	7.5°	9.0°	10.0°
Φ [deg]	49.0	49.5	46.0	45.0	45.0	40.5	45.0	36.0	37.5	36.0	40.0
Ψ [deg]	64.0	63.0	64.0	65.0	63.0	63.0	65.0	66.0	67.5	72.0	70.0

Figure 4.15 shows the digitized skin weights for all angle increment, for first and last ply failure. The lowest weight is obtained by an angle increment of 4.5° for both, first and last ply failure.

For last ply failure, a skin weight of $m = 1.7585\text{kg}$ is achieved with a double double laminate of $[\pm 36.0, \pm 67.5]$. The corresponding thickness distribution is shown in figure 4.16. The optimization yields a difference in weight for FPF and LPF of $\Delta m = 0,9685\text{kg}$ equal to 42%.

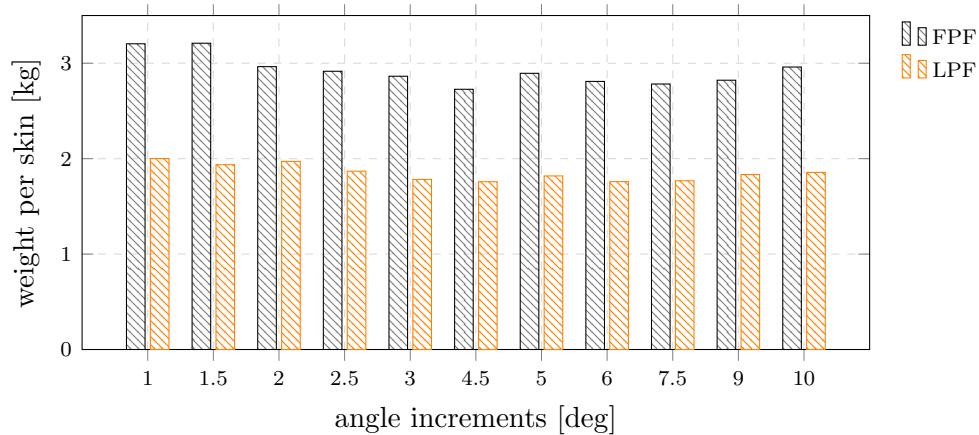


Figure 4.15: Differences in weight for FPF and LPF for unit circle failure criterion optimizations.

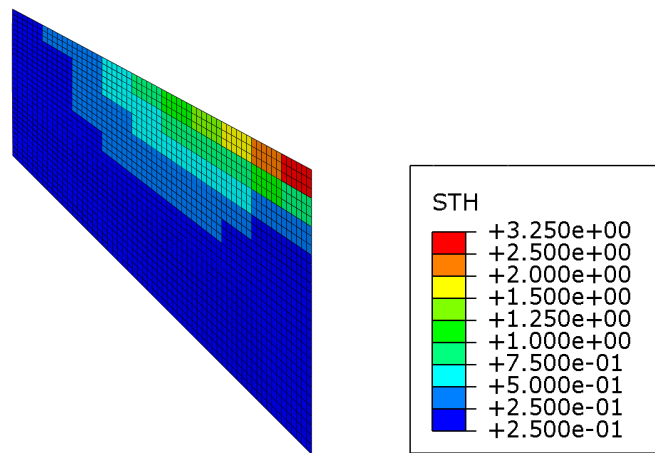


Figure 4.16: Wing skin thickness profile for the unit circle LPF criterion.

4.3.3 Determination of the best design using Nettles circle

In figure 4.17, the achieved skin weights corresponding to the Nettles circle failure criterion for the digitized design, the symmetric design, and the homogenized design are shown for all considered angle increments. As for Tsai-Wu and unit circle, the digitized solution offers the lowest weight for all angle increments because design rules are not applied: the optimization results are up just rounded to the next discrete thickness value. Symmetric designs are created by evaluation of the digitized design and applying the rules for symmetry design. For cells with an odd number of building blocks, the number is rounded up to an even number and mid-plane symmetry is used. The homogenized design is achieved by evaluating the required number of building block repeats for the specific laminate (Φ, Ψ) . For cells with less building blocks as required, the number is raised.

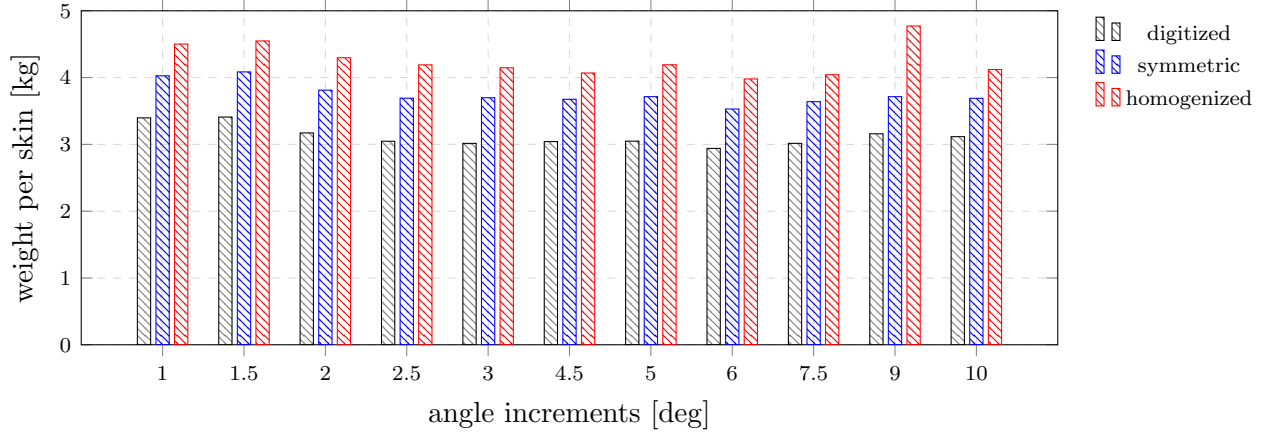


Figure 4.17: Skin weights for different angle increments and design approaches, using the Nettles circle failure criterion.

The skin weight is higher for the homogenized design approach than for the symmetric design approach because a large part of the skin is lightly stressed and the digitized thickness is only one building block thick as shown in figure 4.18. While homogeneity requires 3 to 4 repeats of building blocks, depending on Φ and Ψ , the symmetry condition can be satisfied with a minimum of 2 repeats.

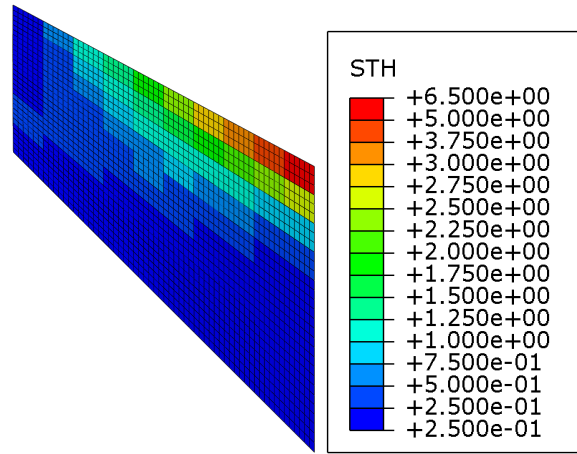


Figure 4.18: Wing skin thickness profile for the Nettles circle criterion.

Using Nettles circle as failure criterion, the best laminate design is achieved as $[\pm 36.0, \pm 66.0]$ by an angle increment of 6.0° . The corresponding weights are $m = 2.9398\text{kg}$ for the digitized design, $m_{sym} = 3.5296\text{kg}$ for the symmetric design, and $m_{hom} = 3.9793\text{kg}$ for the homogenized design, where homogeneity is obtained by 3 repeats of building blocks. Figure 4.19 shows the history plot of a) the DD-angles and b) averaged strength ratio R_{avg} . The best laminate is found already in the first iteration and it takes 7 iterations until the strength requirements are met.

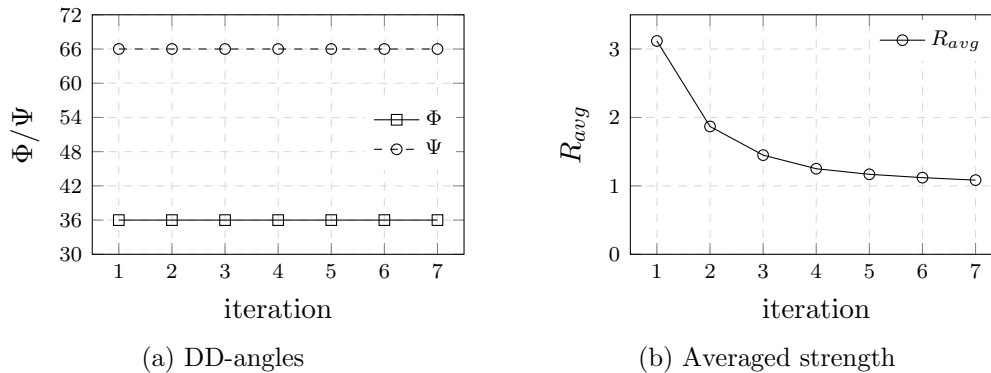


Figure 4.19: Double double angles and averaged strength for all iterations for the best design derived by the Nettles circle failure criterion and an angle increment of 6.0° .

Table 4.5 shows the laminate angles obtained by the Nettles circle failure criterion and all angle increments. Similar to the unit circle criterion, all increments used result in ply orientations with $\Phi \neq \Psi$.

As mentioned, the design corresponding to the lowest weight is achieved by an angle increment of 6.0° yielding a mass of $m = 2.9398\text{kg}$ for the digitized design. This is the only design that accomplishes a weight below 3kg. Close results are obtained by angle increments of $2.5^\circ, 3^\circ, 4.5^\circ, 5^\circ$, and 7.5° where weights between $m = 3.0150\text{kg}$ and $m = 3.0467\text{kg}$ are achieved for the digitized designs. The highest weights for digitized designs are achieved for angle increments of 1.0° and 1.5° with $m = 3.3971\text{kg}$ and $m = 3.4092\text{kg}$, respectively. Taking into account the homogeneity design approach, the heaviest design is obtained by an angle increment of 9° which results in $[\pm 36.0, \pm 72.0]$ laminate and yields a mass of $m_{hom} = 4.7717\text{kg}$. In this case, homogeneity is reached with 4 sub-laminates stacked, while all other designs only require 3.

Table 4.5: Optimal double double angles Φ , Ψ derived by different angle increments using the Nettles circle failure criterion.

angle incr.	1.0°	1.5°	2.0°	2.5°	3.0°	4.5°	5.0°	6.0°	7.5°	9.0°	10.0°
Φ [deg]	49.0	49.5	46.0	45.0	45.0	40.5	45.0	36.0	37.5	36.0	40.0
Ψ [deg]	65.0	64.5	66.0	65.0	63.0	67.5	65.0	66.0	67.5	72.0	70.0

4.3.4 Summary DD optimization using the improved DD-Design Tool

The optimization performed in the previous sections show that the improved DD-Design Tool yield laminate designs and thickness distributions computationally inexpensive. Results are obtained within 6 to 7 iterations for any failure criterion. The best optimization results corresponding to the lowest weight are summarized for all failure criteria in table 4.6.

Table 4.6: Skin weight for different failure criteria and failure modes.

Failure Mode	TW [kg]	UC [kg]	NC [kg]
FPF	2.30	2.73	2.94
LPF	1.65	1.76	-

The lowest weight is achieved by the Tsai-Wu failure criterion for both, first and last ply failure. For first ply failure, a mass off $m = 2.3\text{kg}$ is obtained, and for last ply failure $m = 1.65\text{kg}$, which equals a weight reduction of 28%. A more conservative design is achieved by applying the unit circle as failure criterion. Unit circle yields a weight of $m = 2.73\text{kg}$ for first ply failure and $m = 1.76\text{kg}$ for last ply failure, equal to a weight reduction of 35%. The most conservative criterion considered in this work is the Nettles circle. With Nettles circle, the weight of a skin is obtained as $m = 2.94\text{kg}$. Considering first ply failure, the obtained weight for unit circle is 18% higher than for Tsai-Wu, and the weight achieved by Nettles circle is 28% higher than for Tsai-Wu. Note that the skin weights shown in table 4.6 correspond to the digitized designs. For mid-plane symmetry or homogeneity, the weights are greater. They are shown in table 4.7.

Table 4.7: Skin weight for different failure criteria and design approaches.

Design approach	TW [kg]	UC [kg]	NC [kg]
Digitized (FPF)	2.30	2.73	2.94
Symmetry	2.97	3.33	3.53
Homogenization	3.45	3.86	3.98

The skin weights considering mid-plane symmetry are 29% higher for Tsai-Wu, 22% higher for unit circle, and 20% higher for Nettles circle, compared to the digitized design. Taking into account laminate homogenization, the weight for Tsai-Wu is 50% higher, the weight for unit circle is 41% higher and for Nettles circle 35% higher, compared to the digitized design.

Table 4.8 shows the obtained double double laminate angles and the corresponding angle increment for optimization. It can be seen that each failure criterion yields a different optimum laminate. While Tsai-Wu converged to a single double laminate for the investigated structure, for unit circle and Nettles circle true double double laminates were determined with similar ply angles.

Table 4.8: Optimal double double angles obtained by different failure criteria.

Angles/Incr.	TW [deg]	UC [deg]	NC [deg]
Increment	2.5	4.5	6.0
Φ	47.5	40.5	36.0
Ψ	47.5	66.0	66.0

More important is the observation that the implemented procedure to determine the laminate angles does not yield a better solution for a higher resolution of design space, i.e. smaller angle increment. The laminate designs corresponding to the lowest weight are achieved by an angle increment of 2.5° for Tsai-Wu, 4.5° for unit circle, and 6° for Nettles circle. Smaller increments, e.g. 1.5° for UC and 1.5° or 3° for NC, yield different laminate angles and higher skin weights, even though the same results as in table 4.8 lay in the design space. This is due to the implementation of the iterative laminate angle determination process in the optimization procedure, where they are rather determined by a maximum strength objective than a minimum weight objective.

An alternative approach that considers the structural weight to determine Φ and Ψ is presented in chapter 5 Outlook.

4.3.5 Further optimization potential of best DD designs determined by RSM and GA

Further weight optimization potential of the best double double designs is evaluated in this section. Designs considering mid-plane symmetry and laminate homogenization are optimized using the response surface method (RSM) and a genetic algorithm (GA), respectively. The study is carried out for all three failure criteria (TW, UC, NC) and therefore six optimizations per design approach are executed. A minimum weight objective is chosen and the design space of the double double ply angles is set to

$$\Phi, \Psi \in [0.0, 0.5, 1.0, \dots, 90.0]$$

Starting from the thickness profile obtained by previous optimizations using the improved DD-Design Tool, the ply angles are changed by RSM or GA and a simulation is performed to determine the cell loads. Similar to the procedure in the aforementioned tool, new thickness distributions are determined based on the cell strength ratios, but the ply angles are kept as defined by RSM and GA, respectively.

Table 4.9 shows the optimal double double angles and the resulting total weight per skin for homogenized laminate designs derived by the improved tool, by RSM and by GA optimization. Independent of the failure criterion applied, the total weight is approximately the same for all optimization methods shown. Furthermore, in all cases, the response surface method yields the design with the lowest mass, followed by GA and DD-Tool. Even though the improved DD-Design Tool yields the skin profile with the highest weight, its computational cost is significantly lower compared to RSM and GA. Using Tsai-Wu as failure criterion, RSM required 97 iterations and GA 170 iterations, while the improved DD-Design Tool offers an adequate solution within 6.

Table 4.9: Comparison of optimized designs based on DD-Tool, RSM and GA optimization for homogenized laminate design.

Crit.		DD-Tool	RSM	GA
TW	m [kg]	3.4544	3.35923	3.36325
	Φ [deg]	47.5	46.0	44.0
	Ψ [deg]	47.5	46.0	45.5
	iterations	6	97	170
UC	m [kg]	3.8611	3.67301	3.69377
	Φ [deg]	40.5	36.0	34.0
	Ψ [deg]	63.0	59.0	61.0
	iterations	7	301	160
NC	m [kg]	3.9793	3.78149	3.78149
	Φ [deg]	36.0	38.5	38.5
	Ψ [deg]	66.0	62.0	62.0
	iterations	7	163	120

The optimal double double angles and resulting total weights per skin for symmetric laminate designs are shown in table 4.10. Again, the results obtained by the improved DD-Design Tool are compared with the designs derived by GA and RSM optimization.

Applying Tsai-Wu as failure criterion for optimization the resulting laminate angles are equally

derived as $\Phi = 47.5^\circ$ and $\Psi = 47.5^\circ$ by all three methods. Similar to the symmetric design optimizations, GA required the most iterations with 90, followed by RSM with 85 iterations, and the improved DD-Design Tool with only 6 iterations. Even though the same ply angles are obtained by all three methods, the weight obtained by the improved Tool is not equal to the results of RSM and GA. The weight derived by RSM and GA is $m = 2.96\text{kg}$, which is a difference of less than -1%. This observation is due to the result of the improved tool being taken as the baseline model for GA and RSM, where new thicknesses are evaluated based on the strength ratio and present cell thicknesses.

When using unit circle as failure criterion, the lowest weight is obtained by RSM with a weight saving of 1.8% compared to the baseline model. The response surface method converged after 103 iterations and the genetic algorithm after 180. Again, the DD-Tool required the lowest computational effort with 7 iterations.

Applying Nettles circle as failure criterion, equal double double angles are obtained for all methods used with $\Phi = 36.0$ and $\Psi = 66.0$. Accordingly, the skin weights achieved by RSM and GA are also the same at $m = 3.35\text{kg}$, which is 4.8% less than the design obtained by the DD-Tool. The optimal design was derived by GA after 90 iterations and RSM required 157 iterations, while the DD-Tool converged after 7 iterations.

Table 4.10: Comparison of optimized designs based on DD-Tool, RSM and GA optimization for symmetric laminate design.

Crit.		DD-Tool	RSM	GA
TW	m [kg]	2.9677	2.94583	2.94583
	Φ [deg]	47.5	47.5	47.5
	Ψ [deg]	47.5	47.5	47.5
	iterations	6	85	90
UC	m [kg]	3.3313	3.27349	3.29426
	Φ [deg]	40.5	35.0	34.0
	Ψ [deg]	63.0	58.5	59.5
	iterations	7	103	180
NC	m [kg]	3.5296	3.35433	3.35433
	Φ [deg]	36.0	36.0	36.0
	Ψ [deg]	66.0	66.0	66.0
	iterations	7	157	90

For both design approaches it is shown above, that the improved DD-Design Tool offers computationally inexpensive optimization results. The obtained results are close to those derived by RSM and GA optimizations, with differences in weight below 5%.

4.4 Comparison of Double Double with Legacy Quad and Aluminum designs

In this section, the skin profile is optimized using aluminum and black aluminum, i.e. quasi-isotropic legacy quad laminates made from CFRP.

The optimization of quad laminates is performed using a new method implemented in the improved DD-Design Tool. Similar to the procedure for double double laminates, cell thicknesses are determined by strength ratios with respect to the cell loading conditions. As the laminate angles are fixed, only a thickness scaling is performed and a digitized model is created when convergence is met.

The aluminum design is also obtained by the new quad optimization procedure, but since the material is isotropic the plies behave equally in all directions. Thickness scaling is performed by applying the Tsai-Wu failure criterion because it corresponds to the von-Mises criterion for isotropic materials with equal tensile and compressive strength.

In table 4.11 the achieved skin weights for legacy quad laminates and aluminum construction are compared with the best designs achieved by double double laminates. For legacy quad laminates, three failure criteria are used for optimization: Tsai-Wu, unit circle, and Nettles circle, and as already mentioned, for aluminum only Tsai-Wu is used.

Table 4.11: Comparison of skin weights of legacy quad and aluminum design with digitized double double laminates.

Material	Failure criterion	Quad skin weight	DD skin weight	Δm
ACA	Tsai-Wu	3.62 kg	2.30 kg	-36.5%
ACA	Unit circle	3.73 kg	2.73 kg	-26.8%
ACA	Nettles circle	4.04 kg	2.94 kg	-27.2%
Aluminum	Tsai-Wu	5.92 kg	2.30 kg	-61.1%

It is shown that significant weight savings are possible if double double laminates are considered for the skins. Applying the Tsai-Wu failure criterion, the skin weight can be reduced from 3.62kg to 2.30kg, equal to a reduction of 36.5%. Unit circle yields a weight reduction of 1kg which corresponds to a weight saving of 26.8% and with Nettles circle, the skin weight can be reduced 27%. The highest weight saving is achieved compared to aluminum, where the weight can be reduced 61% from 5.92kg to 2.30kg. Note that for the aluminum design, thickness drops are performed with a step size of 0.25mm, and the quad laminate designs already consist of mid-plane symmetry.

In table 4.12 and table 4.13, similar evaluations are shown but the quad and aluminum designs are compared with symmetry and homogenized double double laminates, respectively.

Considering symmetric double double laminates, there are also significant weight savings. For Tsai-Wu, the weight can be reduced from 3.62kg to 2.97kg, a reduction of 18%. Applying unit circle or Nettles circle as failure criterion, weight reductions of 10.7% and 12.6%, respectively, are possible.

Table 4.12: Comparison of skin weights of legacy quad and aluminum design with symmetric double double laminates.

Material	Failure criterion	Quad skin weight	DD sym. weight	Δm
ACA	Tsai-Wu	3.62 kg	2.97 kg	-18.0%
ACA	Unit circle	3.73 kg	3.33 kg	-10.7%
ACA	Nettles circle	4.04 kg	3.53 kg	-12.6%
Aluminum	Tsai-Wu	5.92 kg	2.97 kg	-49.8%

Higher weights are obtained if the laminate is build with respect to homogeneity. For Tsai-Wu, the weight of the homogenized double double laminate is only 4.7% less than for legacy quads. With unit circle, the achieved weight for homogenized DD laminates is 3.5% higher and Nettles circle yields a weight reduction of only 1.5%. Even though, the weight savings are small if homogenized double double laminates are compared with quad laminates, they yield a weight saving of 41.7% if they are used instead of aluminum profiles.

The reason for the low weight saving potential for homogenized double double laminates is that homogenization requires three to four repeats of sub-laminates stacked. Since there are several low-loaded cells in the wing skin, the thicknesses to meet the strength criterion in these areas are only one building block (four plies). However, this behavior corresponds to the considered model and load cases, other structures may show higher weight savings.

Table 4.13: Comparison of skin weights of legacy quad and aluminum design with homogenized double double laminates.

Material	Failure criterion	Quad skin weight	DD hom. weight	Δm
ACA	Tsai-Wu	3.62 kg	3.45 kg	-4.7%
ACA	Unit circle	3.73 kg	3.86 kg	+3.5%
ACA	Nettles circle	4.04 kg	3.98 kg	-1.5%
Aluminum	Tsai-Wu	5.92 kg	3.45 kg	-41.7%

5 Summary and Conclusion

Within the scope of this thesis, the vertical stabilizer model from (Rother 1985) and (Neuhäusler 2019, S. 77–90) is optimized with a focus on reducing the skin weights by the application of double double laminates $[\pm\Phi, \pm\Psi]$. A new invariant-based method for laminate design is used in which stiffness is described by Tsai’s modulus, homogenization of laminates is considered as an alternative for mid-plane symmetry and failure criteria in strain space are evaluated to obtain the laminate thicknesses.

The method is applied to the FE model by an improved version of the DD-Design Tool (DiCaprio, Riccio, and Tsai 2020), which was developed in the context of this work and allows the optimization of symmetric sandwich structures as required for the wing model. The improved tool is fully implemented in Python and any external finite element software can be used to determine the laminate loads. Furthermore, it applies the same optimization procedure as the original tool but is more flexible because it is designed to consider any number of partitions and any number of load cases. The model is optimized using three different failure criteria to predict first ply failure (Tsai-Wu, unit circle, and Nettles circle), and two criteria for last ply failure (Tsai-Wu and unit circle). For each criterion, the optimization is executed for angle increments of $1^\circ, 1.5^\circ, 2^\circ, 2.5^\circ, 3^\circ, 4.5^\circ, 5^\circ, 6^\circ, 7.5^\circ, 9^\circ, 10^\circ$, which define the resolution of the design space for Φ and Ψ . A total of 55 different optimization configurations were run.

The best result for Tsai-Wu FPF is achieved by an angle increment of 2.5° and for LPF by 1.5° . Applying unit circle as failure criterion, the best design for FPF and LPF is obtained by an increment of 4.5° , and the lowest weight considering Nettles circle was achieved by an angle increment of 6° . The comparisons between FPF and LPF are performed using the digitized optimization results. Among these three criteria, Tsai-Wu yields the lowest weight $m_{digi} = 2.3029\text{kg}$, followed by unit circle $m_{digi} = 2.7270\text{kg}$ and finally Nettles circle with $m_{digi} = 2.9398\text{kg}$. Using last ply failure as optimization criterion, weight savings of 28% for Tsai-Wu and 35% for unit circle compared to FPF. Note that the obtained ply angles differ from those for FPF.

Due to partially low resulting skin thicknesses of only one building block, two design methods are defined and compared concerning skin weight: A homogenized design approach using DD laminates, and a symmetric design approach using DD laminates in combination with mid-plane symmetry in each skin. It is shown that the symmetric approach yields a lower skin weight for all three failure criteria, but this is not generally the case. For the wing model, a greater area of the structure meets the strength criterion already with a thickness of one building block. Consequently, symmetry can be achieved by two repeats of sub-laminate, while homogeneity requires three to four. Thus, for thin-walled DD laminates, the symmetric design approach may yield a better solution.

The best designs for symmetry and homogeneity for all three failure criteria are used as baseline models for optimization using RSM and GA and further optimization potential is investigated. In all cases, the baseline models are close if not equal to the designs derived by RSM and GA. In addition, the model is also optimized considering skins made from legacy quad laminates (quasi-isotropic) and aluminum. Comparing legacy quad with double double laminate design, it is shown for all three failure criteria that double double results in weight savings between 27% and 37%. In Addition, skins made of double double laminates allow a weight saving of 61% compared to skins made of aluminum. However, taking into account design approaches like mid-plane symmetry or homogenization, achieved weight savings are lower.

To sum up, using double double laminates, lower skin weights are achieved for the present model compared to constructions made of legacy quad laminates or aluminum. The improved DD-Design Tool is able to provide an optimized design computationally inexpensive within few iterations, which can be used as baseline model for further improvements. However, the outcome also shows

that the obtained designs depend on the selected angle increment and finer resolution does not necessarily yield a better solution when using the procedure implemented in the DD-Design Tool. Furthermore, if the optimization yields thin-walled structures, a symmetric design approach using DD laminates may yield a better solution compared to homogenization.

Outlook

As mentioned previously, the DD-Design Tool obtained lower skin weights if double double laminates are used instead of legacy quads or aluminum. But it is also shown that a finer resolution of the strength field, i.e. a smaller angle increment, does not necessarily lead to a better solution in terms of weight. For unit circle and Nettles circle, the designs corresponding to the lowest weight were achieved by an angle increment of 4.5° and 6° , respectively. Finer increments instead yield a higher weight. The reason for this behavior is that the laminate angles Φ and Ψ are rather determined by a maximum strength objective than a minimum weight in the Lamsearch algorithm. In other words, the weight reduction is just a consequence of the implemented strength optimization process, where the cell with the highest strength ratio determines Φ and Ψ , and subsequently, the cell thicknesses are scaled concerning these ply angles. Finer angle increments can result in a higher strength ratio in the crucial cell and thus a lower cell thickness. However, depending on the loading conditions in the remaining cells, their thicknesses may be higher, resulting in a higher total weight.

In a further version of the tool, the determination of Φ and Ψ could be implemented concerning the total weight. Instead of evaluating just strength ratio fields $R(\Phi, \Psi)$, a volume field $V(\Phi, \Psi)$ could be determined for each cell, using the respective strength field to obtain a thickness field $t(\Phi, \Psi)$, which is multiplied by the respective cell area. By summing the cell volume fields, a total volume field can then be calculated, as shown in the following equation:

$$V(\Phi, \Psi) = \sum_{k=1}^{n_c} V_k(\Phi, \Psi) = \sum_{k=1}^{n_c} t_k(\Phi, \Psi) A_k = \sum_{k=1}^{n_c} \frac{t_{old,k}}{R_k(\Phi, \Psi)} A_k \quad (5.1)$$

Where Φ and Ψ are determined by the lowest (total) volume. Note that Φ and Ψ are discrete sets that dependent on the angle increment.

Furthermore, new failure criteria such as Puck, Hashin, or Cuntze could be implemented, as well as more finite element software conversions to make the improved DD-Design Tool even more flexible and useful.

The algorithm proposed above should be tested and evaluated for its optimization potential concerning a minimum weight in further study. The wing model can provide a good basis for evaluation since the results of the present work can be used to compare.

References

- Airbus (2021a). “Aviation’s material evolution”. In: *Airbus* (). URL: <https://www.airbus.com/en/newsroom/news/2017-02-aviations-material-evolution> (visited on 04/20/2021).
- Airbus (2021b). “Composites: Airbus continues to shape the future”. In: *Airbus* (). URL: <https://www.airbus.com/newsroom/news/en/2017/08/composites--airbus-continues-to-shape-the-future.html> (visited on 04/20/2021).
- Arteiro, Albertino et al. (2020). “A case for Tsai’s Modulus, an invariant-based approach to stiffness”. In: *Composite Structures* 252.7. ISSN: 02638223. DOI: 10.1016/j.compstruct.2020.112683.
- DiCaprio, Francesco, Aniello Riccio, and Stephen W. Tsai (2020). *DD-Design Tool*.
- Gürdal, Zafer, Raphael T. Haftka, and Prabhat Hajela (1999). *Design and optimization of laminated composite materials*. A Wiley-Interscience Publication. New York, NY: Wiley. ISBN: 0-471-25276-x. URL: <http://www.loc.gov/catdir/bios/wiley042/98022855.html>.
- Hinton, M., P. D. Soden, and Abdul-Salam Kaddour (2004). *Failure Criteria in Fibre-Reinforced-Polymer Composites*. 1. Aufl. s.l.: Elsevier professional. ISBN: 0-08-044475-X. URL: <http://gbv.ebib.com/patron/FullRecord.aspx?p=305568>.
- Jäger, Hubert and Tilo Hauke (2010). *Carbonfasern und ihre Verbundwerkstoffe: Herstellungsprozesse, Anwendungen und Marktentwicklung*. Vol. 326. Die Bibliothek der Technik. München: Verl. Moderne Industrie Süddt. Verl. ISBN: 978-3-86236-001-7.
- Kollar, Laszlo Peter and George S. Springer (2003). *Mechanics of composite structures*. Cambridge and New York: Cambridge University Press. ISBN: 978-0-511-06336-7.
- Lengsfeld, Hauke, Hendrik Mainka, and Volker Altstädt (2020). *Carbon fibers: Production, applications, processing*. 1st. Cincinnati: Hanser Publications. ISBN: 978-1-56990-829-7.
- Mallick, P. K. (2008). *Fiber-reinforced composites: Materials, manufacturing, and design*. 3rd ed., expanded and rev. ed. Boca Raton FL: CRC Press. ISBN: 978-0-8493-4205-9.
- Millen, Scott L.J. and M. Ali Aravand (2021). “Assessing the relative conservatism of the unit circle failure envelope”. In: *Composites Communications* 24.June. ISSN: 24522139. DOI: 10.1016/j.coco.2021.100690.
- MTorres (2021). “Commercial programs”. In: *MTorres*. URL: <https://www.mtorres.es/en/aeronautica/referencias> (visited on 09/05/2021).
- Neuhäusler, Josef (2019). “Design of Composite Structures in the Early Phase”. Master’s thesis. Munich: Munich University of Applied Science.
- Neuhäusler, Josef and Klemens Rother (2021). “Application of Tsai’s Theory for the Laminate Optimization of an Aerospace Wing Box”. In: *Proceedings of the Munich Symposium on Lightweight Design 2020*. Ed. by Simon Pfingstl et al. Berlin, Heidelberg: Springer Berlin Heidelberg, pp. 103–114. ISBN: 978-3-662-63142-3. DOI: 10.1007/978-3-662-63143-0{\textunderscore}11.
- Park, Soo-Jin (2018). *Carbon Fibers*. 2nd ed. 2018. Vol. 210. Springer Series in Materials Science. Singapore: Springer Singapore. ISBN: 978-981-13-0538-2. DOI: 10.1007/978-981-13-0538-2. URL: <http://dx.doi.org/10.1007/978-981-13-0538-2>.
- Reddy, J. N. (2004). *Mechanics of Laminated Composite Plates and Shells Theory and Analysis*. 2nd ed. Boca Raton: Chapman and Hall/CRC. ISBN: 0-8493-1592-1.
- Rother, Klemens (1985). “Bauweisenvergleich eines Seitenleitwerkstoffs aus Kohlefaserverbundwerkstoff für ein Jagdflugzeug: Engl.: Comparison of construction methods of a carbon fiber composite fin box for a fighter plane”. Diploma thesis. München: Fachhochschule München.
- Schürmann, Helmut (2007). *Konstruieren mit Faser-Kunststoff-Verbunden*. 2., bearbeitete und erweiterte Auflage. VDI-Buch. Berlin, Heidelberg: Springer-Verlag Berlin Heidelberg. ISBN: 978-3-540-72189-5. DOI: 10.1007/978-3-540-72190-1.

- Soden, P. (1998). “Lamina properties, lay-up configurations and loading conditions for a range of fibre-reinforced composite laminates”. In: *Composites Science and Technology* 58.7, pp. 1011–1022. ISSN: 02663538. DOI: 10.1016/S0266-3538(98)00078-5.
- Soden, P. D., M. J. Hinton, and A. S. Kaddour (2002). “Biaxial test results for strength and deformation of a range of E-glass and carbon fibre reinforced composite laminates: failure exercise benchmark data”. In: *Composites Science and Technology* 62.12-13, pp. 1489–1514. ISSN: 02663538. DOI: 10.1016/S0266-3538(02)00093-3.
- Tsai, Stephen W. (2008). *Theory of composites design*. Dayton: Think Composites. ISBN: 978-0-9618090-3-4.
- Tsai, Stephen W. (2021). “Double-Double: New Family of Composite Laminates”. In: *AIAA Journal* 115, pp. 1–11. ISSN: 0001-1452. DOI: 10.2514/1.J060659.
- Tsai, Stephen W., Albertino Arteiro, and Jose D. D. Melo (2016). “A trace-based approach to design for manufacturing of composite laminates”. In: *Journal of Reinforced Plastics and Composites* 35.7, pp. 589–600. ISSN: 0731-6844. DOI: 10.1177/0731684415624770.
- Tsai, Stephen W. and José Daniel D. Melo (2015). *Composite materials design and testing: Unlocking mystery with invariants*. Stanford: University. ISBN: 978-0-9860845-0-8.
- Tsai, Stephen W. and Jose Daniel D. Melo (2014). “An invariant-based theory of composites”. In: *Composites Science and Technology* 100, pp. 237–243. ISSN: 02663538. DOI: 10.1016/j.compscitech.2014.06.017.
- Tsai, Stephen W. and Jose Daniel D. Melo (2016). “A unit circle failure criterion for carbon fiber reinforced polymer composites”. In: *Composites Science and Technology* 123, pp. 71–78. ISSN: 02663538. DOI: 10.1016/j.compscitech.2015.12.011.
- Tsai, Stephen W., José Daniel D. Melo, et al. (2017). *Composite laminates: Theory and practice of analysis, design and automated layup*. Stanford: Stanford Aeronautics & Astronautics. ISBN: 9780986084539.
- Tsai, Stephen W. and Edward M. Wu (1971). “A General Theory of Strength for Anisotropic Materials”. In: *Journal of Composite Materials* 5.1, pp. 58–80. ISSN: 0021-9983. DOI: 10.1177/002199837100500106.
- Ueng, Charles E.S. (2002). “Sandwich Composites”. In: *Encyclopedia of physical science and technology*. Ed. by Robert A. Meyers. San Diego: Acad. Press, pp. 407–412. ISBN: 9780122274107. DOI: 10.1016/B0-12-227410-5/00672-4.
- Verein Deutscher Ingenieure (2006). *VDI 2014 Blatt 3, Entwicklung von Bauteilen aus Faser-Kunststoff-Verbund Berechnungen: Development of FRP components (fibre-reinforced plastics) Analysis*.
- Wang, Ben and Hang Gao (2021). “Fibre Reinforced Polymer Composites”. In: *Advances in Machining of Composite Materials*. Ed. by Islam Shyha and Dehong Huo. Cham: Springer International Publishing, pp. 15–43. ISBN: 978-3-030-71438-3.
- Zenkert, Dan, ed. (1997). *The handbook of sandwich construction*. North European engineering and science conference series. Cradley Heath, West Midlands: Engineering Materials Advisory Services Ltd. (EMAS). ISBN: 9780947817961.

A Optimization code

A.1 User manual

A few examples are shown of how to apply the optimization code.

The application as presented here uses Abaqus to obtain the cell loads. Some inputs are Abaqus specific and need to be changed if another finite element software is used. The following examples show the main code that has to be adapted by the user. Changes in Python classes are not necessary, except to implement further failure criteria.

Examples are shown for a simple model that contains one laminate and one load case, and a more advanced model where symmetry is present and two load cases are considered. In addition, a code snippet is shown as an example for running the quad laminate optimization. In principle, only a few lines of code need to be adapted to the specific case.

A.1.1 Setup for a simple model with 1 load case

In this section, a code to run a simple double double optimization is explained. Code is given on the following page and only represents the main code, classes are not shown. By simple, a structure consisting of only one area with any number of cells is meant.

The following steps have to be executed before the optimization can be started:

- set the angle increment (line 5: 7.5)
- set the cell names as defined in Abaqus (line 6: C)
- set the number of cell, same number as modeled in Abaqus (line 7: 100)
- set the failure criterion and the failure mode (line 8&9: TW, LPF)
- define the material parameter for optimization (line 10-29)
- set the material name used in Abaqus (line 30: ACA)

The following lines (33-39) can be used as shown. In these lines some allocations are done, only line 37 may need to be modified if a different failure strain for Nettles circle is required (`ap_Nettles=0.004`).

Line 42 to 45 define the step names, part names, instance names, and composite names as modeled within Abaqus. Note that the instance name is written in capital letters. This is required to enter the odb file correctly. Line 47 is optional and only required if the optimization is started from the windows command line. If the code is started from the Gui, this line can be removed.

Line 42 controls the number of load steps required. In the present case only one load step Step-1 is used for optimization. Multiple load cases can be considered by adding the names of all load cases as modeled in Abaqus, e.g. `['Step-1','Step-2',..., 'Step-n']`.

The optimization procedure is activated and run in line 55 and 56. In line 55 the design tool is set and in line 56 the quad laminate optimization is performed. The parameter `strengthAvg='thick'` means that low loaded areas of the structure are excluded from the convergence criteria.

```

1 if __name__ == '__main__':
2
3     # optimization parameter
4     np.set_printoptions(precision=2)
5     angleIncrement = 7.5
6     cellName = 'C'
7     nCells = 100
8     failureCrit = 'TW'          # 'TW', 'UC', 'Nettles'
9     failureMode = 'FPF'        # 'FPF', 'LPF' for 'TW' and 'UC'
10    matData = { 'name':'C-Ply64',
11                'Trace':160.0,
12                'TraceDeg': 142.0,
13                'E1':140800,
14                'E2':9300,
15                'v21':0.3,
16                'E6':5800,
17                'X':2944.0,
18                'Xs':1983.0,
19                'Y':66.0,
20                'Ys':220.0,
21                'S':93,
22                'F12_s': -0.5,
23
24                'Em_s':0.15,
25                'Em':2500,          # dummy matrix elastic modulus
26                'Gm':1984,          # dummy matrix shear modulus
27                'vf':0.6,           # dummy fiber volume fraction of ply
28                'v21m':0.37,        # dummy Poisson ratio matrix
29            }
30    femMatName = 'ACA'
31
32    # cell names
33    cellNames = [cellName + '-' + str(i + 1) for i in range(nCells)]
34
35    # initialize Lamsearch and build cells
36    LS = Lamsearch()
37    LS.setMaterial(matData, fpf_lpf=failureMode, ap_Nettles=0.004)
38    LS.setAngleField(angleIncrement)
39    LS.createCells(cellName, nCells)
40
41    # Abaqus dependent variables
42    stepNames = ['Step-1']
43    partName = 'upperSkin'
44    instanceName = 'UPPERSKIN-1'
45    compName = 'CompositeLayup'
46
47    mdb=openMdb(pathName="Wing")      # used to run abaqus with noGui command from cmd
48
49    # instance of abaqus conversion
50    aba = AbaqusConversion(cellNames=cellNames, jobName='Job-1', stepNames=stepNames,
51                           partName=partName, instanceName=instanceName,
52                           compName=compName, matName=femMatName)
53
54    # DD Design Tool
55    dd = DDTool(fem=aba, lamsearch=LS, cellNames=cellNames, failureCrit=failureCrit)
56    dd.runLaminateOptimizationNew(strengthAvg='thick')

```

A.1.2 Setup for a symmetric model with 2 load cases

To run an optimization considering two load cases for a symmetric model, the following steps (similar to the example shown above) have to be executed:

- set the angle increment (line 5: 7.5)
- set the cell names as defined in Abaqus (line 6: C)
- set the number of cell, same number as modeled in Abaqus (line 7: 100)
- set the failure criterion and the failure mode (line 8&9: TW, LPF)
- define the material parameter for optimization (line 10-29)
- set the material name used in Abaqus (line 30: ACA)

The following lines (33-39) can be used as shown. In these lines some allocations are done, only line 37 may need to be modified if a different failure strain for Nettles circle is required (ap_Nettles=0.004).

Line 42 to 47 define the step names, part names, instance names, and composite names as modeled within Abaqus. Note that the instance names are written in capital letters. This is required to enter the odb file correctly. Line 49 is optional and only required if the optimization is started from the windows command line. If the code is started from the Gui, this line can be removed.

The optimization procedure is activated and run in line 59 and 61. In line 59 the design tool is set and in line 61 the laminate optimization is performed. The parameter strengthAvg='thick' means that low loaded areas of the structure are excluded from the convergence criteria.

Note that for symmetry, the structure needs to be modeled that the stacking directions, i.e. face normals, of the laminate area and the symmetry area point in the same direction. The code automatically stacks the plies in the right order to obtain a true symmetric design.

```

1 if __name__ == '__main__':
2
3     # optimization parameter
4     np.set_printoptions(precision=2)
5     angleIncrement = 7.5
6     cellName = 'C'
7     nCells = 100
8     failureCrit = 'TW'           # 'TW', 'UC', 'Nettles'
9     failureMode = 'FPF'         # 'FPF', 'LPF' for 'TW' and 'UC'
10    matData = { 'name':'C-Ply64',
11                'Trace':160.0,
12                'TraceDeg': 142.0,
13                'E1':140800,
14                'E2':9300,
15                'v21':0.3,
16                'E6':5800,
17                'X':2944.0,
18                'Xs':1983.0,
19                'Y':66.0,
20                'Ys':220.0,
21                'S':93,
22                'F12_s': -0.5,
23
24                'Em_s':0.15,
25                'Em':2500,         # dummy matrix elastic modulus
26                'Gm':1984,         # dummy matrix shear modulus
27                'vf':0.6,          # dummy fiber volume fraction of ply
28                'v21m':0.37,       # dummy Poisson ratio matrix
29            }
30    femMatName = 'ACA'
31
32    # cell names
33    cellNames = [cellName + '-' + str(i + 1) for i in range(nCells)]
34
35    # initialize Lamsearch and build cells
36    LS = Lamsearch()
37    LS.setMaterial(matData, fpf_lpf=failureMode, ap_Nettles=0.004)
38    LS.setAngleField(angleIncrement)
39    LS.createCells(cellName, nCells)
40
41    # Abaqus dependent variables
42    stepNames = ['Step-1', 'Step-2']
43    partName = 'upperSkin'
44    partSymName = 'lowerSkin'
45    instanceName = 'UPPERSKIN-1'
46    instanceSymName = 'LOWERSKIN-1'
47    compName = 'CompositeLayup'
48
49    mdb=openMdb(pathName="Wing")    # used to run abaqus with noGui command from cmd
50
51    # instance of abaqus conversion
52    aba = AbaqusConversion(cellNames=cellNames, jobName='Job-1', stepNames=stepNames,
53                           partName=partName, instanceName=instanceName,
54                           compName=compName, matName=femMatName,
55                           partSymName=partSymName, instanceSymName=instanceSymName,
56                           symmetry=True)
57
58    # DD Design Tool
59    dd = DDTool(fem=aba, lamsearch=LS, cellNames=cellNames, failureCrit=failureCrit,
60               symCells=True)
61    dd.runLaminateOptimizationNew(strengthAvg='thick')

```

A.1.3 Setup for a quad laminate model

Quad laminate optimizations can be run the same way as for double double laminates. The only difference is that the last is changed to: `dd.runQuadLaminateOptimization()`.

The following steps (similar to the examples shown above) have to be executed before the optimization can be started:

- set the angle increment (line 5: 7.5)
- set the cell names as defined in Abaqus (line 6: C)
- set the number of cell, same number as modeled in Abaqus (line 7: 100)
- set the failure criterion and the failure mode (line 8&9: TW, LPF)
- define the material parameter for optimization (line 10-29)
- set the material name used in Abaqus (line 30: ACA)

The following lines (33-39) can be used as shown. In these lines some allocations are done, only line 37 may need to be modified if a different failure strain for Nettles circle is required (`ap_Nettles=0.004`).

Line 42 to 45 define the step names, part names, instance names, and composite names as modeled within Abaqus. Note that the instance name is written in capital letters. This is required to enter the odb file correctly. Line 47 is optional and only required if the optimization is started from the windows command line. If the code is started from the Gui, this line can be removed.

The optimization procedure is activated and run in line 55 and 56. In line 55 the design tool is set and in line 56 the quad laminate optimization is performed. The parameter `strengthAvg='thick'` means that low loaded areas of the structure are excluded from the convergence criteria.

```

1 if __name__ == '__main__':
2
3     # optimization parameter
4     np.set_printoptions(precision=2)
5     angleIncrement = 7.5
6     cellName = 'C'
7     nCells = 100
8     failureCrit = 'TW'           # 'TW', 'UC', 'Nettles'
9     failureMode = 'FPF'         # 'FPF', 'LPF' for 'TW' and 'UC'
10    matData = { 'name':'C-Ply64',
11                'Trace':160.0,
12                'TraceDeg': 142.0,
13                'E1':140800,
14                'E2':9300,
15                'v21':0.3,
16                'E6':5800,
17                'X':2944.0,
18                'Xs':1983.0,
19                'Y':66.0,
20                'Ys':220.0,
21                'S':93,
22                'F12_s': -0.5,
23
24                'Em_s':0.15,
25                'Em':2500,         # dummy matrix elastic modulus
26                'Gm':1984,         # dummy matrix shear modulus
27                'vf':0.6,          # dummy fiber volume fraction of ply
28                'v21m':0.37,      # dummy Poisson ratio matrix
29            }
30    femMatName = 'ACA'
31
32    # cell names
33    cellNames = [cellName + '-' + str(i + 1) for i in range(nCells)]
34
35    # initialize Lamsearch and build cells
36    LS = Lamsearch()
37    LS.setMaterial(matData, fpf_lpf=failureMode, ap_Nettles=0.004)
38    LS.setAngleField(angleIncrement)
39    LS.createCells(cellName, nCells)
40
41    # Abaqus dependent variables
42    stepNames = ['Step-1']
43    partName = 'upperSkin'
44    instanceName = 'UPPERSKIN-1'
45    compName = 'CompositeLayup'
46
47    mdb=openMdb(pathName="Wing")    # used to run abaqus with noGui command from cmd
48
49    # instance of abaqus conversion
50    aba = AbaqusConversion(cellNames=cellNames, jobName='Job-1', stepNames=stepNames,
51                            partName=partName, instanceName=instanceName,
52                            compName=compName, matName=femMatName)
53
54    # DD Design Tool
55    dd = DDTool(fem=aba, lamsearch=LS, cellNames=cellNames, failureCrit=failureCrit)
56    dd.runQuadLaminateOptimization(strengthAvg='thick')

```

A.1.4 Format of the output file

During the optimization, an output file is created where the optimization parameters are summarized, as well as the cell dependent outputs are given. The file is updated in every iteration and can be viewed while the code is running.

At the top of the output file, the optimization parameters are summarized. Starting by the failure criterion and in addition the respective failure mode (FPF,LPF). In the following, the convergence criteria are given: criterion 1 - change of DD angle between two iterations, criterion 2 - averaged strength minus one, criterion 3 change of averaged strength between two iterations. The maximum number of iterations allowed and the FE material name are given. If symmetry cells are used they are indicated by True, if not, by False. The selected angle increment is given, as well as the strength average method (thick/all) and the laminate optimization method (DD/Quad). Note that for strength avg. equal to thick, cell with a thickness below one ply (e.g. approx. 0.0625 for thin plies and approx. 0.125 for standard plies) are not considered for the averaged strength convergence criterion.

```

Double Double Laminate Optimization

| Optimization Parameter |
|-----|-----|
| Failure Criterion      | Tsai-Wu FPF |
|-----|-----|
| Convergence Criterion 1 | 0.0          |
|-----|-----|
| Convergence Criterion 2 | 0.1          |
|-----|-----|
| Convergence Criterion 3 | 0.001        |
|-----|-----|
| Maximum No. Iterations | 30           |
|-----|-----|
| Material                | ACA          |
|-----|-----|
| Symmetry Cells          | True         |
|-----|-----|
| Angle Incr.             | 4.5          |
|-----|-----|
| strength avg.           | thick        |
|-----|-----|
| laminate                 | DD           |
|-----|-----|

| Cell | Cell Area |
|-----|-----|
| C-1  | 29889.86  |
|-----|-----|
| C-2  | 28400.42  |
|-----|-----|

```

The following two figures show frames of the iteration procedure. Each iteration is indicated, followed by a summary of the laminate angles and averaged strength. Since for iteration 1 no current ply angles are defined, their field is empty, but the resulting ply angles and averaged strength of iteration one are given. In the column "current" the setup before the design update is given and in the column "resulting" the resulting setup.

Similarly, the cell data are given. In the columns below "current configuration", the current cell configuration is given, as well as the corresponding cell loads, obtained by the finite element software. In the columns below "iteration outcome", the resulting strength ratios for the laminate as evaluated in the current iteration are given for all considered load cases, as well the respective thicknesses and the thickness used in the next iteration.


```
*****
iteration 1
*****
```

angle	current	resulting
phi	-	40.5
psi	-	58.5
Ravg		3.3072

current configuration					iteration outcome		
Cell	Thickness	Sig_11	Sig_22	Sig_12	resulting R	Thickness	Thickness i+1
C-1	3.0	4.68	-0.63	2.78	15.1224325682	0.198380782091	
		5.80	-9.29	1.08	7.72575917346	0.388311353311	0.388311353311
		-4.69	0.62	-2.79	36.1241201926	0.0830470052698	
		-5.81	9.28	-1.08	16.5475285949	0.18129595503	
C-2	3.0	9.76	3.20	5.68	9.1582902595	0.327572059303	
		18.70	-7.50	6.41	3.56336812649	0.841900105043	0.841900105043
		-9.77	-3.20	-5.68	23.9282470083	0.125374834143	
		-18.70	7.49	-6.42	8.58092003923	0.349612860426	

```
*****
iteration 2
*****
```

angle	current	resulting
phi	40.5	49.5
psi	58.5	49.5
Ravg		1.8530

current configuration					iteration outcome		
Cell	Thickness	Sig_11	Sig_22	Sig_12	resulting R	Thickness	Thickness i+1
C-1	0.388311207294	12.10	12.84	13.03	8.01399112627	0.0484541598781	0.0484541598781
		4.47	2.13	5.07	12.1037026829	0.0320820179964	
		-12.10	-12.89	-13.07	27.0393476441	0.0143609680383	
		-4.47	-2.18	-5.09	32.0525553412	0.0121148283861	
C-2	0.841899991035	20.41	22.41	19.19	5.21033013424	0.161582849713	0.161582849713
		14.68	13.24	13.04	5.7755098133	0.145770679689	
		-20.43	-22.44	-19.21	18.1090545686	0.0464905546474	
		-14.70	-13.27	-13.06	17.916465936	0.0469902934006	

After finding convergence or if the maximum number of iterations is reached, the procedure stops and the cell thicknesses for the digitized design are given.

```
convergence is found in iteration 7
```

Cell	Thickness	Digitized
C-1	6.73169219085e-07	0.25
C-2	0.000154666905292	0.25
C-3	0.000958420787094	0.25
C-4	0.00278223242122	0.25
C-5	0.00382287166554	0.25

A.2 Python implementation

A short introduction to the classes of the improved DD-Design Tool follows. The detailed documentation of all classes and methods is contained in the Python code as docstring. A total of 5 classes are implemented in the code, each with unique methods and variables. In addition, the classes are sorted by their tasks to give the code a logical structure.

AbaqusConversion

The class AbaqusConversion is the connection to Abaqus/Cae. The class consists of methods to run simulations, read data from the output odb file, process the element outputs and to update the Abaqus model configuration.

Material

The Material class is used to perform all material dependent calculations such as universal engineering constants or degraded material properties. All material dependent parameters are stored within this class.

Cell

The Cell class in combination with the Lamsearch Class is the heart of the Python code. Within the cell class, the strength ratio fields are calculated for all cell loads and thickness scaling is also performed.

Lamsearch

The Lamsearch class is used to organize and control all instances of the Cell class. Cell loads are assigned to the respective cells to calculate the cell dependent strength fields. With the cell-dependent strength fields, the global strength field is calculated by this class and the best double angles are determined.

DDTool

The DDTool class is used to run the optimization procedures, connect all other classes and control the instance of the Lamsearch class. In addition, the optimization output file is also created by this class.

The Python implementation of the improved DD-Design Tool is not included in this version. Please contact Prof. Klemens Rother (klemens.rother@hm.edu) or Timo Stiels (timo.stiels@hotmail.de).

A.3 Python code verification

The DD-Design Tool implemented in Python was verified by optimizing several test cases in both the Ansys version (DiCaprio, Riccio, and Tsai 2020) and the Python implementation. This chapter presents an exemplary verification for a composite plate and two load cases. The results were compared and only negligible small differences were observed.

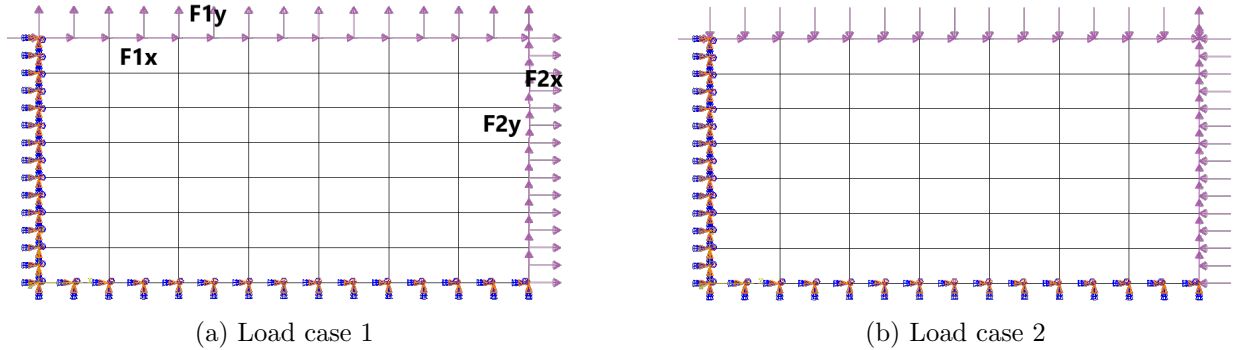


Figure A.1: Test case: rectangular plate with 49 partitions and two load cases.

The tested plate has a length of $l = 700\text{mm}$ and a height of $h = 350\text{mm}$. The cells have a length of $l = 100\text{mm}$ and a height of $h = 50\text{mm}$. Figure A.1 shows both load cases that are applied to the plate and their values are shown in table A.1.

Note that a separate optimization was performed for each load case.

Table A.1: Two load cases for plate optimization.

Load case	F1x	F1y	F2x	F2y
1	150 kN	30 kN	60 kN	75 kN
2	150 kN	-30 kN	-60 kN	75 kN

For all optimization, the start design is chosen as $[0, -45, 90, 45]_s$ and C-Ply 64 as material. For both load cases, the optimization results of both tools are approximately the same. For the thicknesses and strength values, minor differences from the third decimal place onwards can be observed. The digitized thicknesses are the same for both tools.

In the following sub-chapters, the optimization results for both load cases (LC1 and LC2) and all failure criteria (Tsai-Wu, uni circle, Nettles circle) are presented. The convergence criteria of the python code were applied to match the convergence criteria of the original DD-Design Tool.

A.3.1 Load case 1, Tsai-Wu failure criterion

Table A.2: Resulting cell thicknesses for LC 1 and Tsai-Wu failure criterion.

(a) DD-Design Tool

1.246	1.193	1.035	0.895	0.808	0.770	0.779
0.772	0.738	0.654	0.626	0.644	0.694	0.795
0.570	0.472	0.478	0.565	0.642	0.713	0.865
0.417	0.367	0.484	0.612	0.689	0.778	0.942
0.301	0.388	0.595	0.693	0.765	0.873	1.007
0.230	0.546	0.739	0.782	0.864	0.997	1.058
0.237	0.765	0.849	0.891	0.990	1.134	1.120

(b) Python Version

1.245	1.192	1.034	0.894	0.807	0.771	0.779
0.772	0.738	0.654	0.626	0.654	0.693	0.794
0.570	0.472	0.478	0.566	0.642	0.711	0.865
0.417	0.367	0.484	0.613	0.688	0.778	0.942
0.301	0.388	0.595	0.694	0.764	0.872	1.008
0.230	0.546	0.739	0.781	0.863	0.997	1.058
0.237	0.766	0.849	0.890	0.990	1.134	1.120

Table A.3: Resulting cell strengths for LC 1 and Tsai-Wu failure criterion.

(a) DD-Design Tool

1.001	0.959	0.950	0.973	0.997	1.004	1.004
0.974	0.997	1.043	1.061	1.022	1.003	0.991
0.973	1.060	1.093	1.024	0.980	0.967	0.982
1.023	1.126	1.044	0.965	0.948	0.946	0.999
1.097	1.159	0.991	0.954	0.950	0.950	1.029
1.187	1.111	0.989	0.985	0.969	0.971	1.064
1.311	1.032	1.030	1.021	1.012	1.021	1.102

(b) Python Version

1.001	0.959	0.951	0.973	0.998	1.004	1.004
0.974	0.997	1.043	1.062	1.030	1.004	0.991
0.972	1.061	1.093	1.022	0.980	0.968	0.982
1.023	1.126	1.044	0.964	0.949	0.947	0.998
1.097	1.159	0.990	0.954	0.950	0.950	1.029
1.187	1.110	0.989	0.985	0.969	0.971	1.064
1.312	1.031	1.030	1.021	1.012	1.021	1.102

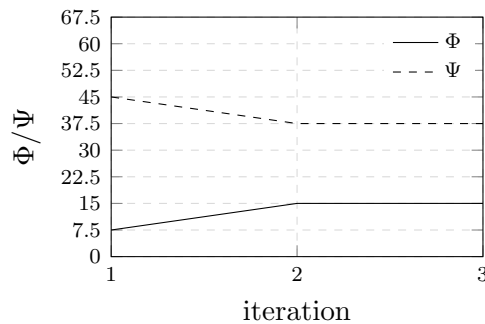
Table A.4: Resulting digitized cell thicknesses for LC 1 and Tsai-Wu failure criterion.

(a) DD-Design Tool

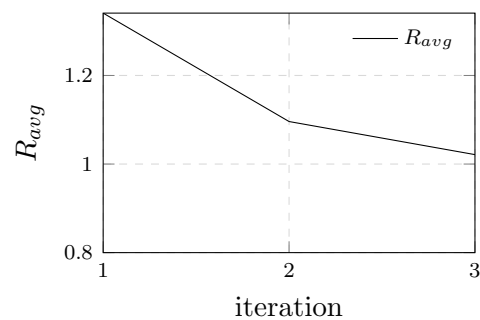
1.250	1.250	1.250	1.000	1.000	1.000	1.000
1.000	0.750	0.750	0.750	0.750	0.750	1.000
0.750	0.500	0.500	0.750	0.750	0.750	1.000
0.500	0.500	0.500	0.750	0.750	1.000	1.000
0.500	0.500	0.750	0.750	1.000	1.000	1.250
0.250	0.750	0.750	1.000	1.000	1.000	1.250
0.250	1.000	1.000	1.000	1.000	1.250	1.250

(b) Python Version

1.250	1.250	1.250	1.000	1.000	1.000	1.000
1.000	0.750	0.750	0.750	0.750	0.750	1.000
0.750	0.500	0.500	0.750	0.750	0.750	1.000
0.500	0.500	0.500	0.750	0.750	1.000	1.000
0.500	0.500	0.750	0.750	1.000	1.000	1.250
0.250	0.750	0.750	1.000	1.000	1.000	1.250
0.250	1.000	1.000	1.000	1.000	1.250	1.250



(a) DD-angles



(b) Averaged strength

Figure A.2: Double Double angles and averaged strength of all iterations for LC 1 and Tsai-Wu failure criterion.

A.3.2 Load case 1, unit circle failure criterion

Table A.5: Resulting cell thicknesses for LC 1 and unit circle failure criterion.

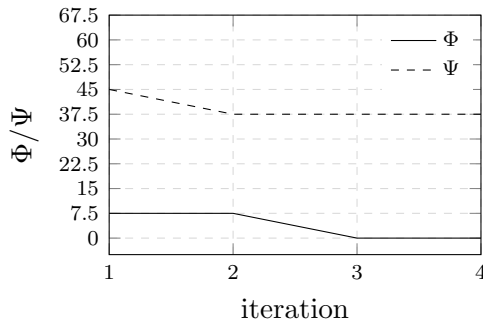
(a) DD-Design Tool							(b) Python Version						
1.744	1.598	1.364	1.135	0.971	0.896	0.920	1.743	1.597	1.363	1.133	0.969	0.897	0.920
0.951	0.856	0.714	0.648	0.661	0.752	0.942	0.951	0.856	0.714	0.648	0.678	0.751	0.942
0.612	0.483	0.451	0.537	0.647	0.783	1.063	0.612	0.483	0.451	0.538	0.647	0.781	1.063
0.399	0.322	0.423	0.577	0.702	0.886	1.197	0.399	0.322	0.424	0.578	0.701	0.884	1.197
0.263	0.304	0.524	0.666	0.797	1.026	1.322	0.263	0.304	0.525	0.666	0.797	1.025	1.322
0.178	0.416	0.657	0.766	0.925	1.194	1.432	0.178	0.416	0.657	0.766	0.924	1.194	1.432
0.163	0.609	0.764	0.874	1.074	1.377	1.546	0.162	0.609	0.764	0.874	1.073	1.377	1.546

Table A.6: Resulting cell strengths for LC 1 and unit circle failure criterion.

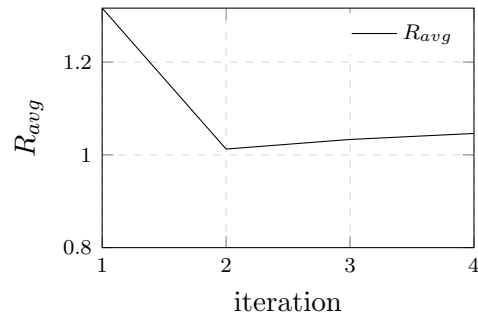
(a) DD-Design Tool							(b) Python Version						
0.900	0.900	0.906	0.936	0.983	1.013	1.010	0.901	0.900	0.906	0.936	0.983	1.013	1.010
0.962	0.987	1.038	1.088	1.083	1.048	0.998	0.962	0.986	1.038	1.088	1.081	1.048	0.998
1.030	1.082	1.150	1.118	1.068	1.020	0.972	1.030	1.082	1.150	1.118	1.067	1.021	0.972
1.110	1.197	1.166	1.080	1.038	0.988	0.957	1.110	1.197	1.166	1.079	1.038	0.988	0.957
1.191	1.263	1.106	1.046	1.011	0.964	0.948	1.191	1.263	1.105	1.045	1.012	0.965	0.948
1.302	1.202	1.066	1.028	0.990	0.951	0.941	1.302	1.201	1.065	1.028	0.990	0.951	0.941
1.373	1.119	1.053	1.020	0.977	0.946	0.935	1.373	1.118	1.053	1.020	0.977	0.946	0.935

Table A.7: Resulting digitized cell thicknesses for LC 1 and unit circle failure criterion.

(a) DD-Design Tool							(b) Python Version						
1.750	1.750	1.500	1.250	1.000	1.000	1.000	1.750	1.750	1.500	1.250	1.000	1.000	1.000
1.000	1.000	0.750	0.750	0.750	1.000	1.000	1.000	1.000	0.750	0.750	0.750	1.000	1.000
0.750	0.500	0.500	0.750	0.750	1.000	1.250	0.750	0.500	0.500	0.750	0.750	1.000	1.250
0.500	0.500	0.500	0.750	0.750	1.000	1.250	0.500	0.500	0.500	0.750	0.750	1.000	1.250
0.500	0.500	0.750	0.750	1.000	1.250	1.500	0.500	0.500	0.750	0.750	1.000	1.250	1.500
0.250	0.500	0.750	1.000	1.000	1.250	1.500	0.250	0.500	0.750	1.000	1.000	1.250	1.500
0.250	0.750	1.000	1.000	1.250	1.500	1.750	0.250	0.750	1.000	1.000	1.250	1.500	1.750



(a) DD-angles



(b) Averaged strength

Figure A.3: Double Double angles and averaged strength of all iterations for LC 1 and unit circle failure criterion.

A.3.3 Load case 1, Nettles circle failure criterion

Table A.8: Resulting cell thicknesses for LC 1 and Nettles circle failure criterion.

(a) DD-Design Tool							(b) Python Version						
3.176	2.979	2.543	2.080	1.669	1.379	1.346	3.171	2.975	2.538	2.074	1.658	1.382	1.347
1.498	1.382	1.092	0.897	0.822	0.971	1.283	1.498	1.384	1.094	0.899	0.879	0.970	1.282
0.863	0.668	0.562	0.623	0.771	0.986	1.431	0.864	0.669	0.564	0.628	0.771	0.983	1.430
0.512	0.373	0.445	0.630	0.823	1.121	1.591	0.513	0.374	0.446	0.633	0.822	1.119	1.592
0.311	0.297	0.519	0.721	0.941	1.314	1.719	0.311	0.297	0.520	0.723	0.940	1.312	1.720
0.183	0.376	0.654	0.837	1.103	1.539	1.818	0.183	0.377	0.655	0.838	1.102	1.538	1.818
0.145	0.550	0.781	0.968	1.295	1.770	1.938	0.144	0.551	0.782	0.968	1.293	1.769	1.938

Table A.9: Resulting cell strengths for LC 1 and Nettles circle failure criterion.

(a) DD-Design Tool							(b) Python Version						
0.945	0.931	0.923	0.928	0.953	0.999	1.020	0.945	0.931	0.924	0.928	0.954	0.999	1.020
0.963	0.983	1.027	1.083	1.095	1.070	1.012	0.962	0.982	1.027	1.082	1.092	1.070	1.012
1.021	1.070	1.135	1.121	1.077	1.033	0.978	1.020	1.068	1.133	1.118	1.076	1.034	0.978
1.097	1.173	1.152	1.078	1.042	0.995	0.967	1.096	1.172	1.151	1.075	1.043	0.996	0.967
1.177	1.215	1.094	1.042	1.014	0.970	0.971	1.176	1.215	1.093	1.041	1.015	0.971	0.971
1.265	1.162	1.058	1.024	0.991	0.958	0.982	1.265	1.161	1.056	1.024	0.992	0.959	0.982
1.291	1.109	1.042	1.013	0.975	0.957	0.996	1.291	1.107	1.041	1.013	0.976	0.957	0.996

Table A.10: Resulting digitized cell thicknesses for LC 1 and Nettles circle failure criterion.

(a) DD-Design Tool							(b) Python Version						
3.250	3.000	2.750	2.250	1.750	1.500	1.500	3.250	3.000	2.750	2.250	1.750	1.500	1.500
1.500	1.500	1.250	1.000	1.000	1.000	1.500	1.500	1.500	1.250	1.000	1.000	1.000	1.500
1.000	0.750	0.750	0.750	1.000	1.000	1.500	1.000	0.750	0.750	0.750	1.000	1.000	1.500
0.750	0.500	0.500	0.750	1.000	1.250	1.750	0.750	0.500	0.500	0.750	1.000	1.250	1.750
0.500	0.500	0.750	0.750	1.000	1.500	1.750	0.500	0.500	0.750	0.750	1.000	1.500	1.750
0.250	0.500	0.750	1.000	1.250	1.750	2.000	0.250	0.500	0.750	1.000	1.250	1.750	2.000
0.250	0.750	1.000	1.000	1.500	2.000	2.000	0.250	0.750	1.000	1.000	1.500	2.000	2.000

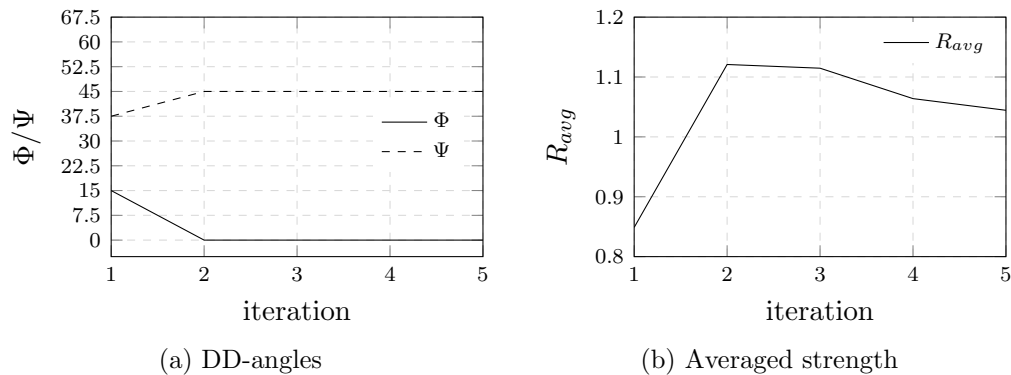


Figure A.4: Double Double angles and averaged strength of all iterations for LC 1 and Nettles circle failure criterion.

A.3.4 Load case 2, Tsai-Wu failure criterion

Table A.11: Resulting cell thicknesses for LC 2 and Tsai-Wu failure criterion.

(a) DD-Design Tool							(b) Python Version						
1.863	1.458	1.117	0.908	0.737	0.612	0.645	1.861	1.457	1.116	0.908	0.736	0.612	0.645
0.545	0.554	0.452	0.363	0.356	0.422	0.625	0.545	0.554	0.452	0.362	0.369	0.421	0.624
0.098	0.113	0.113	0.123	0.208	0.346	0.708	0.099	0.114	0.113	0.124	0.208	0.347	0.708
0.019	0.022	0.025	0.040	0.101	0.261	0.813	0.020	0.022	0.025	0.040	0.101	0.261	0.813
0.004	0.004	0.007	0.016	0.044	0.180	0.963	0.004	0.004	0.007	0.016	0.044	0.179	0.963
0.001	0.001	0.004	0.009	0.026	0.146	1.200	0.001	0.001	0.004	0.009	0.026	0.146	1.200
0.000	0.002	0.004	0.008	0.027	0.126	1.496	0.000	0.002	0.004	0.008	0.027	0.126	1.494

Table A.12: Resulting cell strengths for LC 2 and Tsai-Wu failure criterion.

(a) DD-Design Tool							(b) Python Version						
0.989	0.991	0.993	0.992	0.995	1.001	1.004	0.989	0.991	0.993	0.992	0.994	1.001	1.004
1.001	0.996	0.997	1.008	1.010	1.009	1.002	1.001	0.995	0.996	1.008	1.010	1.009	1.002
1.106	1.079	1.067	1.059	1.025	1.010	0.996	1.106	1.079	1.066	1.059	1.025	1.010	0.996
1.214	1.179	1.158	1.111	1.051	1.019	0.994	1.214	1.178	1.157	1.111	1.051	1.019	0.994
1.346	1.300	1.231	1.132	1.084	1.031	0.993	1.345	1.299	1.230	1.131	1.084	1.031	0.993
1.464	1.371	1.216	1.130	1.085	1.026	0.992	1.462	1.368	1.214	1.129	1.085	1.026	0.992
1.477	1.325	1.179	1.114	1.073	1.021	0.991	1.475	1.322	1.177	1.113	1.073	1.021	0.991

Table A.13: Resulting digitized cell thicknesses for LC 2 and Tsai-Wu failure criterion.

(a) DD-Design Tool							(b) Python Version						
2.000	1.500	1.250	1.000	0.750	0.750	0.750	2.000	1.500	1.250	1.000	0.750	0.750	0.750
0.750	0.750	0.500	0.500	0.500	0.500	0.750	0.750	0.750	0.500	0.500	0.500	0.500	0.750
0.250	0.250	0.250	0.250	0.250	0.500	0.750	0.250	0.250	0.250	0.250	0.250	0.500	0.750
0.250	0.250	0.250	0.250	0.250	0.500	1.000	0.250	0.250	0.250	0.250	0.250	0.500	1.000
0.250	0.250	0.250	0.250	0.250	0.250	1.000	0.250	0.250	0.250	0.250	0.250	0.250	1.000
0.250	0.250	0.250	0.250	0.250	0.250	1.250	0.250	0.250	0.250	0.250	0.250	0.250	1.250
0.250	0.250	0.250	0.250	0.250	0.250	1.500	0.250	0.250	0.250	0.250	0.250	0.250	1.500

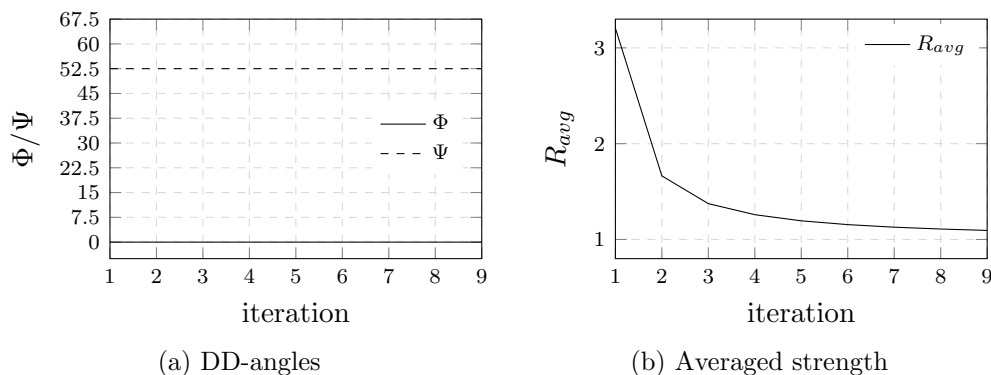


Figure A.5: Double Double angles and averaged strength of all iterations for LC 2 and Tsai-Wu failure criterion.

A.3.5 Load case 2, unit circle failure criterion

Table A.14: Resulting cell thicknesses for LC 2 and unit circle failure criterion.

(a) DD-Design Tool							(b) Python Version						
2.129	1.565	1.158	0.941	0.766	0.640	0.677	2.127	1.563	1.157	0.941	0.766	0.640	0.677
0.718	0.690	0.512	0.385	0.383	0.448	0.653	0.719	0.691	0.513	0.385	0.393	0.447	0.652
0.108	0.130	0.115	0.117	0.217	0.367	0.751	0.108	0.130	0.115	0.117	0.217	0.368	0.751
0.014	0.018	0.018	0.032	0.097	0.270	0.883	0.014	0.018	0.019	0.032	0.097	0.270	0.883
0.002	0.002	0.003	0.011	0.037	0.182	1.019	0.002	0.002	0.003	0.011	0.037	0.181	1.019
0.000	0.000	0.002	0.006	0.023	0.144	1.230	0.000	0.000	0.002	0.006	0.023	0.143	1.229
0.000	0.001	0.002	0.006	0.026	0.124	1.515	0.000	0.001	0.002	0.006	0.026	0.124	1.513

Table A.15: Resulting cell strengths for LC 2 and unit circle failure criterion.

(a) DD-Design Tool							(b) Python Version						
0.995	0.997	0.998	0.996	0.996	1.001	1.002	0.995	0.997	0.998	0.996	0.996	1.001	1.002
0.991	0.988	0.988	1.000	1.004	1.005	1.001	0.991	0.987	0.988	1.000	1.004	1.005	1.001
1.062	1.041	1.037	1.043	1.015	1.005	0.998	1.062	1.041	1.037	1.043	1.015	1.005	0.998
1.180	1.146	1.137	1.095	1.037	1.013	0.996	1.179	1.146	1.136	1.095	1.037	1.013	0.996
1.352	1.303	1.229	1.119	1.069	1.024	0.996	1.351	1.303	1.228	1.118	1.070	1.024	0.996
1.537	1.421	1.228	1.129	1.072	1.022	0.995	1.536	1.420	1.227	1.129	1.072	1.022	0.995
1.556	1.380	1.197	1.116	1.058	1.019	0.994	1.554	1.378	1.196	1.116	1.058	1.019	0.994

Table A.16: Resulting digitized cell thicknesses for LC 2 and unit circle failure criterion.

(a) DD-Design Tool							(b) Python Version						
2.250	1.750	1.250	1.000	1.000	0.750	0.750	2.250	1.750	1.250	1.000	1.000	0.750	0.750
0.750	0.750	0.750	0.500	0.500	0.500	0.750	0.750	0.750	0.750	0.500	0.500	0.500	0.750
0.250	0.250	0.250	0.250	0.250	0.500	1.000	0.250	0.250	0.250	0.250	0.250	0.500	1.000
0.250	0.250	0.250	0.250	0.250	0.500	1.000	0.250	0.250	0.250	0.250	0.250	0.500	1.000
0.250	0.250	0.250	0.250	0.250	0.250	1.250	0.250	0.250	0.250	0.250	0.250	0.250	1.250
0.250	0.250	0.250	0.250	0.250	0.250	1.250	0.250	0.250	0.250	0.250	0.250	0.250	1.250
0.250	0.250	0.250	0.250	0.250	0.250	1.750	0.250	0.250	0.250	0.250	0.250	0.250	1.750

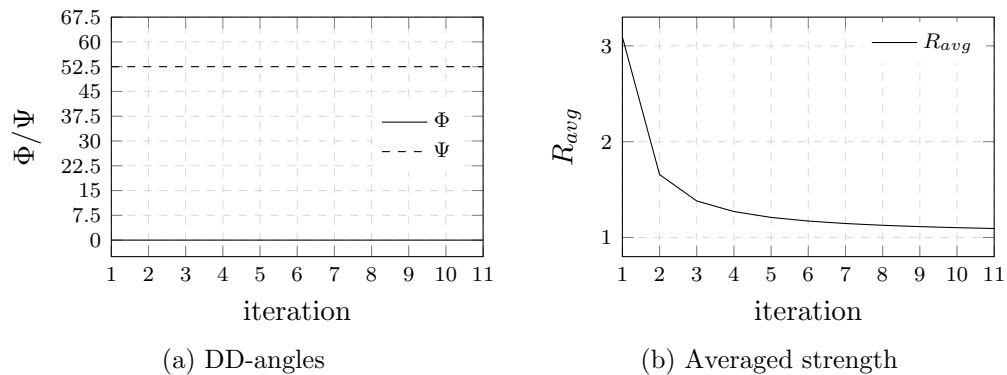


Figure A.6: Double Double angles and averaged strength of all iterations for LC 2 and unit circle failure criterion.

A.3.6 Load case 2, Nettles circle failure criterion

Table A.17: Resulting cell thicknesses for LC 2 and Nettles circle failure criterion.

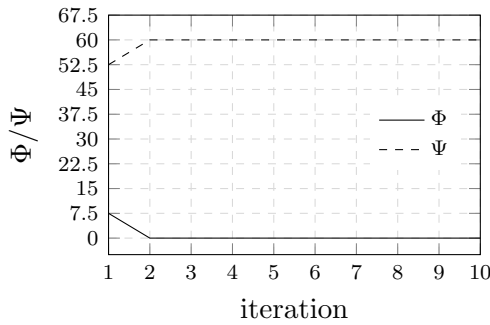
(a) DD-Design Tool							(b) Python Version						
3.234	2.490	2.006	1.712	1.471	1.412	1.657	3.231	2.489	2.006	1.712	1.472	1.411	1.657
0.967	0.899	0.726	0.762	0.942	1.076	1.477	0.968	0.900	0.727	0.763	0.920	1.077	1.477
0.138	0.160	0.163	0.318	0.633	0.924	1.457	0.138	0.160	0.163	0.318	0.634	0.923	1.457
0.019	0.025	0.034	0.120	0.343	0.699	1.507	0.019	0.024	0.034	0.119	0.345	0.699	1.506
0.003	0.003	0.011	0.045	0.140	0.387	1.518	0.003	0.003	0.011	0.045	0.140	0.387	1.517
0.000	0.001	0.008	0.024	0.059	0.179	1.502	0.000	0.001	0.008	0.024	0.059	0.179	1.502
0.000	0.001	0.007	0.021	0.043	0.118	1.639	0.000	0.001	0.007	0.021	0.042	0.118	1.638

Table A.18: Resulting cell strengths for LC 2 and Nettles circle failure criterion.

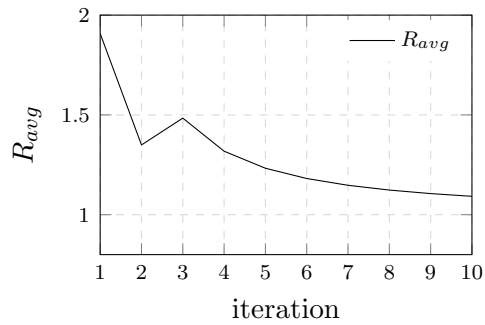
(a) DD-Design Tool							(b) Python Version						
0.994	0.997	0.996	0.995	0.999	1.003	1.002	0.994	0.997	0.996	0.995	0.999	1.003	1.002
0.992	0.990	0.998	1.004	1.003	1.006	1.003	0.992	0.990	0.998	1.004	1.003	1.005	1.003
1.082	1.065	1.068	1.030	1.003	1.002	1.001	1.082	1.065	1.068	1.030	1.003	1.002	1.001
1.202	1.175	1.153	1.057	1.018	1.004	0.998	1.203	1.176	1.154	1.057	1.017	1.004	0.998
1.367	1.316	1.173	1.085	1.047	1.022	0.997	1.368	1.317	1.173	1.086	1.047	1.022	0.997
1.596	1.376	1.157	1.098	1.067	1.040	0.997	1.598	1.377	1.158	1.099	1.067	1.040	0.997
1.670	1.337	1.147	1.095	1.063	1.035	0.994	1.675	1.339	1.148	1.095	1.064	1.035	0.994

Table A.19: Resulting digitized cell thicknesses for LC 2 and Nettles circle failure criterion.

(a) DD-Design Tool							(b) Python Version						
3.250	2.500	2.250	1.750	1.500	1.500	1.750	3.250	2.500	2.250	1.750	1.500	1.500	1.750
1.000	1.000	0.750	1.000	1.000	1.250	1.500	1.000	1.000	0.750	1.000	1.000	1.250	1.500
0.250	0.250	0.250	0.500	0.750	1.000	1.500	0.250	0.250	0.250	0.500	0.750	1.000	1.500
0.250	0.250	0.250	0.250	0.500	0.750	1.750	0.250	0.250	0.250	0.250	0.500	0.750	1.750
0.250	0.250	0.250	0.250	0.250	0.500	1.750	0.250	0.250	0.250	0.250	0.250	0.500	1.750
0.250	0.250	0.250	0.250	0.250	0.250	1.750	0.250	0.250	0.250	0.250	0.250	0.250	1.750
0.250	0.250	0.250	0.250	0.250	0.250	1.750	0.250	0.250	0.250	0.250	0.250	0.250	1.750



(a) DD-angles



(b) Averaged strength

Figure A.7: Double Double angles and averaged strength of all iterations for LC 2 and Nettles circle failure criterion.